2009-07-23

Extreme Ultraviolet Polarimetry with Laser-Generated High-Order Harmonics: Characterization of Uranium

Nicole Brimhall
Brigham Young University - Provo

EXTREME ULTRAVIOLET POLARIMETRY WITH LASER-GENERATED HIGH-ORDER HARMONICS: CHARACTERIZATION OF URANIUM

by

Nicole Brimhall

A dissertation submitted to the faculty of

Brigham Young University

in partial fulfillment of the requirements for the degree of

Doctor of Philosophy

Department of Physics and Astronomy

Brigham Young University

August 2009

BRIGHAM YOUNG UNIVERSITY

GRADUATE COMMITTEE APPROVAL

of a dissertation submitted by

Nicole Brimhall

This dissertation has been read by each member of the following graduate committee and by majority vote has been found to be satisfactory.

Date	Justin B. Peatross, Chair
Date	R. Steven Turley
Date	David D. Allred
Date	Michael Ware
Date	Manuel Berrondo

BRIGHAM YOUNG UNIVERSITY

As chair of the candidate's graduate committee, I have read the dissertation of Nicole Brimhall in its final form and have found that (1) its format, citations, and bibliographical style are consistent and acceptable and fulfill university and department style requirements; (2) its illustrative materials including figures, tables, and charts are in place; and (3) the final manuscript is satisfactory to the graduate committee and is ready for submission to the university library.

Date

Justin B. Peatross
Chair, Graduate Committee

Accepted for the Department

Ross L. Spencer, Department Chair
Department of Physics and Astronomy

Accepted for the College

Thomas W. Sederberg, Associate Dean
College of Physical and Mathematical Sciences

ABSTRACT

EXTREME ULTRAVIOLET POLARIMETRY WITH LASER-GENERATED HIGH-ORDER HARMONICS: CHARACTERIZATION OF URANIUM

Nicole Brimhall

Department of Physics and Astronomy

Doctor of Philosophy

We developed an extreme ultraviolet (EUV) polarimeter, which employs laser-generated high-order harmonics as the light source. This relatively high-flux, directional EUV source has available wavelengths between 10 nm and 47 nm with easily rotatable linear polarization. The polarimeter has allowed us to characterize the optical constants of materials that may be useful for EUV optics. The instrument has a versatile positioning system and a spectral resolution of about 180, and we have demonstrated that reflectance as low as 0.1% can be measured repeatably at EUV wavelengths.

We investigate the high harmonic source used for polarimetry measurements by documenting the spatial evolution of the generating laser in a semi-infinite helium-filled gas cell under conditions suitable for harmonic generation. The laser is observed to focus, diverge, and refocus, accompanied by a flattop beam profile and extended harmonic phase matching. We numerically simu-

late the propagation to investigate these experimental results. We find that harmonic energy comes from the forward portion of the laser pulse, whereas the latter portion gives rise to the incidental double laser focusing. Good phase matching for the harmonics arises in large measure from a balance between the linear phase delay of the neutral atoms and the Gouy shift, which is elongated and nearly linearized when an aperture is partially closed on the beam.

We compare reflectance data taken with the polarimeter instrument with expected results from well-characterized samples and find that they agree. To improve repeatability and reduce the effects of systematic measurement errors we have measured the ratio of p- to s-polarized reflectance and shown that optical constants can be extracted from this data as efficiently as from absolute reflectance measurements. These ratio measurements allow more accurate recovery of optical constants than our absolute reflectance measurements for our well-characterized samples.

We use the polarimeter instrument and the ratio reflectance technique to determine the optical constants of copper, uranium, and their natural oxides from 10-47 nm. For copper, this measurement resolves previously conflicting data sets, where disagreement on optical-constant values arises from failure to keep samples from oxidizing before measurement. Uranium has been proposed as a high-reflectance material in the EUV for several years, however difficulties with oxidation have prevented its careful characterization previous to this work. We find that measured optical constants for uranium do not agree well with previously accepted theoretical calculations.

ACKNOWLEDGMENTS

I would like to acknowledge my advisor, Justin Peatross for all of his support and assistance. Also Steve Turley, David Allred, and Michael Ware for invaluable advice and discussions. Thank you to fellow graduate student John Painter and to 'my' undergraduates: Nathan Powers, Gavin Giraud, Mark Adams, Matt Turner, Nick Herrick, Nathan Heilmann, Eric Cunningham, Jacob Johansen, Jordan Maucotel, Mike Adams, and Jordan Cox. I would also like to thank the National Science Foundation for supporting this research (Grant# PHY-0457316). And last, but not least, thank you to my family and my wonderful husband Bryan for encouraging words, patient listening, and hugs, without which I never would have made it this far.

PUBLICATIONS

1. N. Brimhall, J. C. Painter, M. Turner, S. V. Voronov, R. S. Turley, M. Ware, and J. Peatross, "Construction of an extreme ultraviolet polarimeter based on high-order harmonic generation," Proc. of SPIE **6317**, 63170Y (2006).

2. J. C. Painter, M. Adams, N. Brimhall, E. Christensen, G. Giraud, N. Powers, M. Turner, M. Ware, and J. Peatross, "Direct observation of laser filamentation in high-order harmonic generation," Opt. Lett. **31**, 3471-3473 (2006).

3. N. Brimhall, J. C. Painter, N. Powers, G. Giraud, M. Turner, M. Ware, and J. Peatross, "Measured laser-beam evolution during high-order harmonic generation in a semi-infinite gas cell," Opt. Express **15**, 1684-1689 (2007).

4. M. Turner, N. Brimhall, M. Ware, and J. Peatross, "Simulated laser-pulse evolution for high-order harmonic generation in a semi-infinite gas cell," Opt. Express **16**, 1571-1576 (2008).

5. N. Brimhall, M. Turner, N. Herrick, D. D. Allred, R. S. Turley, M. Ware, and J. Peatross, "Extreme-ultraviolet polarimeter utilizing laser-generated high-order harmonics," Rev. Sci. Instr. **79**, 103108-1-7 (2008).

6. N. Brimhall, N. Heilmann, M. Ware, and J. Peatross, "Polarization-ratio reflectance measurements in the extreme ultraviolet," Opt. Lett. **34**, 1429-1431 (2009).

7. N. Brimhall, N. Herrick, D. D. Allred, R. S. Turley, and J. Peatross, "Optical constants for thin films of copper, uranium, and their natural oxides from 10 nm to 47 nm," Appl. Opt. *in preparation.*

Contents

List of Figures

Chapter 1

Introduction

1.1 High Harmonic Generation

Harmonic generation is the process by which a laser interacts with atoms, producing coherent light with frequencies which are integer multiples of the generating laser frequency. This phenomenon was discovered soon after the invention of the laser when Franken and coworkers observed second harmonic generation in quartz [1]. Light passing through a medium such as quartz causes the electrons in the lattice to move in response to the electric field of the light. When the light is sufficiently intense, the motion of the electrons is no longer purely sinusoidal, causing radiation not only at the driving laser frequency but also at higher harmonics of the driving laser field.

In 1987, McPherson et al. produced the first harmonics higher than the fifth, generating orders up to the 17th in neon gas, establishing the field of high harmonic generation (HHG) [2]. High harmonics form a comb of frequencies throughout the extreme ultraviolet (EUV), the wavelength range between 1 and 100 nm. The wavelength of an individual harmonic is λ/q, where λ is the wavelength of the generating laser and q is the harmonic order, an odd integer. (Since a gas is centro-symmetric

any induced polarization of the gas must be an odd function of the electric field. Thus only odd orders are produced.) When an intense generating laser is focused in a gas, many harmonic frequencies (with wavelengths distributed throughout the EUV) simultaneously emerge from the focus in a collimated beam embedded in the residual laser beam, as shown in Figure 1.1.

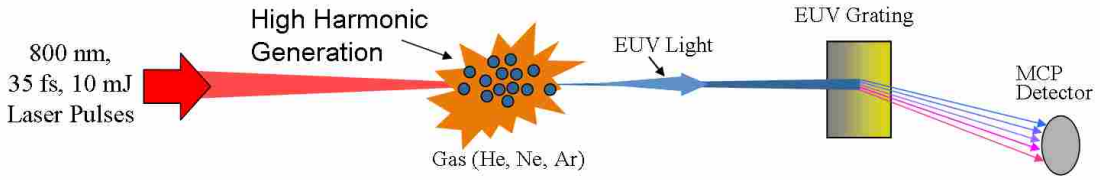

Figure 1.1 Setup for producing high-order harmonics.

High harmonic spectra initially decrease in intensity at low orders but then form a 'plateau,' where the intensity of the harmonics remain approximately constant over many orders [2,3]. This wide plateau of harmonic orders are simultaneously generated up to a maximum order associated with a cutoff frequency [4], which depends on the laser intensity and the atoms used for the harmonic generation. At laser intensities of 10^{13} to 10^{16} W/cm^2, the laser field becomes strong enough to ionize a piece of the electron wavepacket even from noble gases and accelerate it in the field. As the oscillating laser field reverses direction, the electron wavepacket returns, collides, and interferes with the remaining packet, releasing energetic harmonic photons (see Figure 1.2).

To date, harmonics have been generated and detected up to several hundred orders [4–6]. Because the generation process literally rips the generating medium apart, high harmonic generation is implemented most frequently in gases. The ionization potential of the atoms used effectively sets the intensity of the laser field that accelerates the electron. This is because laser pulses inevitably have gradual rise times; an

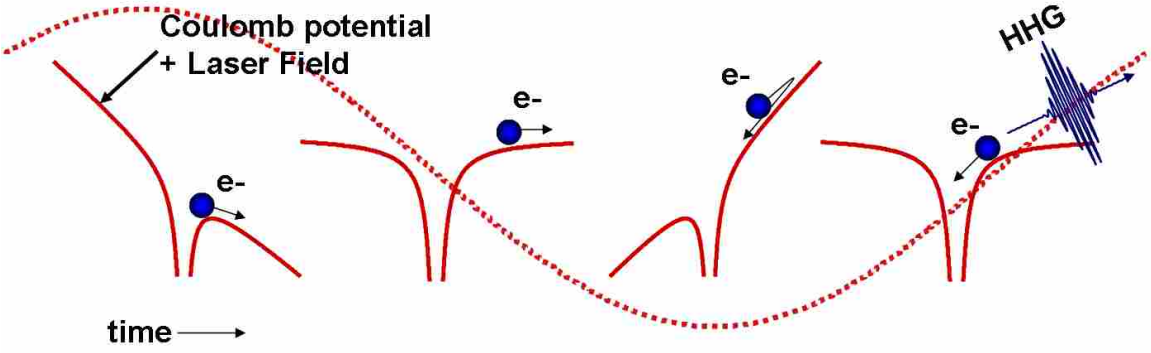

Figure 1.2 Very strong oscillating laser potentials suppress the Coulomb potential enough to ionize even tightly bound electrons. When the field reverses, electrons return and collide with their parent ions, emitting energetic photons in the form of high harmonics.

atom cannot be exposed to higher intensity than that which causes it to ionize. Noble gases are commonly used for high harmonic generation because they have the highest ionization thresholds, and thus can produce the highest harmonics. Helium, with an ionization potential of 24.6 eV, can generate harmonics at the highest intensity of any material. The ionization limit can be increased somewhat by making the laser pulses shorter. Femtosecond lasers are commonly used as driving pulses for HHG because the fast rise time allows the laser to reach higher intensities before ionization occurs [7, 8]. This also allows the maximum number of atoms to participate in the generation process (an ionized atom does not generate harmonics), producing the highest possible orders.

Although light noble gases such as helium produce the highest harmonic orders, these harmonics are not as bright as lower orders produced with heavier gases such as argon. This is because the lighter gases have more tightly bound electron wave packets, which then undergo a faster spreading during the excursion away from and back to the parent ion. This reduces the cross-section of recombination, and thus the brightness of the harmonics [9].

In our laboratory at BYU, high harmonics are generated with 800 nm, 35 fs, ∼10 mJ laser pulses at 10 Hz focused in a gas cell of helium, neon, or argon gas. High harmonics are detected using a grazing-incidence tungsten-coated grating, which disperses and focuses the different harmonic orders in one dimension onto a microchannel plate (MCP) coupled to a phosphor screen. This setup was used to produce the high harmonics seen in Figure 1.3. Each harmonic order strikes the detector at a different horizontal position while the angular size of each harmonic beam is preserved in the vertical dimension.

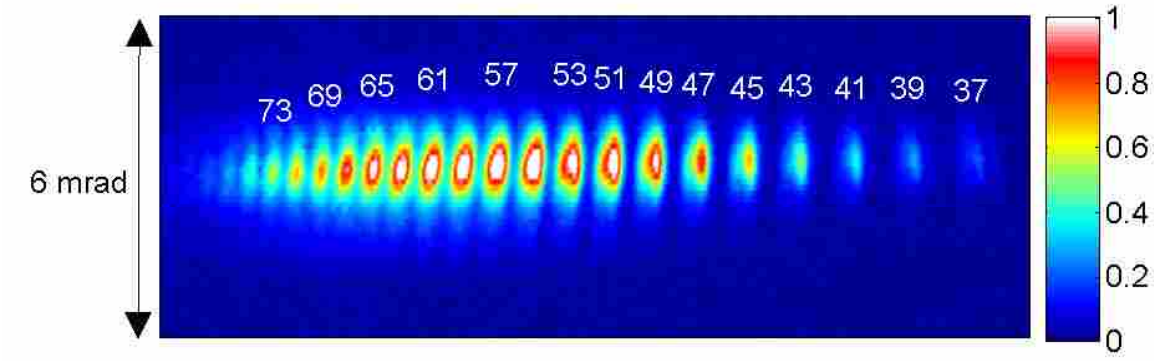

Figure 1.3 Harmonics of order 37-79 (wavelengths 10.1-21.6 nm) produced in neon gas.

Under the correct generation conditions, the EUV beams that emerge from the process are spatially coherent [10, 11]. Also, because electron ionization and recombination occurs near the peak of a laser cycle, the harmonics also have very short pulse duration, even shorter than the driving laser pulse. Each time an ionized electron returns to its atom, it releases a burst of EUV light a fraction of a femtosecond long [12]. Thus, the high harmonic light emerges as an attosecond pulse train which typically lasts less than 10 fs. If the driving laser pulse has a pulse duration of less than 5 fs, a single attosecond pulse may be generated [13].

Harmonics naturally maintain the same linear polarization as the driving laser [14].

In fact, the generating laser must be nearly linearly polarized in order to produce high harmonics. This can be understood by the classical model of high harmonic generation. The model shows that ellipticity in the polarization of the generating laser beam causes the returning electron to miss the parent ion (see Figure 1.4). Quantum mechanically, the overlap of the returning electron wavepacket with the parent ion is reduced when the laser is not linearly polarized. This has been observed experimentally, where the intensity of harmonics decreases rapidly with increasing ellipticity of the generating laser [15].

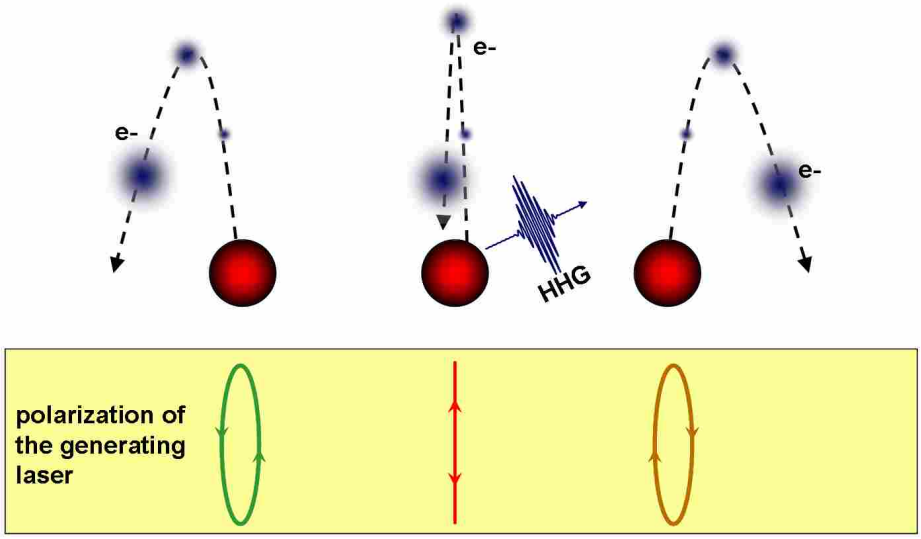

Figure 1.4 Harmonic generation is very sensitive to the polarization of the incident laser. If the laser's polarization is not nearly linear, returning electrons tend to miss their parent ion rather than re-colliding, and no harmonics are produced.

Depending on specific initial conditions, the electron that escapes from the atom may or may not return to re-collide with the parent ion. The maximum kinetic energy an electron can attain from the driving field (on a classical trajectory) and still return to collide with the nucleus is given by $E_{max} = 3.2U_p$, where U_p is the average kinetic energy of a free electron oscillating in the laser field, also called the ponderomotive

potential [16, 17]. We can add the binding potential V_0 to E_{max} to calculate the cutoff frequency emitted from a particular atomic species using $V_0 + E_{max} = \hbar\omega$. The ponderomotive potential is given by

$$U_p = \frac{e^2\mu_0}{8\pi^2 mc} I_0 \lambda^2 \tag{1.1}$$

where e is the electron charge, ϵ_0 is the vacuum permittivity, I_0 is the intensity, λ is the laser wavelength, m is the electron mass, and c is the speed of light. The average kinetic energy of an electron oscillating in response to light with intensity I_0 is designated U_p. Helium, with an ionization potential of 24.6 eV and a corresponding ionization intensity of 1.5×10^{15} W/cm^2, has $E_{max} + V_0 = 311$ eV. This corresponds to a maximum harmonic order of 199 for 800 nm light. In contrast, argon has an ionization potential of 15.8 eV and an ionization intensity of 2.5×10^{14} W/cm^2. Thus the maximum harmonic order that can be produced in argon is only 41. As mentioned, the harmonics generated from argon will tend to be much brighter since the initially larger electron wave packet spreads less during its excursion.

The brightness of harmonic emission depends on many parameters, but is ultimately limited by reabsorption. The generating gas has a non-zero absorption coefficient for EUV wavelengths. Thus, there is a point at which atoms downstream essentially will re-absorb all the harmonics generated by atoms sufficiently far upstream [18].

High harmonics have been generated in gas jets [4], gas cells [6, 19], and hollow gas-filled fibers [20, 21]. L'Huillier et al. reported conversion efficiencies of 10^{-6} for the 17th harmonic order in a xenon gas jet [4]. Rundquist et al. observed conversion efficiencies of 10^{-6} for harmonic orders 23—31 generated in an argon-filled hollow capillary tube [21]. Takahashi et al. demonstrated a conversion efficiency of 10^{-5} for the 27th harmonic generated in an argon-filled gas cell [6]. For higher orders,

Tamaki et al. reported a conversion efficiency of 10^{-6} for the 49th order generated in a neon-filled gas cell [19].

1.2 Phase Matching

In order to generate the largest possible output signal, the harmonic contributions of individual atoms need to constructively interfere. Hence, the harmonics generated upstream in the medium need to be in phase with harmonics generated downstream, a principle known as phase matching. In short, the generating laser light and each harmonic must have the same phase velocity as they propagate together through the generating medium so the harmonics stay in phase with the generating pulse. There are several sources of phase mismatch, including geometrical phase mismatch due to wavelength-dependent diffraction, frequency-dependent index variations, and intensity-dependent variations in the phases of the harmonics as they are emitted from atoms.

Geometrical phase mismatch is due primarily to the Gouy shift, which is a wavelength-dependent phase change that all light beams experience when it goes through a focus [22]. The phase of a laser going through a focus is given by

$$\phi = \tan^{-1}\left(\frac{z}{z_0}\right) \tag{1.2}$$

where z is the axial distance from the laser focus and z_0 is the laser Rayleigh range. Harmonics are generated with a phase of q (harmonic order) times this phase of the laser. Thus, the phase of generated harmonics will cycle through 2π many times through the generation region. This phase mismatch is most pronounced for higher harmonic orders.

We can estimate the coherence length for Gouy phase mismatches for laser parameters similar to our own. The coherence length is the distance over which a harmonic

order q gets out of phase by π with harmonic orders emitted downstream. The phase of a harmonic q at axial locations near the focus is given by

$$\phi_q = q \tan^{-1}\left(\frac{z}{z_0}\right) \approx \frac{qz}{z_0} \tag{1.3}$$

The phase difference in harmonics emitted at axial positions z_1 and z_2 is given by

$$\Delta\phi_q \approx q\frac{z_2 - z_1}{z_0} \tag{1.4}$$

If we let this phase difference $\Delta\phi_q$ be π with the Rayleigh range given by $z_0 = \pi w_0^2/\lambda$ where w_0 is the beam waist and λ is the laser wavelength, then the coherence length for the Gouy phase mismatch is given by

$$\Delta z_{\text{Gouy}} = \frac{w_0^2\pi^2}{\lambda q} \tag{1.5}$$

For typical values of $w_0 = 30$ μm and $\lambda = 800$ nm with $q = 57$, for example, the coherence length due to geometric phase mismatches is $\Delta z_{\text{Gouy}} = 200$ μm.

Another source of phase mismatch is dispersion, because the gas (like all materials) has a frequency-dependent index of refraction. If the laser and a harmonic travel through the gas with different phase velocities, harmonics generated by the laser at one point in the medium join out of phase with harmonics generated at previous points. This effect becomes especially significant as the laser partially ionizes the gas and creates a plasma. In a plasma, the difference in index for the laser versus the harmonics is much larger than in a neutral gas.

The index of refraction for a plasma is given by

$$n = \sqrt{1 - \frac{\omega_p^2}{\omega^2}} \approx 1 - \frac{1}{2}\frac{\omega_p^2}{\omega^2} \tag{1.6}$$

where ω is the laser frequency and ω_p is the plasma frequency. The approximation in equation 1.6 is typically good since the laser frequency is usually much higher than

the plasma frequency. The plasma frequency for an ionized gas is

$$\omega_p = \sqrt{\frac{Pe^2}{kT\epsilon_0 m}} \tag{1.7}$$

where P is the pressure (ionized), e is the electron charge, k is Boltzmann's constant, T is the temperature, ϵ_0 is the permittivity of free space, and m is the electron mass. The coherence length Δz_{plasma} can be written as

$$\Delta z_{\text{plasma}} = \frac{\lambda\omega^2}{q\omega_p^2} = \frac{4\pi^2 c^2 kT\epsilon_0 m}{\lambda q P e^2} \tag{1.8}$$

Substituting in for physical constants with $T = 300$ K, $\lambda = 800$ nm, and $q = 57$ generated in 50 torr of neon with 5% of the generating medium ionized, the coherence length due to plasma generation is about $\Delta z_{\text{plasma}} = 300$ μm.

Gouy phase shift and frequency-dependent index are two aspects of conventional phase mismatches. Also important are intrinsic phase mismatches, or phase mismatches that arise from spatial variations in laser intensity both axially and radially as the laser focuses. Because the phase of emitted harmonics depends on the laser intensity, the phase of emitted harmonics will vary depending on their generating atom's radial and axial location in the focusing beam. Spatial intensity variations can affect other aspects of HHG as well. As the laser begins to focus, the highest intensities are on-axis, and thus the highest density of free electrons created in the generating medium is on-axis. This creates a lensing effect that disrupts the natural focusing of the laser, causing significant changes to the phase and intensity profiles. The high-harmonic generation process and the phase of the generated harmonics are strongly dependent on the intensity of the laser beam; thus defocusing of the laser can alter phase matching conditions dramatically from what would be expected in the absence of a plasma [23, 24]. This is especially important for the generation of harmonics in longer gas targets such as gas cells. On the other hand, gas filled hollow

fibers deal with this issue by preventing the laser from defocusing, although there are limitations to the amount of ionization they can tolerate while maintaining good phase matching.

Phase mismatches in high harmonic generation can be mitigated to some degree through various techniques [20, 25–27]. The most straight-forward method of minimizing geometrical phase mismatches is to use a gas jet or cell that is narrow relative to the depth of the beam focus. This limits the interaction region to a single geometrical coherence length to avoid destructive phase cancelations. The gas distribution produced by a typical gas jet can be as small as 300 μm [28]. This technique has the disadvantage of wasting much of the potential region where the laser intensity is sufficient to produce high harmonics that lies outside of this small volume. However, if the gas density is high enough, the reabsorption limit can be reached, even in a short gas jet or cell.

Milchberg et al. [29] showed that producing harmonics in a plasma waveguide could achieve phase-matched pulses for distances up to 2.2 cm at intensities sufficient to generate high harmonics. Durfee investigated the phase matching of HHG in a gas-filled hollow core fiber [20, 21] and was able to achieve extended coherence lengths of several centimeters in xenon, krypton, argon, and hydrogen gases. Tamaki et al. also used a gas-filled hollow fiber for HHG [30]. They found that the harmonic spectrum emitted from the fiber showed an intensity distribution significantly different from that in free space. By comparing the two harmonic distributions, they observed more than a hundred times enhancement around the 25th harmonic, which they attributed to macroscopic phase matching effects.

Another phase-matching technique that was pioneered by Prof. Peatross's group at BYU is quasi phase matching with counter-propagating light [31]. This technique uses weak interfering light to disrupt harmonic emission in specific regions of the

focus. The timing and duration of these counter-propagating pulses can be chosen appropriately to frustrate harmonic production in regions with undesirable phase, allowing the emission from the remaining regions to interfere constructively.

Harmonic generation has been investigated in the BYU group for the past decade. J. Sutherland, a former master's student, probed the focal region in a gas cell with counter-propagating pulses to determine where harmonics are produced [32]. Sutherland's work revealed that harmonics are phase matched over extended distances in a long gas cell. She found that in most cases only a single phase zone near the exit foil existed, and that the pressure was high enough and the coherence length long enough to reach the re-absorption limit in the case of neon. This was unexpected, since geometrical phase mismatches alone were expected to have produced several opposing phase zones within the HHG region. This extended phase matching suggests that laser self guiding plays a role in enhancing harmonic production in gas cells, a proposition supported by reports made by Tamaki [19] and Tosa [33] based on the observation of strong harmonic emission from thick gas cells.

To investigate this observed extended phase matching and to achieve the harmonic brightness needed for polarimetry measurements introduced in section 1.4, former master's student, John Painter, and myself characterized the spatial profile and spectrum of the laser in the region of harmonic generation, along with the brightness of the associated harmonic emission. These measurements are discussed in chapter 2. We observed several interesting features of the generating laser, including a flat-top intensity profile and a double focusing of laser fluence in the region of harmonic generation. To help explain these experimental observations, we used a computational model developed by undergraduate Matthew Turner, which was able to reproduce our data remarkably well. We utilized these simulations to investigate the dynamic phase-matching of harmonics as the laser propagates in helium gas.

1.3 Applications of High Harmonic Generation

Several applications of high harmonic generation have emerged in the past decade. The next section gives an overview of the high-harmonic application of EUV polarimetry, which is the subject of this dissertation. We first mention in this section some other exciting applications of high-order harmonics. A recent development is the generation of attosecond pulses. Attosecond pulses open a new field where atom and electron dynamics can potentially be probed with temporal resolution sufficient to capture the dynamics of quantum transitions. As mentioned earlier, harmonic generation occurs within a fairly narrow time interval compared to the full half-cycle of the laser. Thus harmonics naturally emerge as trains of attosecond pulses.

For many applications, single attosecond pulses (one burst per laser pulse) are preferred. They emerge naturally from atoms driven by few-cycle pulses (less than 5 fs) [13]. With these ultrashort generating pulses, only the electron accelerated by the central half-wave cycle possesses enough energy to contribute to the high-harmonic emission. With longer generating pulses, a single attosecond pulse may be isolated from the train of attosecond pulses that naturally emerge from harmonic generation. This process, called pulse gating, has been implemented successfully using state-of-the-art lasers and innovative techniques. A common method for isolating a single attosecond pulse from the train in which they naturally occur is called polarization gating, shown schematically in Figure 1.5. This technique, first proposed by Ivanov et al. [34], splits the generating laser into two parts, making one part right-circularly polarized and one left-circularly polarized. These two parts are then re-combined, with one part delayed in time relative to the other. Because harmonic generation is disrupted when the generating laser has any ellipticity, neither of the two parts of the driving laser can generate harmonics on their own. However, when the dual

pulse switches from right- to left-circularly polarized (i.e., where the pulses overlap with equal amplitude), the generating laser has linear polarization and can generate harmonics in a single half laser cycle. Still, to work well, polarization gating requires a generating laser with pulse durations less than 10 fs. Currently, these few-cycle generating pulses can be made with maximum energies of a few millijoules, which limits the energy of the interaction [35].

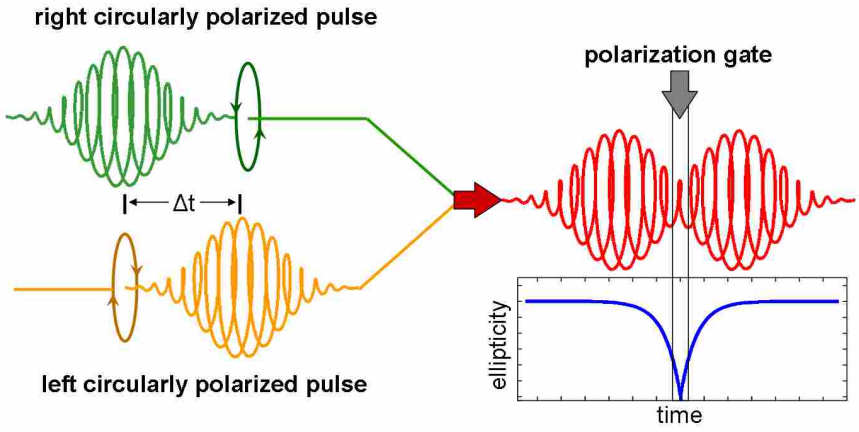

Figure 1.5 Polarization gating isolates a single attosecond pulse using a generating laser with a time-dependent ellipticity. Under this field, harmonics are only generated in the small time window where the ellipticity is close to zero.

Attosecond pulses have already been used for several novel applications. In 2004, Goulielmakis et al. [36] used a 250 attosecond probe to directly trace out the electric field of a short, few-cycle visible laser light pulse, shown in Figure 1.6(a). The measurement technique is shown schematically in Figure 1.6(b). A few-cycle pulse of laser light to be measured, together with a synchronized attosecond EUV pulse, is focused into a gas target where the EUV pulse ionizes the atoms. The laser light imparts a momentum change to the ionized electrons, which is measured by an electron detector. Direct probing of light-field oscillations represents an exciting new metrology tool. It has been postulated that attosecond pulses may eventually be used to

measure and manipulate molecules and atoms on unprecedented time scales.

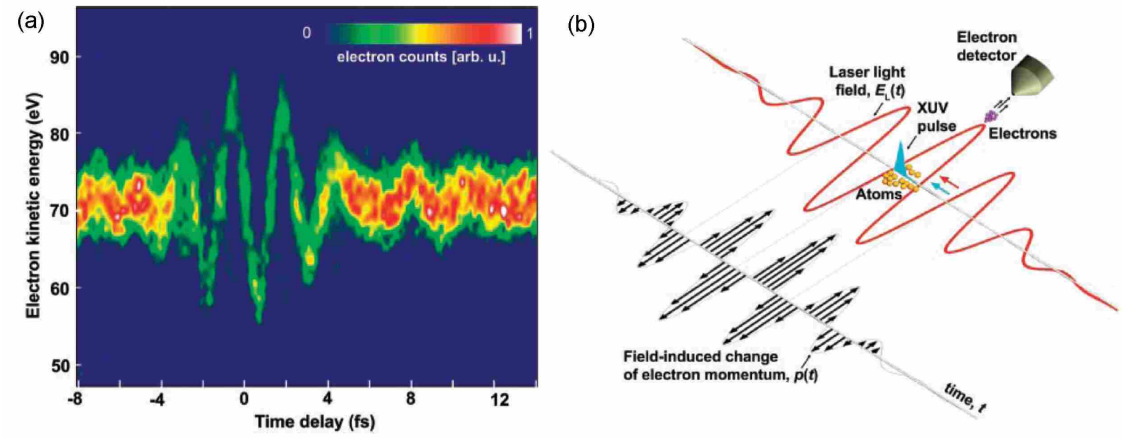

Figure 1.6 (a) The electric field of a 5 fs, 750 nm laser field measured using the kinetic energy spectra of electrons ionized from neon atoms by a 250-as EUV pulse. (b) Schematic of the measurement principle. The attosecond pulse ionizes electrons in a gas where the laser field then imparts them a momentum kick. This kick is proportional to the electric field of the laser, which can be measured using an electron detector (figure taken from [36]).

In another unique application, high harmonic generation has been used to reconstruct the electron orbitals of the very molecules used to generate high harmonics, a technique called tomographic imaging. Molecules are aligned with a pump laser pulse, then harmonics are generated with a second laser pulse. The emitted harmonic signal can be interpreted to extract spatial information about the ionized electron's orbital. By changing the relative angle between the alignment of the molecules and the polarization of the harmonic-generating laser, one can build up a set of projections of the molecular orbital. These can be inverted by using an algorithm based on computed tomography [37], resulting in an image. This is shown for a nitrogen molecule in Figure 1.7, along the corresponding calculated orbital [38].

Another application of high-order harmonics is in high resolution EUV microscopy. Short-wavelength microscopy techniques are currently being pursued at synchrotron sources, with the best image resolution demonstrated to date, 15 nm, being obtained

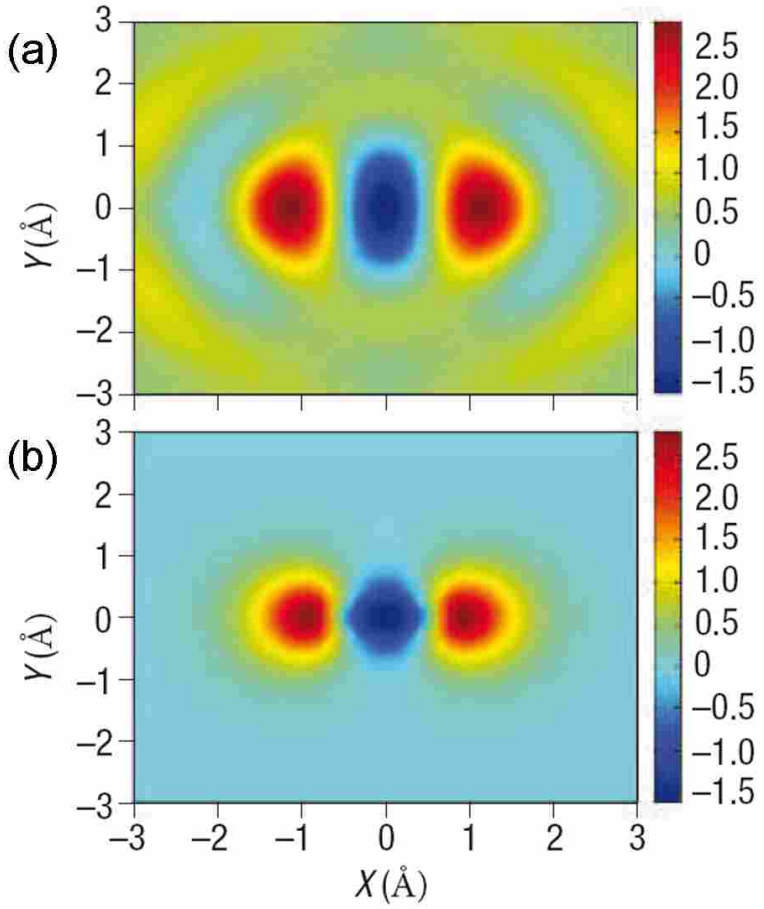

Figure 1.7 (a) The orbital shape of the highest occupied molecular orbital of N_2 is tomographically imaged by recording the high harmonic spectra from molecules aligned at different angles relative to the laser polarization direction. (b) The calculated orbital is shown for comparison (figure taken from [38]).

at the Advanced Light Synchrotron source at Lawrence Berkeley National Labs [39]. EUV and soft x-ray imaging techniques have important applications in biological imaging in the water window [40, 41], research on magnetic nanostructures with both elemental and spin-orbit sensitivity [42], and studies that require viewing through thin windows, coatings, or substrates (such as buried electronic devices in a silicon chip) [43]. High harmonic sources of EUV light show promise as a coherent, compact source of EUV light for similar imaging applications that would provide greater access for EUV microscopy applications. A high harmonic EUV source is being implemented for compact imaging systems [44]. Researchers at the Coherent X-ray Research Center (CXRC) have recently developed zone plate lenses to image nano patterns with a resolution better than 100 nm [45]. Figure 1.8 shows an images of 200 nm and 150 nm nano pattern imaged with a high harmonic source.

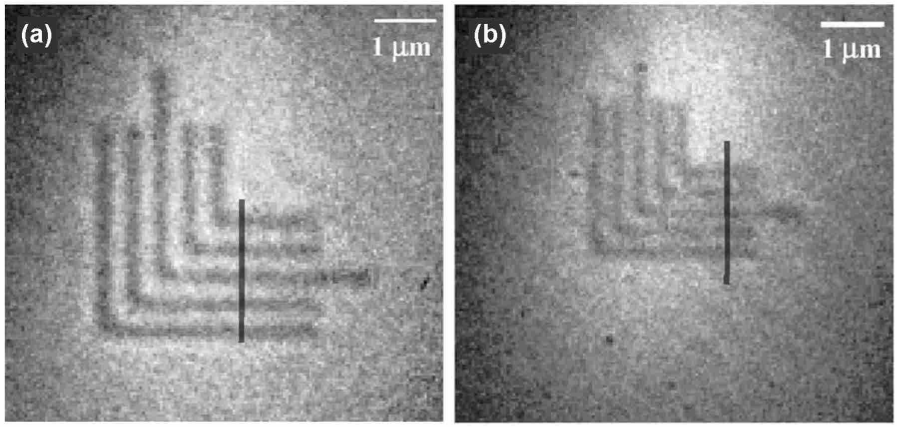

Figure 1.8 Nano elbow pattern pictures obtained using a high-harmonics-based soft x-ray microscope. (a) 200 nm width elbow pattern. (b)150 nm width elbow pattern (figure taken from [45]).

1.4 Extreme Ultraviolet Polarimetry Based on High Harmonic Generation

A large part of this dissertation describes the development and use of a polarimeter instrument based on high harmonic generation useful for measuring the optical constants of materials in the extreme ultraviolet wavelength range. This work represents one of the first applications where high harmonics are employed in a work-horse setting to make measurements important to another field, rather than just demonstrating proof of principle. The full instrument can determine the reflectance from samples as a function of incident angle, light polarization orientation, and wavelength (associated with a discrete comb of odd harmonics of 800 nm, up to order ∼81). We are able to measure reflectance from a wide comb of wavelengths simultaneously (with a much wider range of available wavelengths due to a rotatable grating). The polarization of the high harmonics is easily rotated with a half-wave plate in the incident beam. A schematic of the instrument is shown in Figure 1.9.

The polarimeter instrument allows characterization of materials at EUV wavelengths. Extreme ultraviolet light is becoming increasingly important in fields such as lithography (for producing integrated circuits), space-based astronomy, and microscopy [46–48]. However, because EUV energies are comparable to electron binding energies, virtually all materials that might be used for optical elements are highly absorptive in most of this wavelength range. Thus, transmissive optics are for the most part precluded, and reflective optics typically require multilayer coatings to reach feasible reflectivities. To design such multilayers, the indices of refraction of coating materials need to be well characterized. Unfortunately, the optical properties of many materials in this wavelength range are unknown or not completely characterized [49–51].

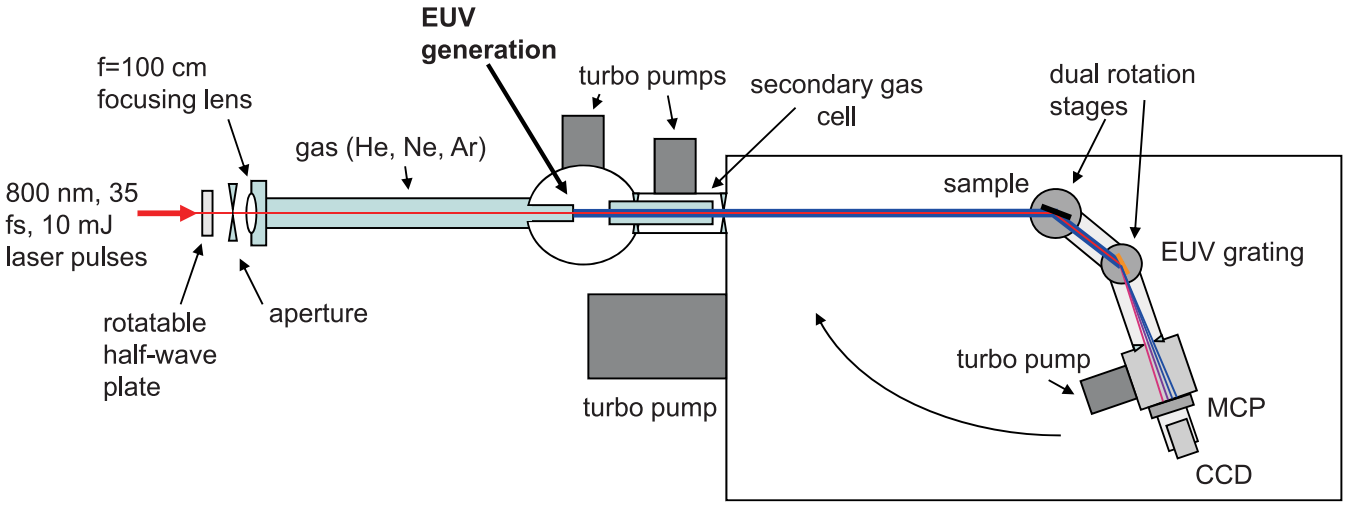

Figure 1.9 Polarimeter schematic (top view). 800 nm, 35 fs, and 10 mJ laser pulses are focused into a cell of helium, neon, or argon gas to generate harmonics. A half-wave plate in the generating laser rotates the linear polarization of the laser and harmonics. Harmonics emerge from the focus in a narrow beam, which travels through the secondary gas cell to the sample. Reflected harmonics are separated and focused with a grating and imaged onto a MCP.

The EUV research group at Brigham Young University (BYU), directed by Professor David Allred and Professor Steve Turley, produced mirror coatings that were used on the IMAGE satellite, which was launched March 25, 2000 [52]. This instrument took the first series of pictures of the Earth's magnetosphere at 41 eV as part of a comprehensive multi-spectral imaging of the near-space around Earth. The mirror coatings used in the satellite were uranium/silicon multilayers, and needed high reflectance (greater than 20%) at 30.4 nm, 14 degrees from normal and low reflectance (less than 2%) at 58.4 nm. The design work for this project was hampered by the fact that the index of refraction, or optical constants, for the uranium differed significantly from previously determined values. Researchers in the last decade, including those at BYU, have realized the need to expand and verify optical constants of materials in the EUV.

The complex index of refraction of a material is typically obtained by measur-

ing reflectance and/or transmittance of the material as a function of sample angle, wavelength, and polarization. Reflectance or transmittance measurements are defined as reflected or transmitted light intensity divided by incident light intensity, giving a percentage reflected or transmitted light for each sample angle. Reflectance or transmittance data can be fit to the theoretic reflectance or transmittance to obtain the complex index of refraction, N, which includes the real part, n, and the imaginary part, κ. The parameters δ and β are essentially interchangeable with n and κ, where $n \equiv 1 - \delta$ and $\kappa \equiv \beta$. The set of n and κ (or δ and β) are referred to as optical constants. Previous to this work, the EUV research group at BYU made reflectance and transmittance measurements for this purpose at the either at BYU using a monochromator with a plasma light source or at the Advanced Light Source (ALS) synchrotron at Lawrence Berkeley National Labs in Berkeley, California. The process of making reflectance measurements is commonly referred to as reflectometry. When reflectometry is performed using a variable-polarization light source, the process is called polarimetry.

Previous work in the EUV group includes measuring the optical constants of uranium oxides [53], uranium nitride [54], thorium dioxide [55], and scandium oxide [56]. Along these same lines, the EUV research group at BYU has also furthered techniques for determining optical constants to a greater degree of accuracy. These techniques include measuring and fitting reflectance and transmittance data simultaneously [57], determining the effect of surface roughness and interfacial diffusion on reflectance data [58], and exploring the accuracy of utilizing Kramers-Kronig relations to find optical constants [59]. All of these important developments in the understanding of materials in the EUV are hampered by the fact that BYU's monochromator does not have the flux nor the wavelength range of the ALS. However, the ALS is located in Berkeley, California, requiring significant time and travel expenses to make

measurements there. Because optical properties are intertwined with surface characteristics and thin-film preparation procedures, it is of significant advantage to have a polarimeter with sufficient source brightness and energy range co-located with sample preparation and characterization instruments at BYU.

Chapter 3 of this dissertation describes in detail the polarimeter instrument, which I constructed. We have found that our high harmonic source has sufficient flux for reflectance measurements with wavelength coverage from 10 nm to 47 nm. By using laser energy discrimination and averaging many laser shots, are able to reduce fluctuations in our incident light intensity to within 0.5% (although our system still suffers from rather large systematic errors, which can be mitigated using the technique described in chapter 5). Our positioning system is versatile. The instrument allows for a spectral resolution ($\lambda/\Delta\lambda$) of about 180 if electronic adjustments to the position of high-harmonic peaks within the images are made.

We have measured reflectance as a function of angle of a thermally oxidized silicon sample and found that these measurements are repeatable and accurate. These measurements are documented in chapter 4. The measurements agreed with reflectance curves calculated using the optical constants of silicon and silicon dioxide, which are well known [60].

In chapter 5, we describe a method for reducing systematic errors in our data by extracting optical constants from the *ratio* of p- to s-polarized reflectance, rather than absolute reflectance of either polarization. We have found that ratio reflectance curves are much more repeatable than absolute reflectance curves because they are less susceptible to noise and systematic alignment errors and we are able to extract optical constants from these measurements as efficiently as from absolute reflectance measurements. Thus, the ratio reflectance approach makes for more viable polarimetry with laser produced high harmonics, with the advantages of relatively low cost,

small footprint, and opportunity for *in-situ* measurements.

In chapter 6 we describe how we used the polarimeter along with the ratio reflectance technique to determine the optical constants of copper and uranium thin films and their natural oxides in the wavelength range from 10 nm to 47 nm. We were able to evaporate copper and uranium films inside our polarimeter, then make reflectance measurements without breaking vacuum (*in-situ* measurements), thus avoiding oxidation and contamination problems. We found that the optical constants of copper and uranium had not been well characterized previous to this work. Previously accepted values for copper in this range were actually the constants of oxidized copper. Uranium has been postulated as a high-reflectance material in the EUV since the mid 1990s [61]. In fact, uranium/silicon multilayer mirrors were used on NASA's IMAGE satellite launched in 2000 to image the earth's magnetosphere in the EUV [52]. However, difficulties with oxidation have prevented the careful measurement of the optical constants of uranium metal for many years. Here, we have characterized the optical constants of uranium and naturally oxidized uranium for the first time in this wavelength range. We find that these values do not agree well with previously accepted theoretical calculations.

Chapter 2

High Harmonic Source

In this chapter we discuss the high harmonic source used for polarimetry measurements described in later chapters. The development of the high harmonic generation techniques described here made it possible to achieve the brightness needed to perform these polarimetry measurements. We describe in detail the laser system used to generate harmonics. We also characterize the spatial evolution of the laser pulse as it propagates within a gas cell while generating harmonics [62, 63]. Along with this, we document the evolution of the brightness of the associated high-harmonic emission. These measurements show evidence of a double focus in the laser fluence, with the best harmonic emission occurring from the region between the double focus. We also observe that the laser exhibits a flat-top intensity profile at this location. This flat-top profile has previously been associated with laser self guiding and extended phase matching in neon [33, 64]. However, the double focusing we observe was unexpected in this description. We have undertaken computational modeling of laser beam propagation to explain these phenomena as well as the effect of partially closing an the aperture on the laser beam [65]. We find that the observed double focus in the fluence arises from a combination of the back of the pulse which is distorted

due to plasma generation and the undistorted front of the pulse. This simulation also includes the aperture effect, which linearizes the Gouy shift, allowing it, together with the phase error arising from a limited amount of plasma, to effectively cancel deleterious phase-mismatches due to dispersion in the neutral gas.

2.1 Laser System

The laser system we use to generate harmonics is a Ti:sapphire, 10 mJ laser that delivers pulses at a repetition rate of 10 Hz. The laser pulses are centered on 800 nm with an amplified bandwidth of 35 nm (FWHM). We recently reconfigured the laser system for purposes of achieving higher pulse energy, and the following is a description for the reconfigured system. A schematic of the entire laser system is shown in Figure 2.1. The laser pulses originate in a passively mode-locked Ti:Sapphire oscillator cavity made by KMLabs, which uses a continuous 532 nm Coherent Verdi laser as the pump source. The Ti:sapphire cavity produces a train of $\sim$15 fs pulses separated by 11 ns (the time for a round-trip through the cavity) with a wavelength centered around 800 nm. This is equivalent to a repetition rate of 91 MHz and this pulse train beam has a average output power of about 600 mW.

After emerging from the oscillator, isolated pulses (selected at 10 Hz) enter a chirped pulse amplification (CPA) system, which consists of a stretcher, two amplification stages, and a compressor. The CPA approach was first introduced by Strickland and Mourou [66] in 1985. Before that time, the peak power of laser pulses was much more restricted because high intensities cause self-focusing in amplification crystals due to the optical Kerr effect, leading to distortions in the spatial and temporal profiles of a pulse. In chirped pulse amplification, the ultrashort laser pulses coming from the oscillator are stretched in time using a pair of diffraction grat-

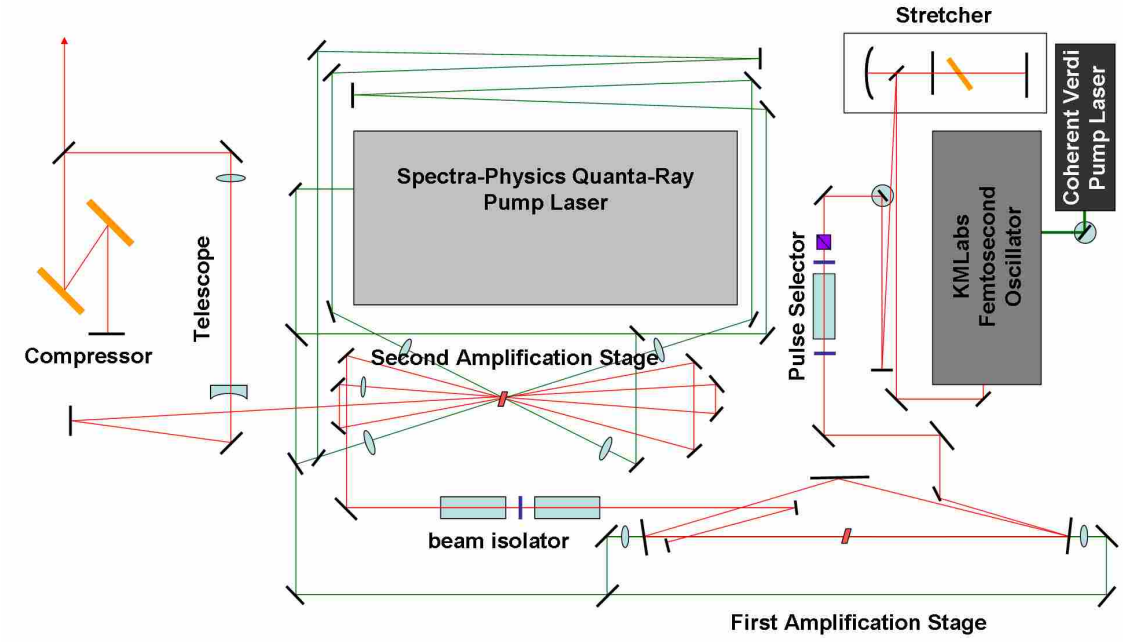

Figure 2.1 Schematic of the laser system used to generate high harmonics.

ings that are arranged so that the long wavelength component of the pulse travels a shorter distance than the short-wavelength component. Thus, after traveling through the stretcher, the pulse is positively chirped and stretched in time, with the long wavelengths in the front of the pulse and the short wavelengths in the back of the pulse. This lengthening in time reduces the intensity of the pulse by a factor of about 10^3 [67], allowing amplification without damaging the crystal or distorting the pulse. After amplification, the laser is sent through a set of compression gratings which reverse the process of the stretcher, re-compressing the pulse in time and allowing a very energetic, short-pulsed beam.

We use an all reflective, single-grating stretcher design. The stretcher expands the ~15 fs pulses coming from the oscillator to about 70 ps [68]. After the stretcher, the beam enters the pulse selector system. The pulse selector takes the pulse train arriving from the oscillator at a rate of 91 MHz and selects pulses at 10 Hz, which is

the repetition rate of our pump laser, using a Pockels cell. A Pockels cell is a KPD crystal with an electrically-induced birefringence that rotates the polarization of the incoming light when a high voltage is applied. When no voltage is applied, the Pockels cell allows the pulses to pass through unchanged. Voltage is applied to the Pockels cell for approximately 10 ns at a repetition rate of 10 Hz. This high voltage rotates the polarization for a single pulse, from s- to p-polarization. A polarizer placed after the Pockels cell rejects the s-polarized pulses but transmits the p-polarized pulses that arrive at a repetition rate of 10 Hz.

The amplification in our system is performed in two Ti:sapphire-based stages. Ti:Sapphire lases over a wide spectral range peaked and centered around 800 nm. During amplification, a pulse can suffer modest narrowing of its spectrum, which adds to the pulse duration upon recompression. The first amplification stage is shown in Figure 2.2. The beam enters at the injection mirror M6. The mirrors M7 and M8 are concave dielectric mirrors of focal length 50 cm that reflect 800 nm light and transmit 532 nm light. The mirrors are located 100 cm from each other, forming a triangle arrangement together with a wide flat mirror M9. The Ti:Sapphire crystal (produced by Saint Gobain Crystals) is a 0.25% doped, Brewster-cut, 7 mm thick crystal. This crystal is centered between the mirrors M7 and M8. The seed pulses make 9 passes clockwise around the triangle formed by the mirrors M7-M8-M9. On each pass, the beam hits a slightly different place on each of the mirrors but passes through the same point in the amplifier crystal. On the ninth pass, the amplified pulse is extracted from the amplifier with a pick-off mirror (M10).

Both amplification stages are pumped with a 532 nm Spectra-Physics Quanta-Ray laser, which produces s-polarized light pulses with 12 ns duration and energy up to 700 mJ at 10 Hz. About 12% of the Quanta-Ray laser is used to pump the first amplification stage where it is split into two equal parts with BS1. These two beams

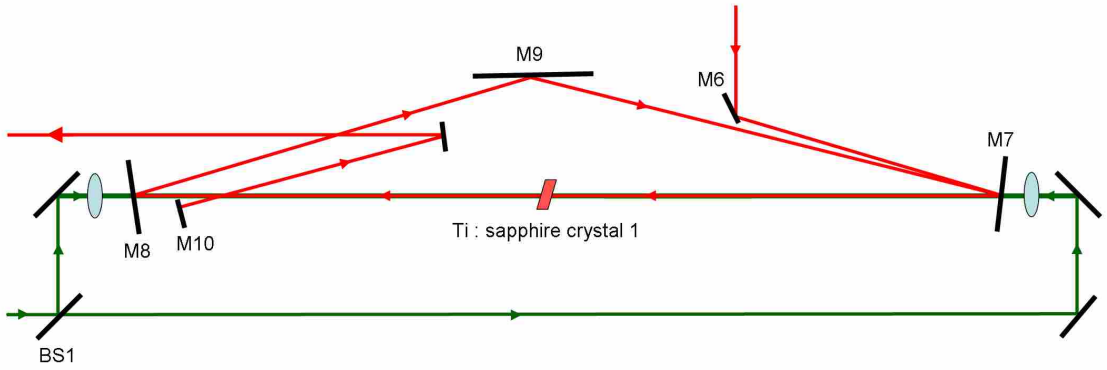

Figure 2.2 Schematic of the first amplification stage. This stage amplifies ∼7 nJ pulses to about 5 mJ.

are focused with f=50 cm lenses to points 5 cm past the Ti:sapphire crystal in both directions. The mirrors for the infrared beam triangle, M7 and M8, are reasonably transparent to the 532 nm pump beam. After the first amplification stage, the infrared beam typically reaches energies of 5 mJ at a repetition rate of 10 Hz. The overall gain of this amplifier stage is therefore about 10^6.

The infrared beam exiting the first amplification stage next enters the beam isolator setup, which uses two Pockels cells to eliminate any light due to spontaneous emission or satellite pulses we wish to eliminate from our beam. This setup also ensures that any stray light that may be traveling through the system backwards is removed, since this light could potentially damage optics in the first amplifier. The beam loses about 50% of its energy while traversing the isolator setup. However, most of this lost energy can be attributed to undesirable light that we wish to eliminate from our beam.

The second amplification stage is a four-pass system designed to amplify the beam to energies of 10-50 mJ. A schematic of this stage can be seen in Figure 2.3. The beam is inserted into the system with mirror M11, then proceeds in series to mirrors M12-M18, passing through the crystal four times. After the second pass, the laser is

sent through a f=-150 cm focal length lens (L1) designed to make the beam larger as it becomes more energetic, preventing damage to the crystal or other optics. The amplification in this stage is roughly a factor of 16, yielding a beam energy of about 40 mJ. After the beam exits the amplifier, it is up-collimated with a telescope to a beam diameter of about 1 in.

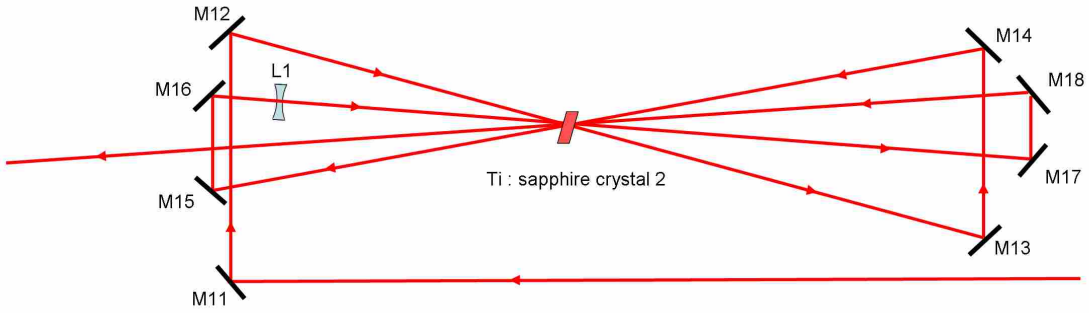

Figure 2.3 Schematic of the second amplification stage. This is a four-pass system that amplifies pulses to about 40 mJ.

The second amplifier stage is pumped with the 88% of the energy from the Spectra-Physics laser not sent to the first amplifier. This beam is split into four beams that enter the Ti:sapphire crystal from four angles, two from each side. This tends to wash out any spatial structure in the green pump beam that may cause spatial structure in the amplified infrared beam. A schematic of the beam path for this pump laser is shown in Figure 2.4. Two of the beams have longer path lengths than the other two. Thus, not all of the energy from the four pump beams arrive at the crystal at the same time to avoid damage. Each pump beam is focused to a spot about 10 cm beyond the crystal with lenses L2-L5.

The infrared beam coming from the second amplifier is compressed with a pair of gratings that reverse the process performed by the stretcher. The pulse duration measured by frequency-resolved optical gating (Swamp Optics UPM-8-9) after compression is about 35 fs.

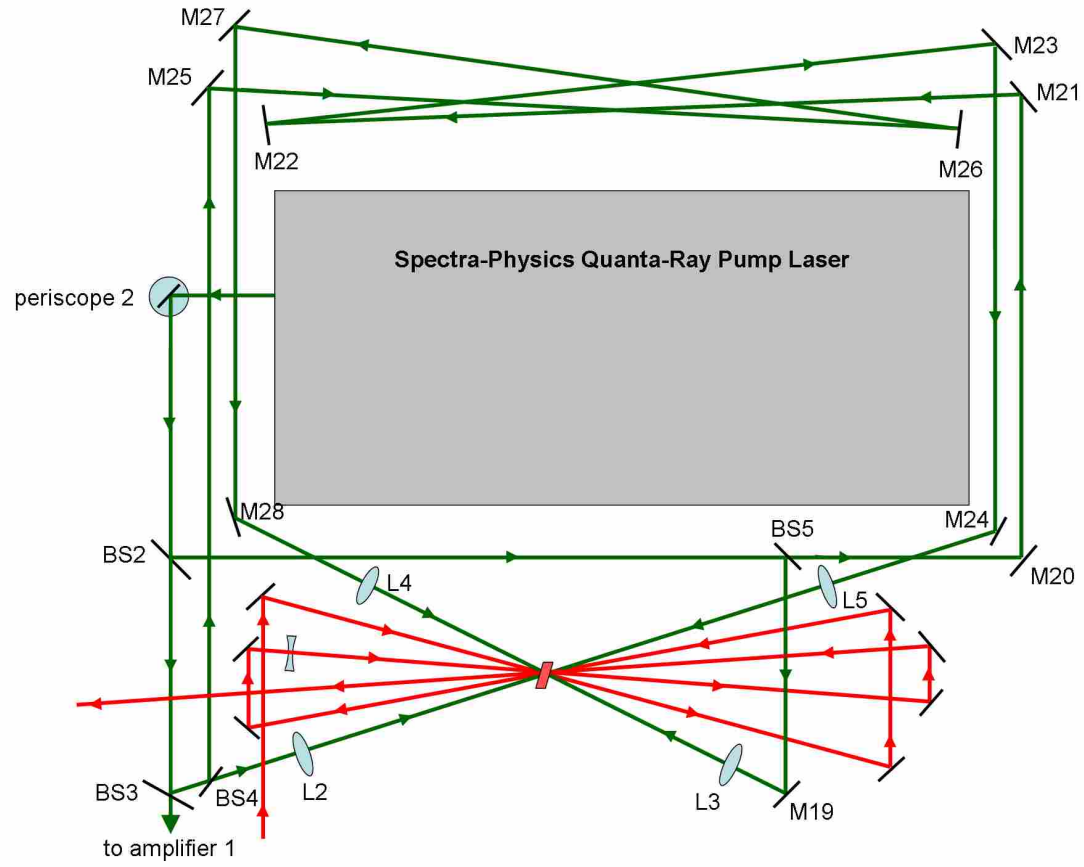

Figure 2.4 Schematic of pump laser for the second amplification stage. The pump laser is split into four beams that enter the crystal from four angles, two from each side.

2.2 High Harmonic Generation Experimental Setup

The amplified and compressed laser beam is focused with a 100 cm focal length lens or mirror into a cell filled with helium, neon, or argon gas (see Figure 2.5). This focusing achieves an intensity of about 1.3×10^{15} W/cm^2 in vacuum and approximately half that in the gas-filled cell which modifies the focus. An 8-10 mm aperture (closed on a $\sim$2 cm beam) located before the focusing optic was shown to strongly enhance harmonic emission [69]. A glass tube capped with molybdenum foil separates the region of gas from vacuum. This setup, where the gas-filled region extends from the focusing optic to the exit foil, is called a semi-infinite gas cell configuration and was shown to produce brighter harmonics than short cells of 6 mm or less [32]. The laser self-drills a hole in the molybdenum foil, eliminating the need for precise alignment. After harmonic generation, the harmonics exit into vacuum and co-propagate with the residual laser beam. The harmonics and laser proceed to the detection setup about 1.5 m away, passing through two small holes that provide for differential pumping. The harmonics are separated and focused in one dimension by a tungsten-coated EUV grating and are detected by a microchannel plate detector coupled to a phosphor screen. A visible-light CCD camera captures the image on the phosphor screen and relays it to the computer.

Figure 2.6 shows harmonics produced in 80 torr helium from the 45th to the 91st order, which have approximately uniform intensity. We measured the energy in an individual harmonic order to be about 1 nJ [63]. Higher order harmonics are diffracted with a 1200 line/mm grating with 2 m radius of curvature. Lower order harmonics, such as those produced in argon are diffracted instead with a 600 line/mm grating with a 1 m radius of curvature. We found that the best gas pressure for harmonic production in helium is about 80 torr, the best gas pressure for harmonic production

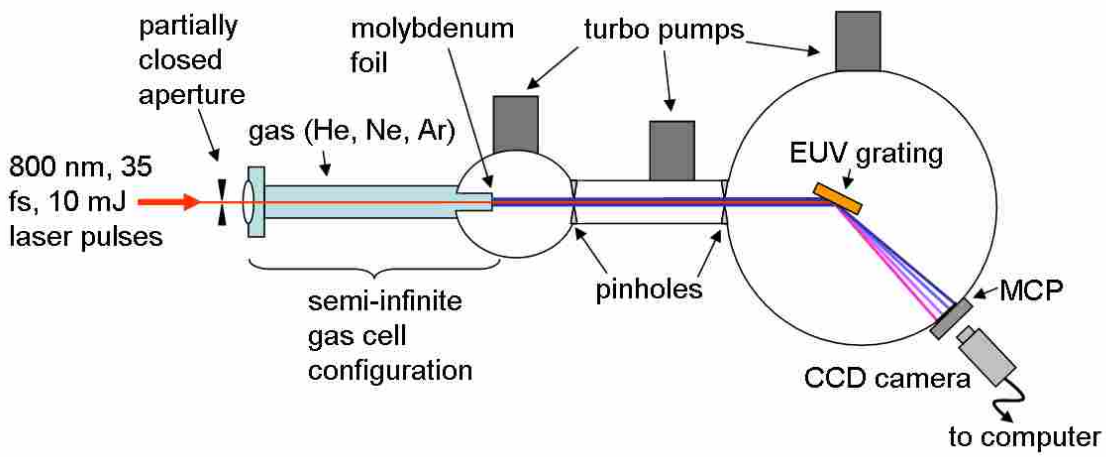

Figure 2.5 Harmonic generation and detection setup.

in neon is about 55 torr, and the best gas pressure for harmonic production in argon is about 12 torr. The intensity of the harmonics is not affected by gas pressure variation of ±5%.

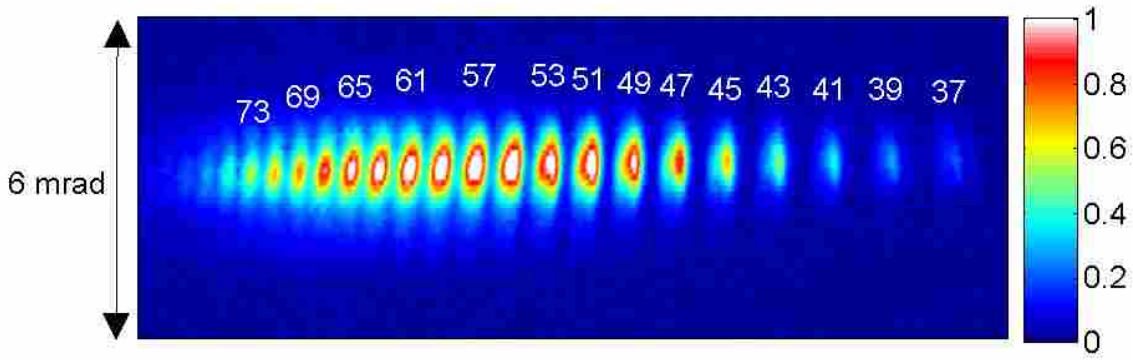

Figure 2.6 Harmonics of order 37-79 (wavelengths 10.1-21.6 nm) produced in neon gas.

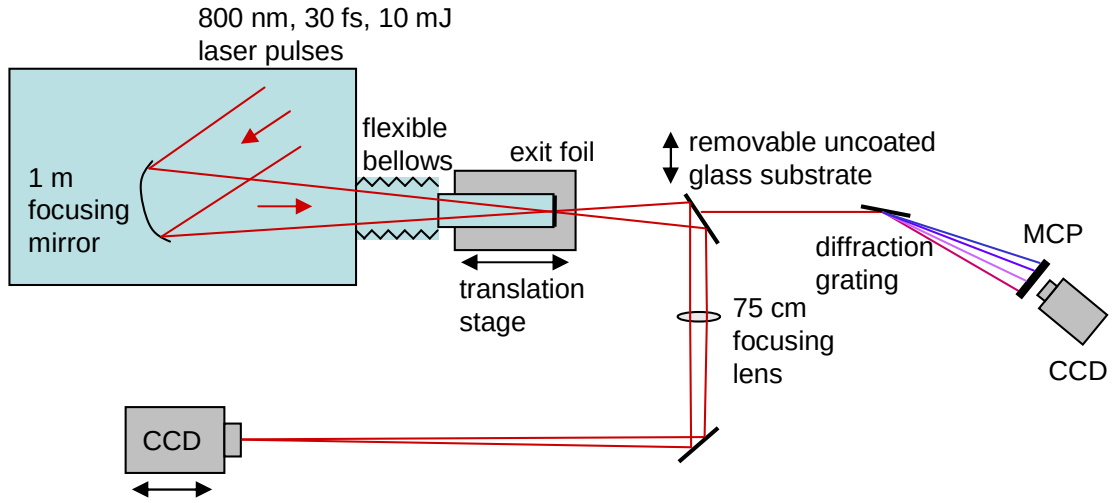

Figure 2.7 Setup to image laser beam spatial profile under conditions suitable for harmonic generation.

2.3 Effect of Focal Position on Harmonic Generation and Laser Profile

This section describes results highlighted in John Painter's master's thesis, but they are summarized here also since we worked together on the project and also published an article in this area. To image the spatial profile of the laser beam under conditions suitable for producing harmonics, an uncoated glass substrate oriented at 45 degrees was temporarily inserted in the beam before the harmonic-detection setup (see Figure 2.7). The glass substrate, which functioned both as a mirror and an attenuator, could be moved into and out of the laser beam in a matter of seconds while maintaining vacuum in the harmonic detection setup. The substrate reflected approximately 2% of the laser, which was imaged by an f = 75 cm focusing lens onto a CCD camera. Neutral density filters were used for further attenuation. The camera was positioned to image the laser at the plane of the exit foil of the gas cell. The position of the foil was scanned parallel to the laser axis over a range of 9 cm. The axial position of the

camera was also scanned to maintain an image of the laser beam at the exit foil. The magnification of the image was approximately 3×, depending on the exact location of the foil relative to the imaging lens.

Figure 2.8 shows plots of harmonics generated in 80 torr helium gas together with the evolution of the laser beam spatial profile as the foil position is varied. The left image shows the generated harmonics, the middle image shows the measured laser beam spatial profile, and the graph on the right shows a lineout of the laser beam spatial profile. The units on the laser image and beam lineout are scaled to the dimensions of the laser focus in the gas cell rather than the image size on the CCD. The z-position of the exit foil is measured relative to the focusing mirror (the beam focuses at 100 cm in vacuum). Each image is the average of 10 laser shots.

Figure 2.9(a) plots the beam diameter (FWHM) in both 80 torr helium and vacuum as the foil position is varied. In helium, the width of the beam reaches a minimum near $z = -3$ cm, widens to reach a maximum near $z = 0$ cm, and then narrows again to a second minimum at $z = 4$ cm. In vacuum the beam goes through a single focus, as would be expected. The z-position of the exit foil is measured relative to the 100 cm focal-length mirror. Figure 2.9(b), shows the intensity of several harmonic orders at the foil positions where the beam diameter in helium was measured. The best harmonic production is observed around $z = 0.5$ cm, where the laser in helium is changing from diverging to converging.

Figure 2.10 compares fluence lineouts of the laser beam focused in helium and in vacuum. The beam propagating in vacuum shows a Gaussian-like profile, which reaches a single minimum width with maximum fluence at $z = 0$ cm. The beam propagating in helium exhibits the double focus discussed above, and a distinct flat-top radial profile from about $z = -2$ cm to $z = 1.5$ cm. Although not immediately apparent from the lineouts, the two curves correspond to similar total energies. (The

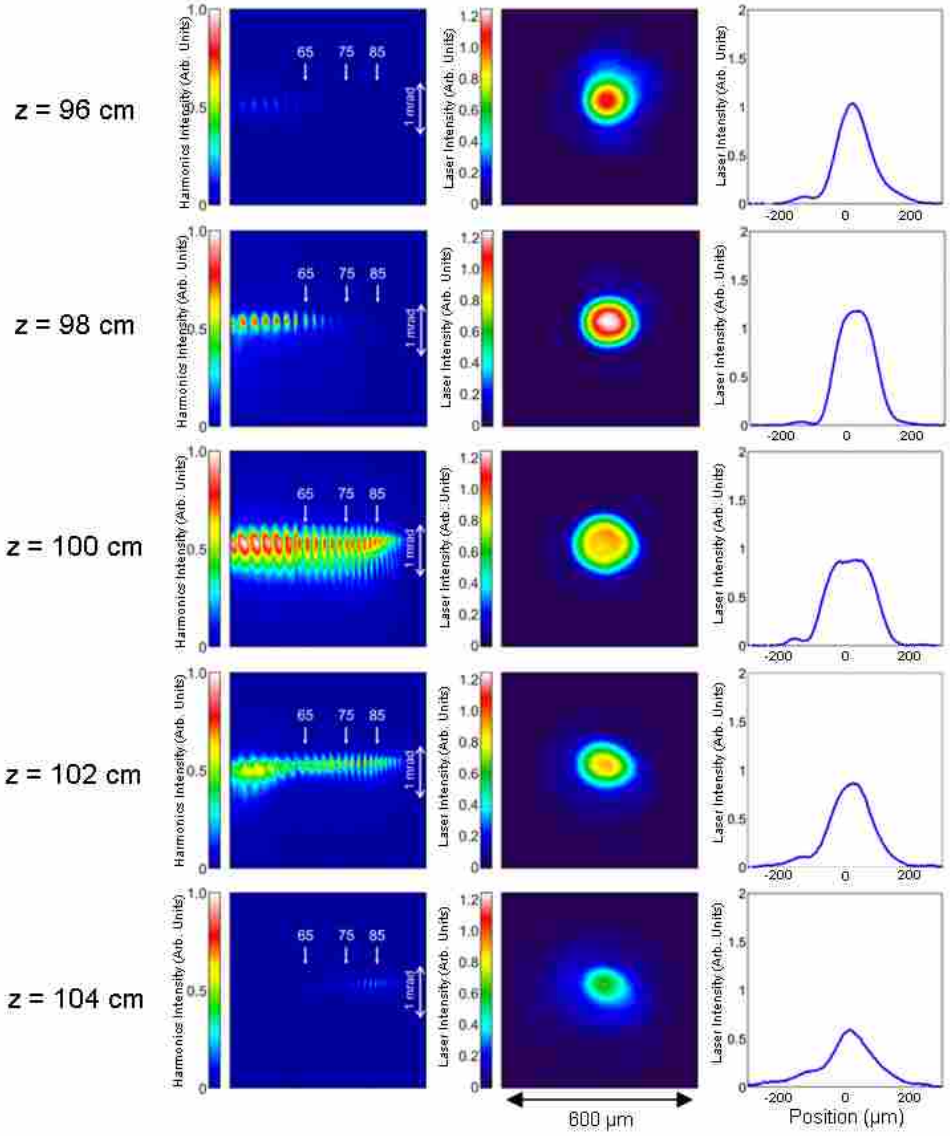

Figure 2.8 Harmonics (left), imaged laser beam (center), and beam lineout (right) for harmonics generated in 80 torr helium at four z positions (in vacuum the beam focuses at $z = 100$ cm).

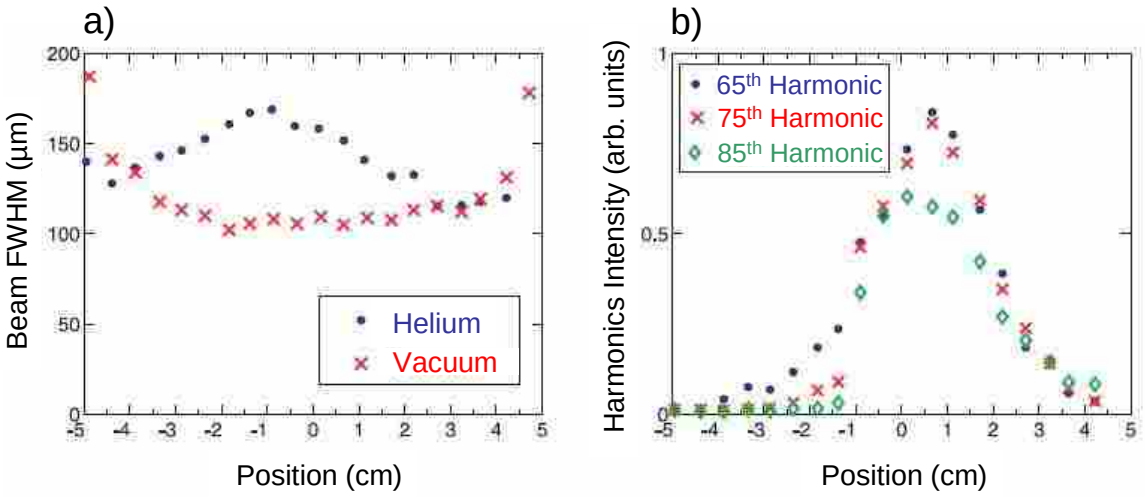

Figure 2.9 (a) Diameter of the laser as it exits from the gas cell, either filled with 80 Torr helium or evacuated. The best focus in the absence of gas occurs 100 cm after the focusing mirror. (b) The brightness of several harmonic orders as the foil position is varied.

fluence at wider radii is incident on a larger area, so in two dimensions the extra fluence in the wings of the profile in helium compensates for its lower on-axis fluence).

A flat-top fluence profile in the laser focus was previously associated with laser self guiding and extended phase matching in neon [33, 64]. Tosa et al. [33] calculated the radial intensity profile of a self-guided beam and predicted that it would exhibit a top-hat profile, owing to wavefront distortions from free electrons. Kim et al. [64] subsequently observed a radial intensity flattening in a single image produced for a laser that had traveled through a wide gas jet. The top-hat profile was attributed to defocusing of the laser by free electrons at inner radii. As the on-axis energy is defocused out to wider radii, it overlaps with the less intense outer portion of the laser beam still in the act of focusing.

While this explanation is consistent with the radial fluence distribution observed and laterally broadened wave fronts, it was not at first obvious how this could offer

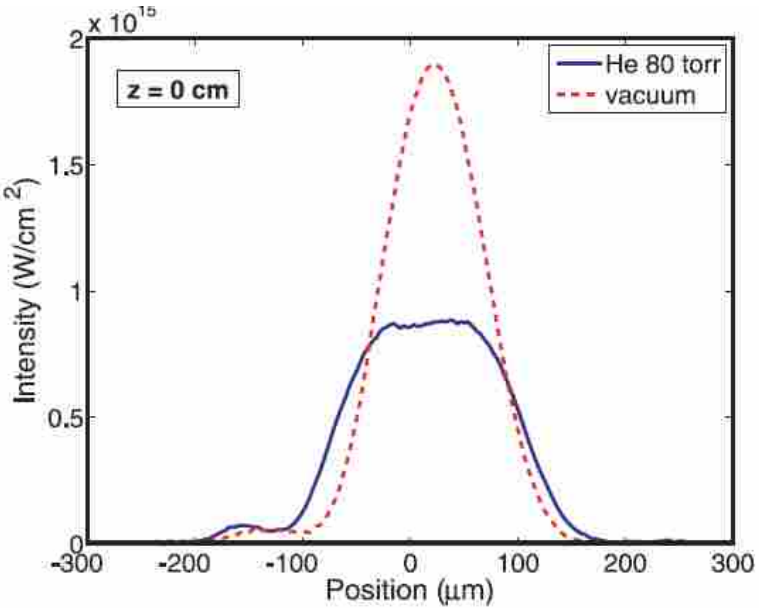

Figure 2.10 Lineouts of the laser focused in helium and in vacuum at the $z = 0$ cm position, or where the laser focuses in vacuum.

good longitudinal phase matching for high-harmonic generation, or how this could cause a re-convergence of our beam to a second focus, as seen in the data. The brightest harmonics are attained when the exit foil of the gas cell is positioned near the middle of the self-guiding region, where the beam diameter is large. This region of extended phase matching occurs where the laser beam changes from diverging to converging between the two foci. This is opposite in character to a conventional laser focus, which changes from converging to diverging while accompanied by the Gouy shift (known to be deleterious to phase matching). The interpretation of the data is complicated by the fact that the CCD camera measures energy fluence rather than intensity (technically a mislabeling of Figures 2.8 and 2.9). Our measurement technique is therefore unable to distinguish whether the entire pulse in time develops the flat-top profile as seen in the data, or whether different temporal portions of the pulse look spatially different.

We at first supposed that the double focusing observed in our laser beam as it

interacted with helium was suggestive of Kerr-style self-focusing, or filamentation. Placing a partially closed aperture in the laser beam before the focusing mirror could cause the observed laser focus to be smoother, possibly favoring the formation of a single filament rather than competing filaments. Nevertheless, the nonlinear index in 80 torr of helium is reported to be approximately 4×10^{-22} cm^2/W [70, 71], which predicts a critical power for filamentation in excess of 2 TW. In contrast, the power used in our experiments was an order of magnitude less. Tosa and coworkers [33] also indicate that the Kerr nonlinearity should be inconsequential.

Computational modeling of laser propagation in a gas was undertaken to try and explain these unexpected experimental results. These calculations, described in detail in section 2.5, show that all of our experimental results, including the observed double focus, arise from an interplay between the diffraction caused by the partially closed aperture and the dispersion caused by free electrons generated in the focus. The results appear to be consistent with the mechanisms described previously by Tosa et al. [33].

2.4 Effect of Focal Position on Laser Spectrum

A 50 μm fiber optic was swept through the laser image radially to test for variations in the spectrum resulting from the interaction with the helium. Taking into account the magnification in the imaging system, we determined that the effective spatial resolution of the scan corresponded to less than 20 μm in the actual focus. Figure 2.11 shows a Gaussian fit to the spectrum of the laser as the fiber is swept radially through the beam. A comparison is made between the cases of helium and vacuum when the exit foil of the semi-infinite cell is positioned at $z = 100$ cm. In vacuum, the laser spectrum is seen to be centered at 800 nm with a FWHM of 35 nm. As expected, the

vacuum spectrum exhibits no change as the fiber is moved through the laser image. For radii less than 70 μm, we observe a blue-shift of up to 4 nm of the laser focused in helium versus the laser focused in vacuum. The spectral blue-shifting of the center of the beam coincides with the onset of ionization (as suggested by a visible streak of plasma seen from the side of the focus), but other effects may also play a role [72].

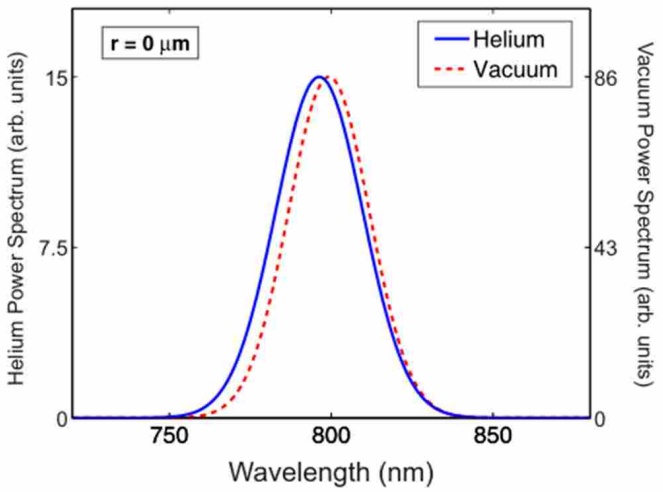

Figure 2.11 The spectrum of the radial center of the laser focused in vacuum and in helium. The laser focused in helium shows a 4 nm blue-shift, due to the onset of ionization.

2.5 Laser Profile Computational Analysis

Matthew Turner, an undergraduate student in our research group, wrote a program to simulate propagation of high-intensity laser pulses in helium. We used this program to investigate the role of nonlinear effects in our gas-cell high-harmonics experiments and to help explain the experimental results discussed in previous sections and the aperture effect described by Sutherland [32].

Our computational model is based on the method outlined by Chiron et al. [73], which uses the slowly-varying envelope and paraxial approximations to the scalar

wave equation, assuming radial symmetry and neglecting group velocity dispersion. In a moving frame, this equation is given by

$$\frac{2ik_0c}{\omega_0}\frac{\partial E}{\partial \eta} + \nabla_\rho^2 E + 2n_0\Delta n E = 0 \tag{2.1}$$

where E is the field envelope multiplying a plane wave oscillating at ω_0. The wave number k_0 is evaluated in the neutral gas medium with index n_0. The change in index due to the Kerr effect and plasma generation is given by $\Delta n \approx n_2 I - \omega_p^2/2\omega_0^2$. In helium gas, $n_2 = 3.5 \times 10^{-21}$ cm^2/W [74]. The plasma frequency ω_p, associated with free electrons, is determined using the ADK ionization model [75]. The variables $\eta = z/(c/\omega_0)$ and $\tau = \omega_0[t - \eta/(k_0c)]$ track the pulse in a moving frame, reducing computational load. Here, t is time, z is the axial propagation distance, and ρ is the radial position. Fresnel diffraction integrals are used to calculate the initial pulse profile 5 cm before the nominal beam focus, taking into account the effects of the aperture and the focusing optic on the incoming pulse. A Crank-Nicolson algorithm is used to propagate the pulse in the vicinity of the focus where nonlinear effects become important.

To check our computational model, we verified that the propagation of a Gaussian pulse in vacuum recovers the analytic solution. We also verified that our model recovers the Kerr effect as predicted by theory. The parameters for the simulation are chosen to be similar to experimental parameters: pulse duration is 35 fs FWHM, center wavelength is 800 nm, beam diameter ($1/e^2$) is 11 mm, pulse energy is $\sim$7 mJ, and the beam is focused with a 100 cm focal length optic. The simulation includes a 9 mm aperture placed 145 cm before the focusing optic. With the aperture in the beam the laser focuses in vacuum to an intensity of 1.3×10^{15} W/cm^2. The generation medium in the simulation was taken to be 80 torr of helium.

Figures 2.12(a) and (b) show the pulse intensity and the free-electron density,

respectively, as the pulse propagates 10 cm through the focus (i.e., from 96 cm to 104 cm after the focusing mirror). Each frame shows a snapshot of the pulse at locations 2 cm apart along the direction of travel. As seen in this figure, the early generation of plasma causes the back of the pulse to refract outward to form a ring. As described by Kim et al. [64], some beam energy at wider radii misses the plasma and continues to converge toward the axis downstream. This effect is enhanced for the apertured beam (which has an elongated focal region) and accounts for the dual focus in fluence we see.

As discussed in the previous section, we measured fluence profiles of our pulse in the region of the focus. Figure 2.12(c) shows a line-out of the time integrated intensity, or fluence in units of energy per area from the simulation. These radial fluence profiles exhibit several key features in agreement with experimental data, including the occurrence of a flat-top profile seen experimentally (see Figure 2.10, also reference [33]). The simulations reveal that the flat-top profile arises from the combination of the undistorted front of the pulse and the ring structure at the back of the pulse caused by plasma generation.

Figure 2.13(a) shows the peak pulse intensity and the on-axis fluence as a function of axial position in the focus. Our previous experimental fluence measurements are also shown for comparison. As is evident, the peak intensity continuously decreases after an initial maximum. In contrast, the fluence undergoes a second local maximum. This implies an increased pulse duration at that location. Figure 2.13(b) shows the full-width-at-half-maximum of the fluence as the pulse propagates in the simulation. Note that the simulation reproduces the experimentally observed double focus profile (also plotted in Figure 2.9). Importantly, the dual focus arises without the need for Kerr-style filamentation as we initially supposed. Including or not including the Kerr effect has almost no impact on the simulation. This dismissal of a substantial Kerr

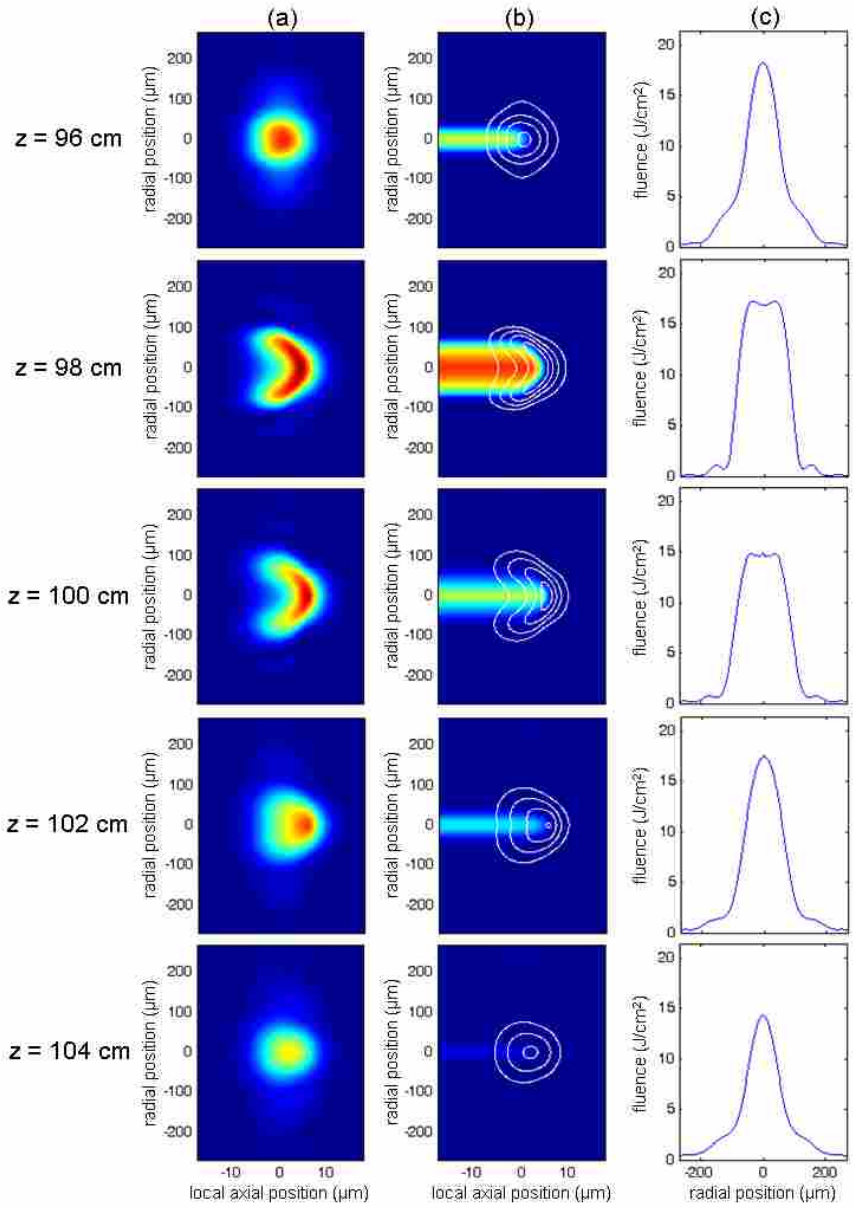

Figure 2.12 (a) The pulse intensity (dark red indicates the peak intensity of 5.7×10^{14} W/cm^2), (b) free-electron density (dark red indicates the peak free-electron density of 5.3×10^{22} electrons/m^3, equivalent to 2.1% ionization), and (c) fluence as the pulse propagates 10 cm through the focus. Each frame shows a snapshot of the pulse at locations 2 cm apart along the direction of travel. The contour lines in frame (b) indicate pulse intensity, with lines representing a 20% change in intensity.

effect is consistent with the fact that the peak power is an order of magnitude below the critical level for self-focusing. In contrast, if plasma generation is switched off in the simulation, the pulse propagation is virtually identical to that in vacuum.

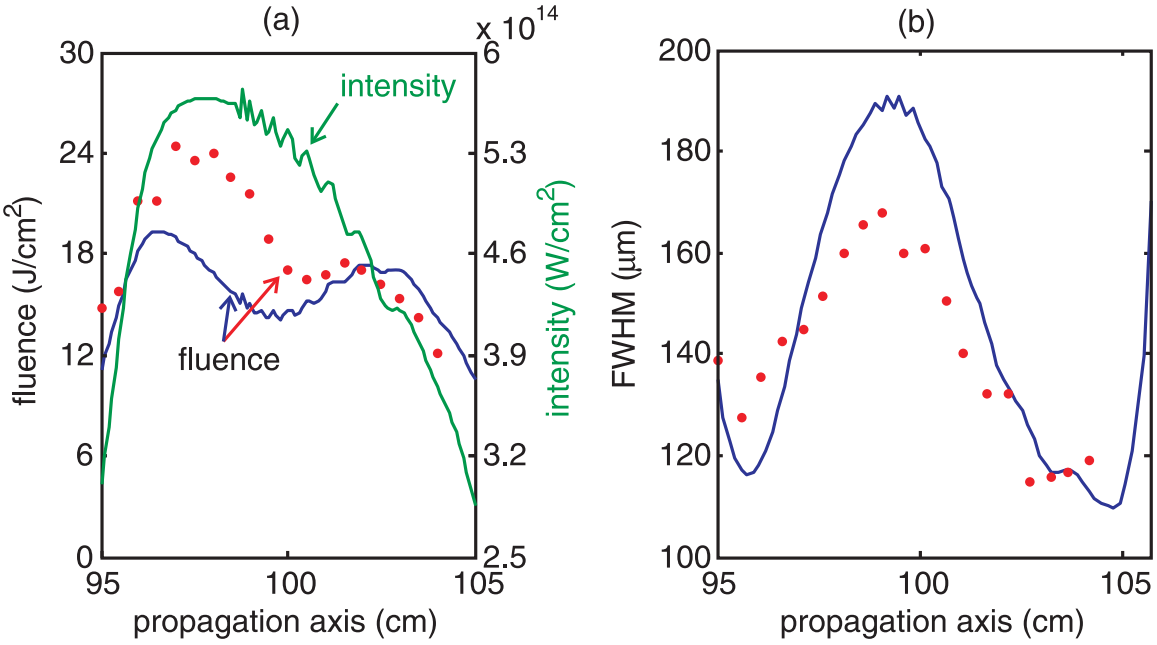

Figure 2.13 (a) The on-axis fluence from the experiment (dots) and simulation (line), and the calculated peak pulse intensity as a function of axial position in the focus. (b) FWHM values for the fluence along the propagation axis given by simulation (line) and by experiment (dots). The propagation axis location is given as a distance from the focusing optic (f=100 cm).

The spectral blueshift of the simulated pulse at the nominal focus is 6 nm, which is in reasonable agreement with the experimentally observed blueshift of 4 nm (see section 2.4). The overall agreement between the simulations and the experimental measurements lends confidence that the simulation code captures the essential physics of the pulse-medium interaction. The simulations can therefore be employed with reasonable confidence to investigate dynamic phase matching of high harmonics in our setup.

2.6 Computational Analysis of Phase Matching

As discussed in section 1.2, phase mismatches in the high-harmonics generating process come from two sources: (1) conventional phase mismatches, which arise from the Gouy phase shift and the refractive index of the neutral atoms and generated plasma, and (2) intrinsic phase mismatches, which arise from variations in the laser intensity. For harmonics generated in helium in the plateau, the intrinsic intensity-dependent phase is expected to follow $\phi_{intrinsic} = \pi I/2.5\times10^{13}$ W/cm^2 for our laser frequency [76] (based on $\phi_{intrinsic} = 5.8U_p$, where $U_p = 1$ in atomic units corresponds to a ponderomotive potential of 27 eV). This can easily produce phase errors greater than π if the intensity of a given point on the traveling laser pulse varies by more than a few percent as the pulse propagates. Figures 2.14(a) and (b) show the forward-directed coherence lengths for each point on the pulse, based separately on the conventional and the intrinsic intensity-dependent phase mismatches, respectively. The coherence lengths, which are for the 75th harmonic, are computed by comparing the phase at a particular point in a frame with the phase of the corresponding points in past frames to find the maximum distance wherein the harmonic phase varies by less than π. The coherence lengths were capped in the calculations at an estimated reabsorption limit of 2 cm [60].

The coherence length for the conventional phase shown in Figures 2.14(a) is many millimeters long near the regions of high intensity. This good phase matching stems primarily from a fortuitous cancelation between the phase due to the linear index and the Gouy shift. (The index for the fundamental in 80 torr helium is $1 + 3.8 \times 10^{-6}$, whereas it is $1 - 2.7 \times 10^{-7}$ for the 75th harmonic [60].) The aperture has the effect of linearizing the Gouy shift with axial position in the focus. This linearized Gouy shift, together with the phase error arising from a limited amount of plasma, tends to

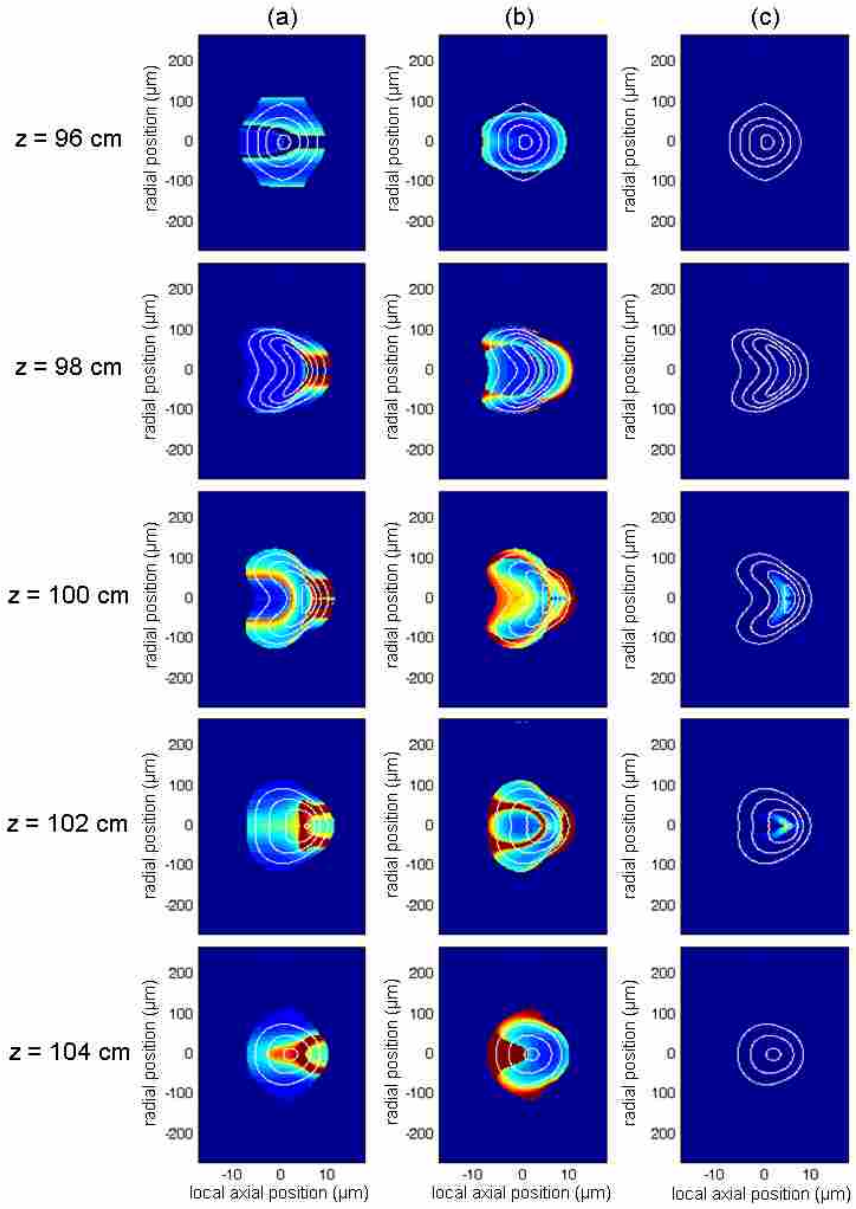

Figure 2.14 Coherence lengths of the 75th harmonic for each point on the pulse for (a) conventional and (b) intrinsic intensity-dependent phase. Coherence lengths have been capped at a reabsorption limit of 2 cm (dark red). (c) The fifth power of the laser intensity multiplied by the square of the coherence length (including both conventional and intrinsic phases) at each point on the pulse. The white contour lines indicate laser intensity. The dark red color in (c) indicates strong harmonic generation in arbitrary units.

cancel with the linear dispersion of the neutral gas. In the case of decreasing intensity with z, the intrinsic phase mismatch shown in Figure 2.14(b) introduces a phase slip with the same sign as that arising from the neutral gas.

The energy of harmonic emission depends nonlinearly on the laser intensity, which we approximate with a fifth-order power law [77] (although a third-order power law, for example, gives qualitatively similar results). Efficient high-harmonic generation requires both high-intensity and good phase matching. Figure 2.14(c) shows the fifth power of the laser intensity multiplied by the square of the coherence length, computed with the combined conventional and intrinsic phases (not shown). In each frame, one can see the portions of the pulse that contribute to overall harmonic emission, assuming the harmonics exit into vacuum following the frame and continue on to a detector (as was done in the experiment described in the previous section by scanning the exit foil to different axial positions). The best overall phase matching occurs near z =101 cm, where the separate phase mismatches indicated in Figures 2.14(a) and (b) have similar magnitudes and opposite signs. Near the front of the pulse, the coherence length exceeds the reabsorption limit of 2 cm, in agreement with earlier direct experimental observations [32]. On the other hand, as plasma is generated on the rear of the pulse, that portion of the pulse experiences poor phase matching. By integrating each snapshot in Figure 2.14(c) radially and longitudinally, the total harmonic energy emerging from each longitudinal step can be calculated. Figure 2.15(a) shows the calculated overall emission for the 75th harmonic at each longitudinal step. Our experimental results for the same harmonic are also shown for comparison (also shown in Figure 2.9(a)). We find that the vast majority of the harmonic output comes from the forward part of the pulse, before significant ionization. The result is hardly affected if we exclude regions wherein ionization exceeds 10% of the peak amount.

We have observed experimentally that opening the aperture located before the

focusing lens decreased the harmonic output by about an order of magnitude [65]. Our simulation also shows this dramatic behavior, which is plotted in Figure 2.15(a). Since the simulation uses a smooth input beam, the aperture effect does not arise merely from spatially cleaning the laser beam. Rather, it is due primarily to linearizing the rate of the Gouy phase slip in the apertured case, as seen in Figure 2.15(b). This is consistent with the analysis by Kazamias et al. [69] on the aperture effect.

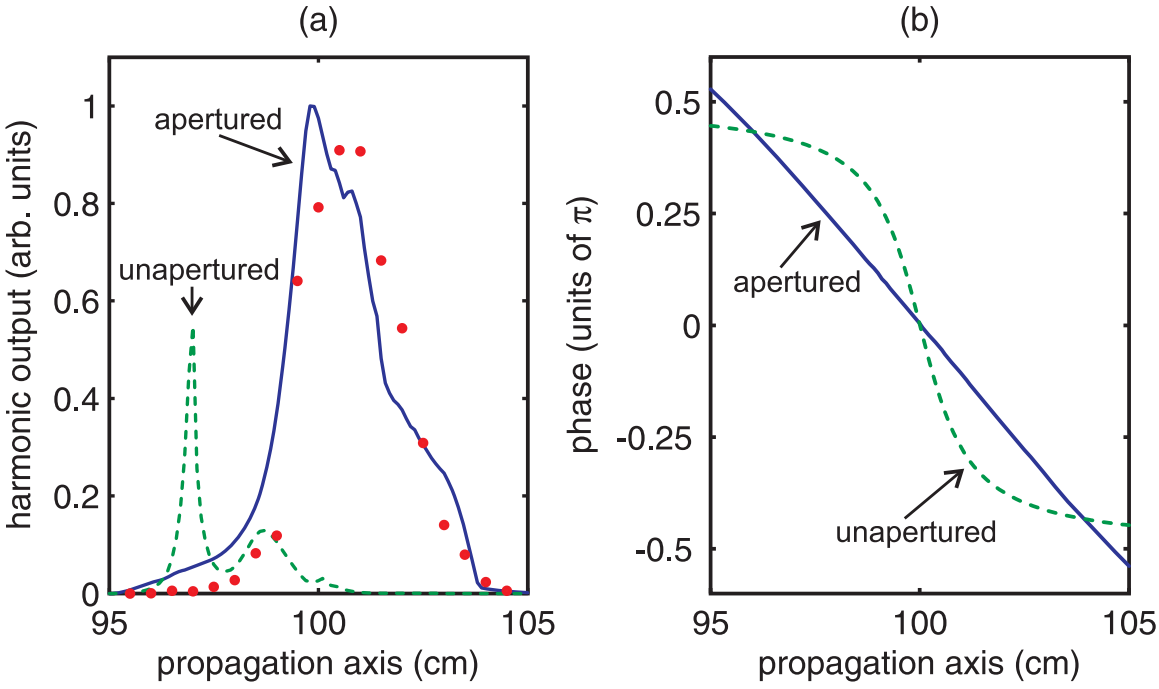

Figure 2.15 (a) The calculated (solid line) and measured (dots) overall emission for the 75th harmonic with an aperture in the beam. Also plotted is calculated overall emission for the same harmonic with an unapertured pulse (dashed line). (b) Beam phase due to the Gouy shift for an apertured (solid line) and an unapertured (dashed line) beam.

2.7 Conclusion

Simulations demonstrate that the interplay between the focusing geometry of the apertured beam combined with refraction from plasma generation is responsible for

the double focus observed in our experiments. Kerr-style self-focusing does not appear to play a role. The agreement between the simulations and the various experimental measurements lends credibility to using the simulations to assess phase-matching of high-order harmonics. The simulations suggest that the high harmonics produced in our helium-filled cell come almost entirely from the forward, undistorted portion of the laser pulse. Harmonics are suppressed in the rear portion of the pulse that undergoes significant ionization. Thus, the self-guiding of the pulse and the occurrence of the second focus in fluence are only incidental in the sense that they arise from a part of the pulse that does not contribute to the high-harmonic output. The good phase matching we have observed experimentally arises in large part from the balancing of the linear index against the Gouy shift, which varies almost linearly in z when an aperture is partially closed on the pre-focused beam. The intrinsic phase mismatch and that arising from a modest amount of plasma also participate in minimizing the phase mismatch. These findings have allowed us to use the semi-infinite gas cell along with the aperture effect to maximize harmonic output. This has enabled us to reach the kind of high harmonic signals we need for polarimetry measurements described in subsequent chapters.

Chapter 3

Description of Extreme Ultraviolet Polarimeter and Procedures

In this chapter we detail the development of a polarimeter instrument for EUV reflection measurements, including the positioning system, spectral resolution, and source stability. Our instrument has a wavelength range from 10 nm to 42 nm. We have found that we can make measurements of reflectances as low as 0.001 with a spectral resolution ($\lambda/\Delta\lambda$) of about 180.

3.1 Positioning and Detection Systems

The major components of the polarimeter are the sample, the grating, and the microchannel-plate (MCP) detector. The positioning system is made up of four rotation stages and two linear translation stages controlled by a single computer, as illustrated in Figures 3.1 and 3.2. The sample or test surface is mounted above two concentric rotation stages (ThorLabs NanoRotator NR360S). One stage varies the incident angle of the harmonic light on the sample. This provides measurements of

sample reflectance as a function of incident angle. The other stage swings the entire detection system (grating and MCP detector) through twice that angle, allowing detection of reflected light. A second pair of rotation stages sits beneath the grating at a distance of 15 cm from the sample. One of these rotation stages adjusts the grating angle, and the other separately adjusts the angle of the MCP to allow detection of diffracted light. A linear translation stage is used beneath the MCP detector to focus the harmonic orders of interest onto the detector. A typical grating angle is 4°, and a typical distance from the grating to the MCP is 30 cm. The sample holder is also connected to a linear translation stage. This allows the sample to be moved out of the beam to obtain incident-intensity measurements of harmonics.

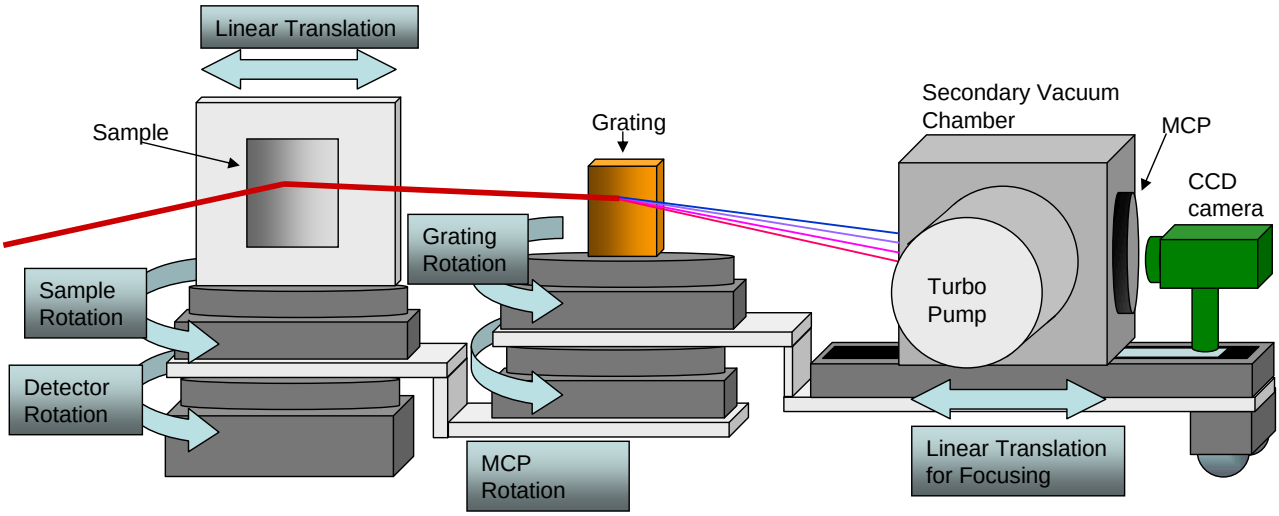

Figure 3.1 Polarimeter positioning system (side view). Incident harmonics are reflected from a sample that can be rotated to measure reflectance as a function of angle. A second rotation stage beneath the sample rotates the entire detection system through twice the sample angle. The EUV grating can also be rotated to measure different wavelength ranges of harmonics. A second rotation stage under the grating rotates the detector.

The diffraction grating is placed after the sample, which allows simultaneous reflectance measurements of a range of wavelengths. The different harmonic orders are spatially separated on the MCP and recorded with a charge coupled device (CCD)

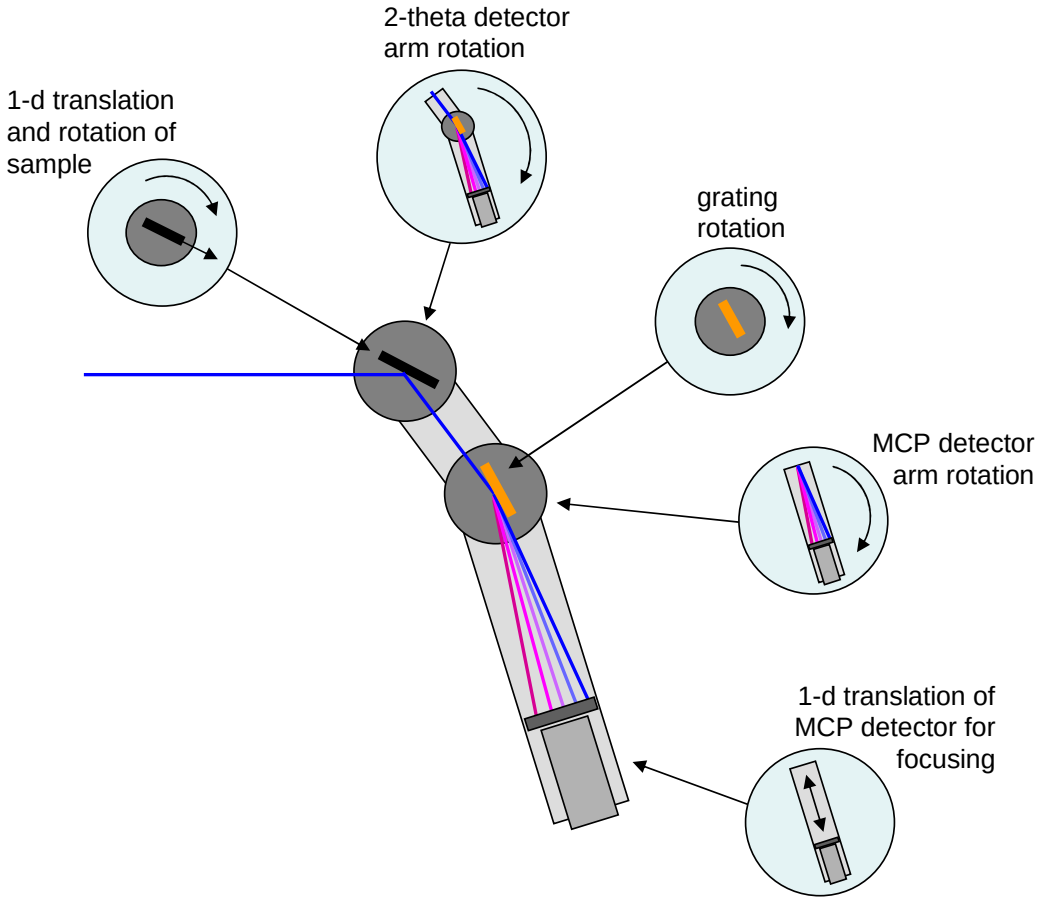

Figure 3.2 Polarimeter positioning system (top view)

camera. We can measure the reflectance for 10—20 consecutive odd harmonic orders simultaneously. The polarimeter positioning system is housed in a vacuum chamber with approximate dimensions 1.5×1 m^2, which is evacuated to about 10^{-4} torr. The MCP detector must be operated at pressures lower than 10^{-5} torr so we placed a small vacuum chamber (Lesker CU60450) inside the large vacuum chamber. This secondary vacuum chamber has its own turbo pump and a 5 mm aperture for the harmonics to enter. With differential pumping, this secondary chamber can reach base pressures lower than 10^{-6} torr. The entire system can pump to the necessary pressures in under 30 min from startup.

The detector consists of a stacked microchannel plate pair coupled to a phosphor screen. The front plate is connected to ground and the back plate is held at 1100-1600 V. The phosphor screen is powered with 5200 V. A visible light CCD camera captures the image on the phosphor screen and is read by a computer.

To determine the wavelength of each harmonic, we placed a 0.2 μm thick aluminum filter on a solenoid so that it could be moved into and out of the harmonic beam before the sample while under vacuum. The aluminum $L_{2,3}$ edge transmits harmonics of order 47 and below, but not harmonic orders 49 and above. By moving the filter into the beam while observing harmonics, we can quickly identify the 47th order. From there we simply count orders to calibrate the rest of the harmonic spectrum. A lineout of harmonics with and without the aluminum filter inserted are plotted in Figure 3.3.

Photographs of the positioning setup are shown in Figures 3.4 and 3.5.

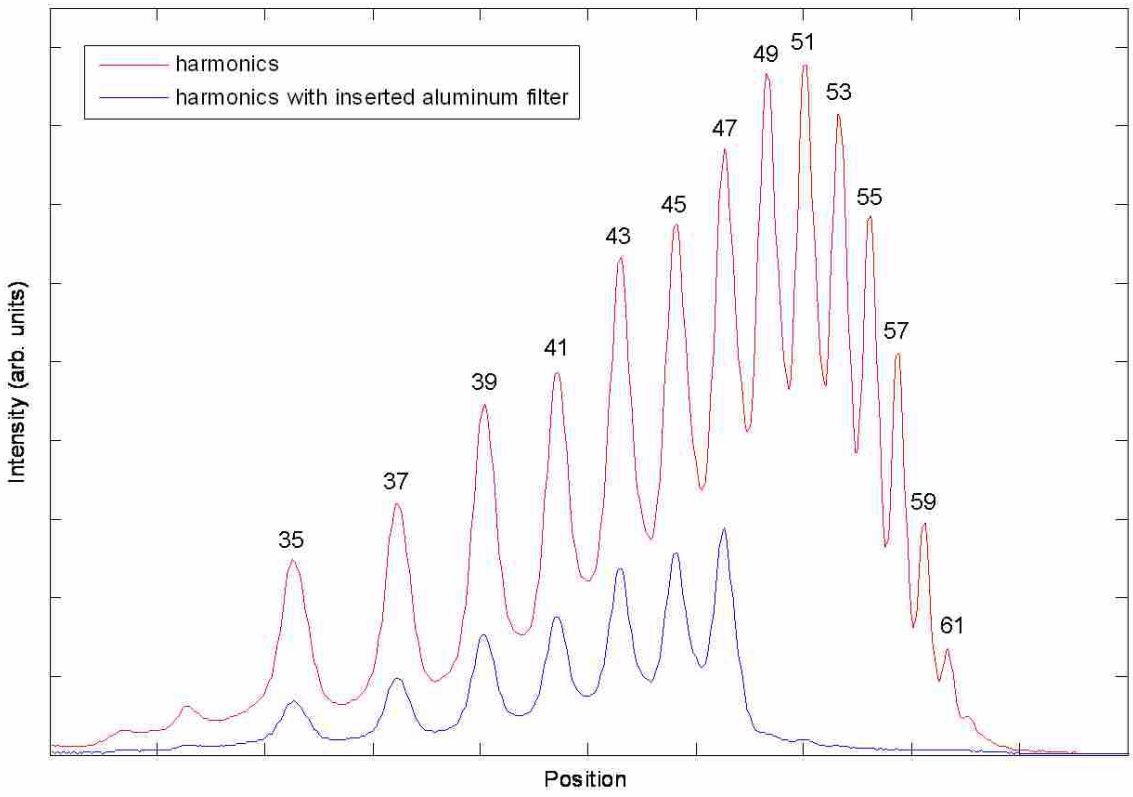

Figure 3.3 Harmonics measured with and without inserted aluminum filter.

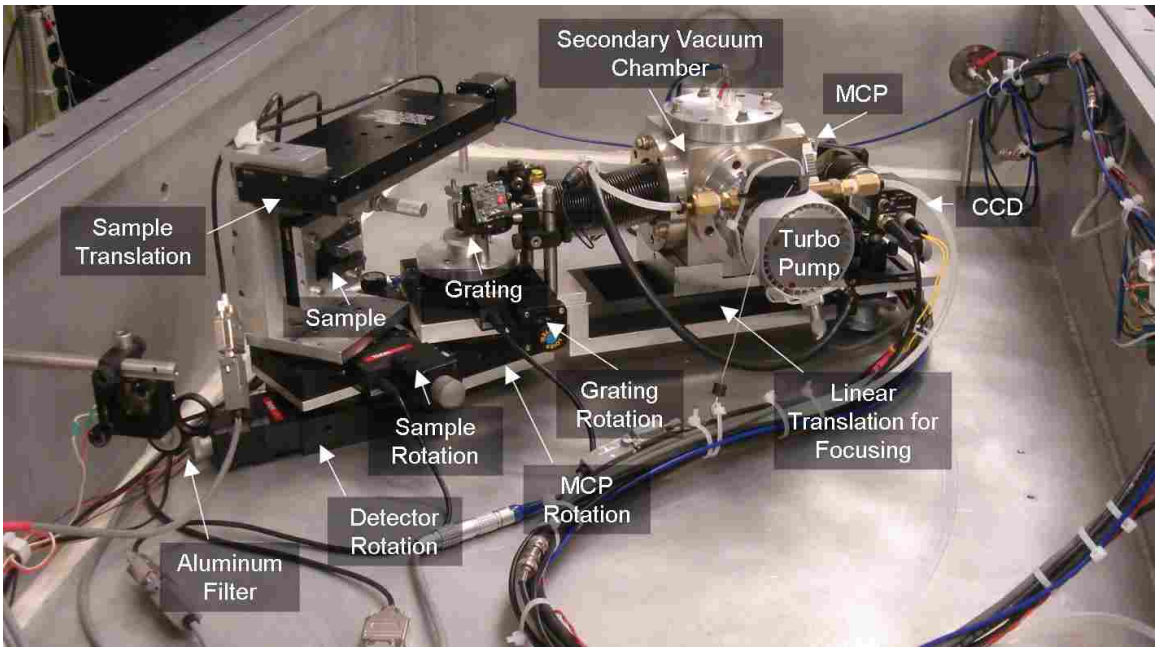

Figure 3.4 Photograph of polarimeter positioning system (side view).

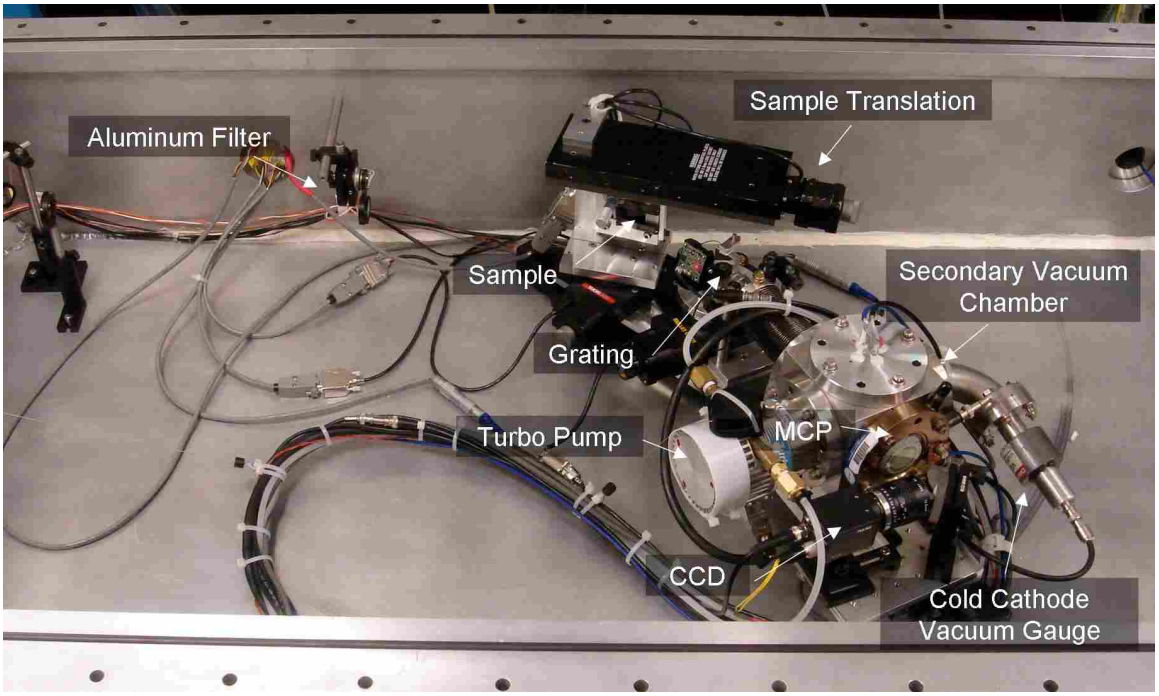

Figure 3.5 Photograph of polarimeter positioning system (top view).

3.2 Alignment Diagnostic

The secondary vacuum chamber (15 kg) and the turbo pump (3 kg) are major contributors to weight on the long (∼45 cm) rotating arm. We use ball-bearing wheels under the secondary vacuum chamber to carry the weight of the assembly. However, owing to the weight of the positioning stages and the secondary vacuum chamber, the torque limit of 23 N·cm is seriously exceeded on two of the rotation stages. As a result, the positioning error compounds to as poor as 1°, which is clearly unacceptable. For example, to repeatedly position a given harmonic order within 1 mm on the detector, the first rotation stage must have positioning accuracy of 0.1°, and the second 0.2°. (Recall that the sample-to- grating distance is approximately 15 cm while grating-to-MCP distance is approximately 30 cm.)

To address this issue, we implemented an alignment diagnostic that employs a tightly collimated HeNe 633 nm laser (refer to Figure 3.6). The laser enters the large vacuum chamber through a lens in a side port. A solenoid toggles a temporary mirror into position at any time during a measurement run, allowing the HeNe laser to propagate along the same path as the harmonics into the spectrometer. The HeNe laser has a ∼1 mm spot size on the diffraction grating. A CCD camera views the HeNe laser spot on the diffraction grating surface. A second CCD positioned inside the secondary vacuum chamber observes where the zero-order reflection from the grating strikes the MCP surface.

After initial positioning of the rotation stages, fine adjustments can be made first to center the HeNe laser on the diffraction grating and second to cause the zero-order reflection of the HeNe beam to strike a predetermined location on the interior of the MCP. This procedure allows the first stage to be set with a positioning accuracy better than 0.1° and the second stage to better than 0.2°. We found that the positioning

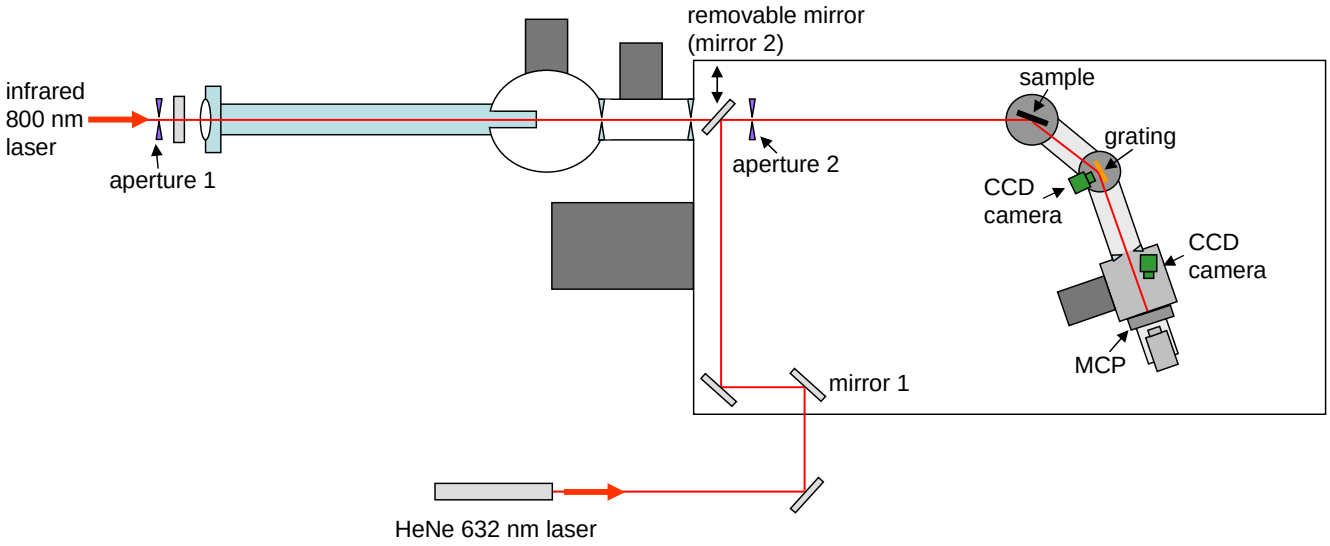

Figure 3.6 *In-situ* HeNe laser alignment system. A solenoid toggles a mirror into position while under vacuum, temporarily sending the HeNe laser along the same path as the harmonic-generating laser. A CCD camera views the HeNe laser spot on the grating and another CCD views the laser spot on the MCP surface, allowing alignment of rotation stages.

system was accurate enough for us to easily distinguish harmonic orders from each other. Because of the sharpness of some of the harmonic peaks, we are able to align the harmonic spectral images further using software, making the effective angle positioning accurate to about 0.01°. Using both of these techniques, we are able to obtain a spectral resolution $\lambda/\Delta\lambda$ of 180 (discussed in section 3.4).

The alignment procedure for the system is as follows (see Figure 3.7):

1. At low power, align the infrared laser with apertures 1 and 2.
2. Move the sample to 90 degrees and adjust the sample angle until it retro-reflects the laser beam back through the apertures. A HeNe laser can also be used temporarily in place of the infrared laser system.
3. Turn on the solenoid that inserts the HeNe mirror (mirror 2) into the laser path. Align the HeNe laser along the same path as the infrared laser by aligning with aperture 2 with mirror 1 and adjusting mirror 2 until the HeNe laser beam retro-reflects from the sample.
4. Move the sample out of the laser path with the linear sample stage.

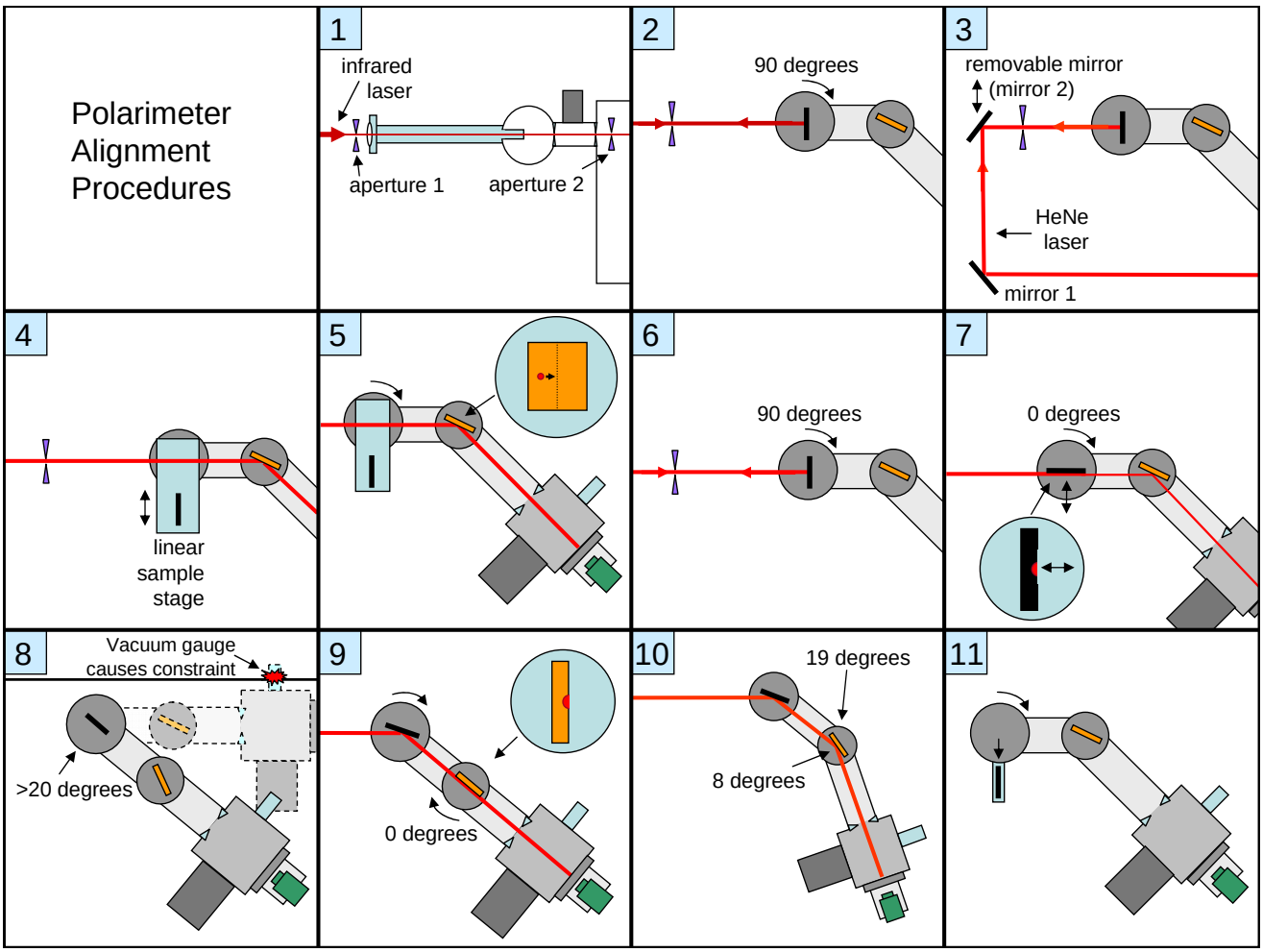

Figure 3.7 Depiction of steps for aligning the polarimeter.

5. To align the detector arm, adjust the detector angle until the HeNe laser is centered on the grating.

6. Move the sample back into the beam with the linear sample stage. Because the detector angle was adjusted in the previous step, the sample angle will now be slightly off (the sample motor is on top of the detector motor, so moving the detector motor also moves the sample). Adjust the sample angle again so that it is retro-reflecting the HeNe laser. This angle is defined as the sample 90-degree position.

7. Move the sample angle to 0 degrees. Align the sample z-position by adjusting the micrometer on the sample stage until the sample is cutting off half of the HeNe beam.

8. The vacuum gauge on the secondary vacuum chamber causes a physical constraint such that the MCP arm cannot be moved to 0 degrees at the same time that the detector arm is moved to 0 degrees. To align the MCP arm, move the detector angle to any angle greater than 10 degrees. Move the MCP arm angle to 0 degrees and adjust until the legs line up.

9. To align the grating angle, move the sample angle to half of what the detector angle is. This reflects the HeNe laser onto the grating. Move the grating angle to 0 degrees and adjust this angle until the grating is cutting off half of the HeNe beam.

10. The grating and MCP arm angles are now both at 0 degrees. To see harmonics, the grating should be moved to approximately 8 degrees and the MCP arm should be moved to approximately 19 degrees. These angles can be adjusted while viewing harmonics to view desired harmonic orders.

11. To prepare the positioning system for an incident intensity measurement, which is usually the first step in a reflectance scan, move the detector angle to 0 degrees, the sample angle to 90 degrees, and move the sample out of the beam with the linear sample stage.

3.3 Controlled harmonic attenuation

In the EUV, most materials are not highly reflecting except near grazing incidence. For this reason, a measurement of reflectance as a function of grazing-incidence angle made through a significant range of angles can span three or four orders of magnitude. Our MCP/camera system does not have sufficient dynamic range to span this

variation. We successfully increased the dynamic range of our detection system with a secondary gas cell that acts as a controlled harmonic attenuator.

Previous to using this attenuator, we increased the dynamic range of the detection system by increasing the voltage on the second plate of the microchannel plate detector [78]. This process is naturally nonlinear. We attempted to characterize this nonlinearity. However, the performance of the MCP is different for each wavelength of light; it could change as the plates age; and it could be different for different physical locations on the plates. When making reflectance measurements of silicon dioxide, a known sample, we found that these measurements did not agree well with calculated curves, especially far from grazing where the signal was low. We attributed this mismatch with our inability to accurately describe the performance of the detector as the voltage was increased. We thus implemented the secondary gas cell to eliminate the need to change the plate voltage as the signal decreased.

The secondary gas cell is 14 cm long, and is placed in the path of the laser after harmonics are generated, about 30 cm downstream from the laser focus so that the laser cannot ionize the gas or generate additional harmonics (see Figure 1.9). Neon gas can be added to the cell (usually between 0 and 3 torr measured with a manometer), which attenuates harmonics up to three orders of magnitude. The principle of the controlled harmonic attenuator is depicted schematically in Figure 3.8. At grazing incidence where signal is high, gas is added to decrease the signal, while at near-normal angles, no gas is added. Thus high and low signal can be measured with similar exposure to the detector. The actual signal level is later obtained using the absorption coefficient of neon, which is well characterized [60].

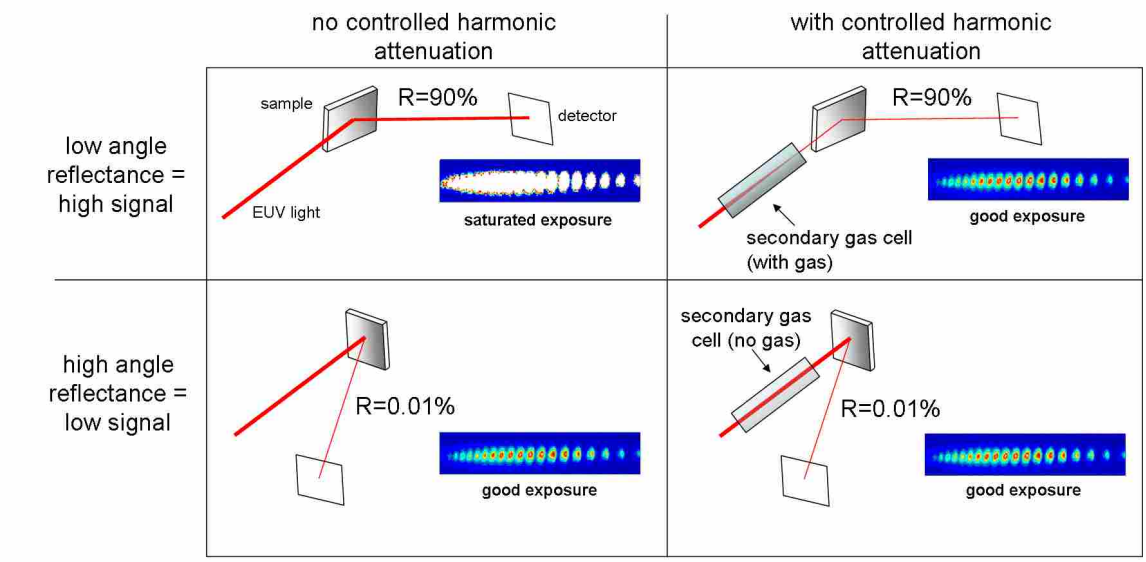

Figure 3.8 Schematic of the principle of controlled harmonic attenuation. Without the secondary gas cell, reflectance at low angles will saturate the detector if the detector voltage is sufficiently high to detect reflectance at high angles. With the secondary gas cell, neon gas is added to attenuate harmonics at grazing incidence when signal is high, so that they can be detected on the same detector settings as reflected harmonics at near-normal incidence. Actual signal levels are later recovered using the absorption coefficient of neon.

3.4 Spectral Resolution

The harmonic source itself serves effectively as the entrance slit of the polarimeter/spectrometer. We developed a simple ray-tracing program to characterize the defocusing of the harmonics at the detector due to the finite size of the source and aberrations from the geometry of the spherical grating surface. We traced representative rays from a 100 μm extended light source to the grating situated 1.5 m away oriented 4° from grazing, and then to the MCP surface an additional 30 cm afterward (see Figure 3.9). The grating has 1200 lines/mm with a 2 m radius of curvature. The location of the focusing (or image distance) is given by

$$\frac{\sin^2\theta_1}{d_o} + \frac{\sin^2\theta_2}{d_i} = \frac{\sin\theta_1 + \sin\theta_2}{R} \tag{3.1}$$

where θ_1 is the incident angle of the light on the grating measured from grazing, θ_2 is the diffracted angle of the light measured from grazing, d_o is the object distance, d_i is the image distance, and R is the radius of curvature of the focusing diffraction grating [79, 80]. The simulation agrees with Eq. 3.1, giving a focusing location of about 33 cm for the 45th harmonic.

For typical harmonic beams with 3 mrad divergence arising from a 100 μm source, the maximum spread at the detector is 150 μm (rather than an ideal line), whereas the typical separation between harmonic lines is approximately 1 mm. The finite width of harmonic lines is partly due to the fact that we observe multiple wavelengths on a single plane, whereas different harmonics focus best with different grating-MCP spacings. Since harmonic features can be lined up effectively to within 30 μm using software, aberrations in the grating imaging system are the limiting factor in the spectral resolution.

As can be seen in Figure 3.10, harmonic peaks appear to sit on top of a quasi-continuous spectrum. The previous analysis suggests that the apparent continuous

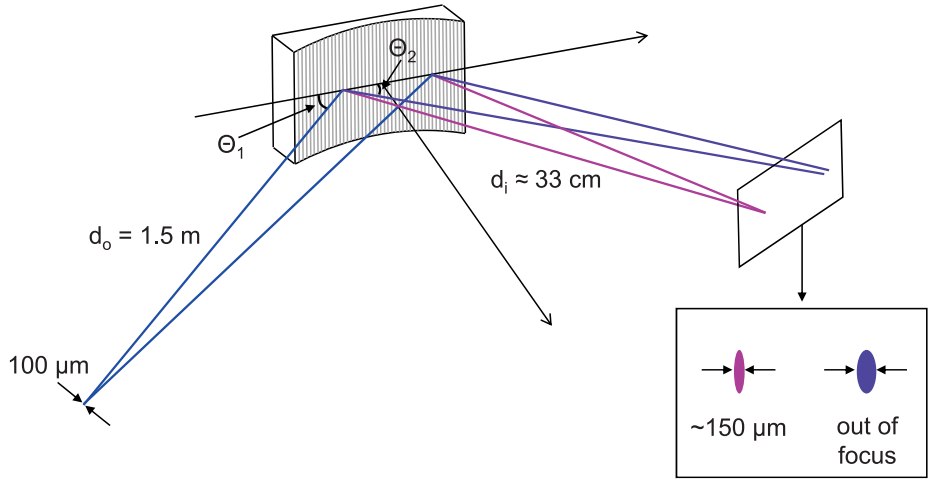

Figure 3.9 Schematic of setup for ray-tracing program to determine spectral resolution. Representative rays are traced from a 100 μm extended light source to the grating, situated 1.5 m away and oriented 4° from grazing and then to the MCP surface an additional 30 cm afterward.

spectrum does not arise merely from aberrations in the imaging system. The sharpness of the harmonic peaks within the image provide direct evidence of good spectral resolution. There may be multiple regimes of harmonic-generation within the generating volume, some regions giving rise to sharp orders, and others contributing shifted or broadened peaks of EUV wavelengths due to chirping of the generating pulse [81] or selfsteepening of the leading edge of the pulse [82]. The harmonics from these various regions can merge together to give broader spectral coverage.

As indicated in Figure 3.10, the 39th and 53rd harmonics are separated by 8.8 mm on the detector. This represents a change of 5.4 nm in wavelength. The blurring of the peaks by 150 μm (due to aberrations) corresponds to a change in wavelength of 0.092 nm, which corresponds to a spectral resolution ($\lambda/\Delta\lambda$) of about 180 for the 47th harmonic (λ=17.0 nm).

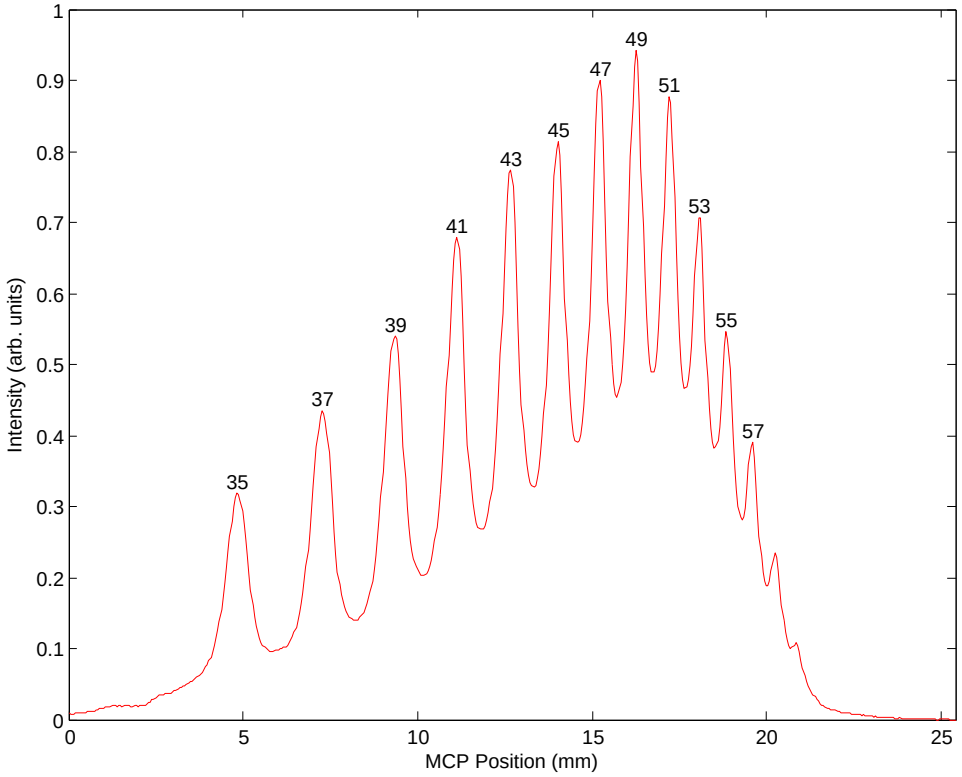

Figure 3.10 Harmonic signal as a function of position on the MCP detector. Harmonics orders from 35 to 61 were generated in neon gas. The sharpness of the harmonic peaks confirms that non-zero signal between harmonics is not due to defocusing.

3.5 Source Stability

The stability of our high harmonic source is very important in performing accurate polarimetry measurements. Reflectance measurements are defined as reflected signal divided by incident signal. Accordingly, variation in incident signal will affect the accuracy and repeatability of reflectance measurements. There are many factors to consider when determining the stability of the high harmonic source. For example, one of the main causes in variation of harmonic signal is that small variations in pump laser energy translate to large variations in harmonic output because of strong nonlinearity. Also, gas pressure variations, optic damage over time, and laser energy drift may affect the harmonic output over the course of a run. Short term stability in high harmonics, in other words stability from laser shot to laser shot, can vary by as much as 37%, as seen in Figure 3.11.

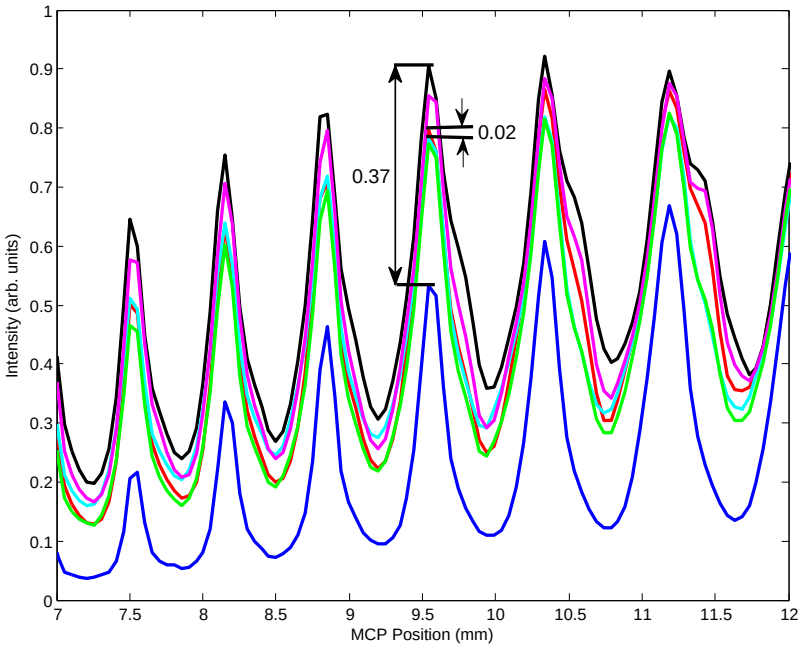

Figure 3.11 Lineout of harmonics from successive shots. This plot shows the short term, or shot to shot, stability of high harmonic source. The intensity of a single harmonic varies by as much as 37% and as little as 2%.

To improve stability of our EUV source, we average 100 shots (10 seconds) for each data file taken. The variation of harmonics averaged over 100 shots is, as seen in Figure 3.12, on the order of 7%.

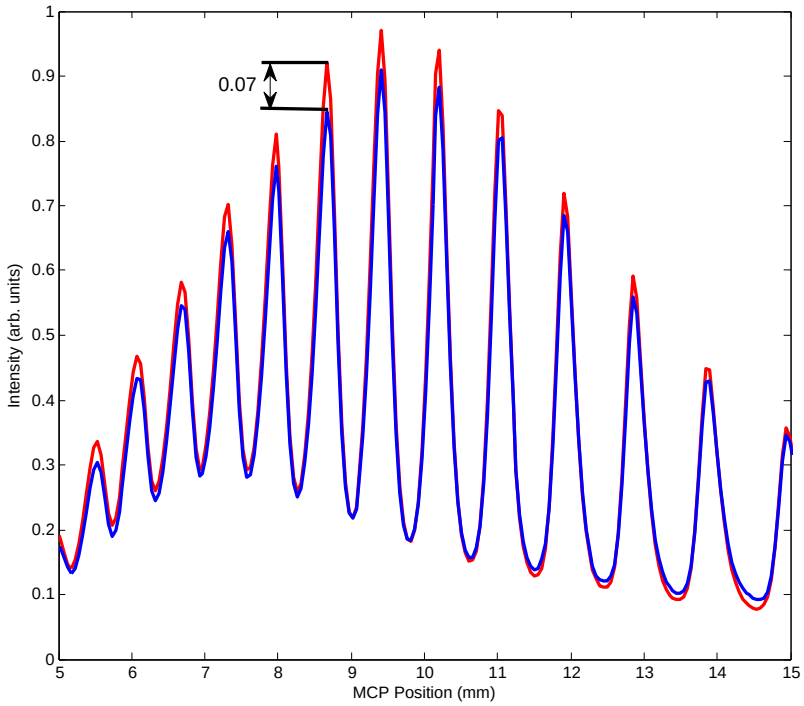

Figure 3.12 Lineouts of two measurements of harmonics averaged over 100 shots (10 seconds). Variation is on the order of 7%.

To further improve repeatability, we implemented a laser-pulse energy discriminator. An optical fiber transmits a small sample of the incident laser beam to an unused corner on the outside surface of the MCP detector. The light from the fiber is thus captured in the same image that records the harmonic spectra, providing real-time monitoring of the laser power. An example image of harmonics and the beam transmitted by the fiber is shown in Figure 3.13 (the white box outlines the beam transmitted by the fiber). In real time, our computer selects only shots where the incident laser energy falls within a user-specified range and averages 100 'acceptable' harmonic images. By decreasing the range of acceptable laser energy, the repeata-

bility of the measurements improves markedly. For our system, a ±10% laser-energy window selects about one image out of three and reduces the variability in harmonic signal significantly. Figure 3.14 shows two lineouts of harmonic spectra taken using a laser-energy window of ±10%. Variation is on the order of 0.4%.

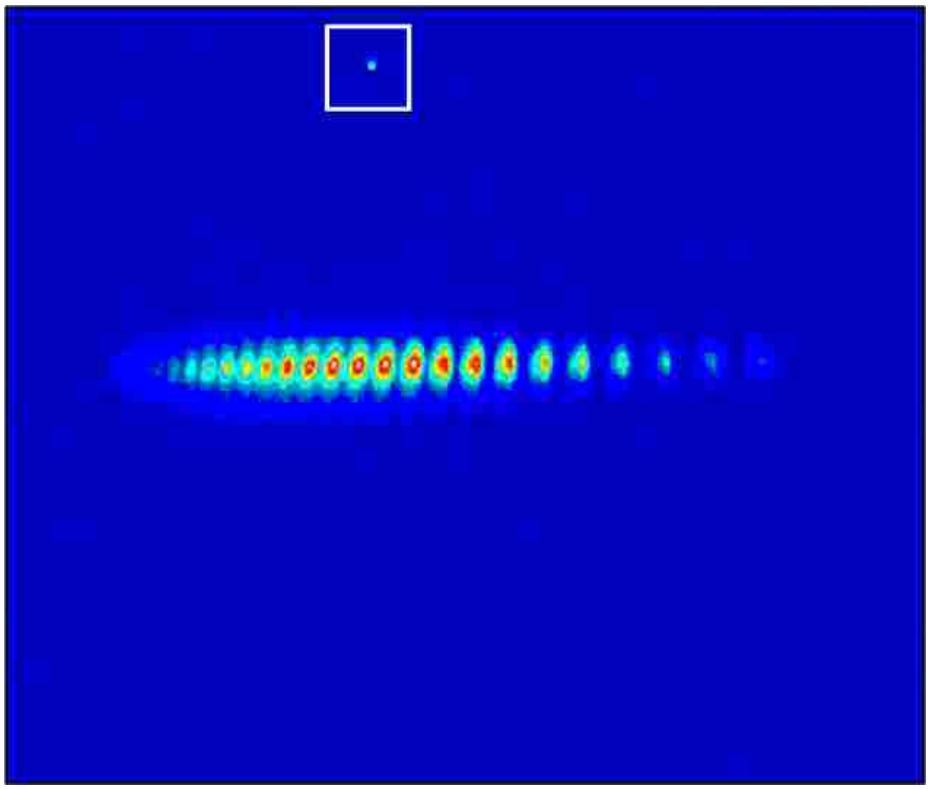

Figure 3.13 Image of harmonics at the detector. The white box outlines a small sample of the incident laser beam used for real-time laser energy discrimination.

Implementing this laser-power discriminator allowed us to increase the effective stability of our laser source to about 0.4%. However, laser-power variation is not the only systematic error we have in our system. For example, changes in the spatial profile of the gas in the region of harmonic generation (as happens when the laser continues to drill through the exit foil during a scan) or slight misalignments can cause error in our measurements. We demonstrate a technique to reduce the effects of these systematic errors on our measurements in chapter 5.

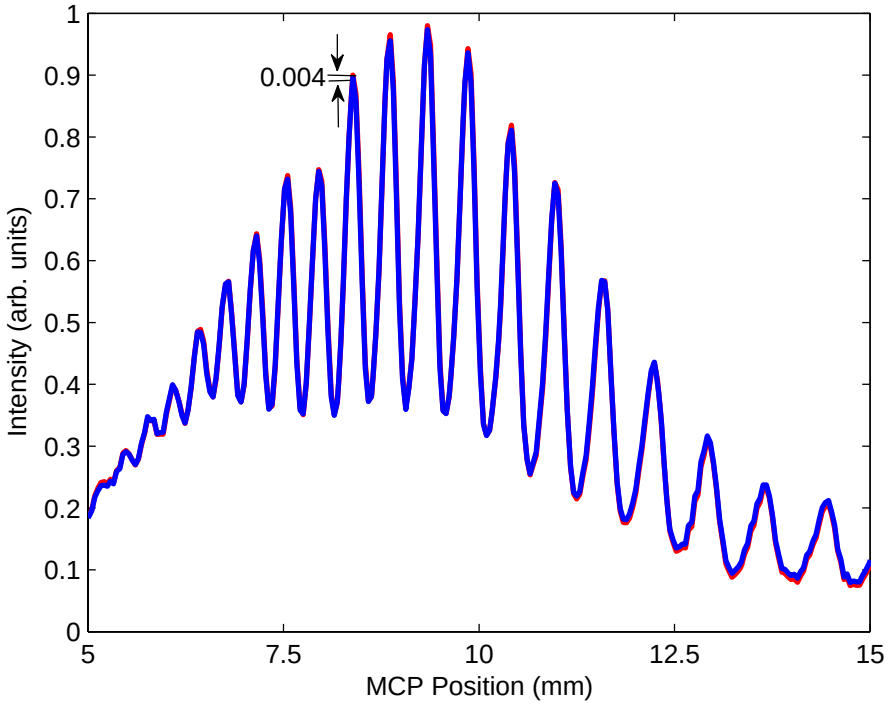

Figure 3.14 Lineout of two measurements of harmonics averaged over 100 'acceptable' images where the laser energy window is ±10%. Variation is on the order of 0.4%.

Chapter 4

Absolute Reflectance Measurements

In this chapter we discuss reflectance measurements of a silica sample used to benchmark the performance of the polarimeter. We describe the sample parameters, as well as the repeatability of the measurements. We outline the theoretical model, including the determination of optical constants, used to calculate reflectance curves for these measurements. We find good agreement between measured and expected results.

4.1 Sample

We used a silicon substrate with a thermally oxidized layer as a test sample to characterize our instrument. Spectroscopic ellipsometry showed the sample thickness to be 27.4 nm$\pm$0.2 nm. This sample is a good reference surface for characterizing the accuracy of the polarimeter, especially at wavelengths from 10 nm to 20 nm. This is because the thickness is such that interference in reflected light from the front and back surfaces of the silicon dioxide layer create fluctuations in reflection as the sample

angle is rotated. These fluctuations are commonly referred to as interference fringes, and they allow detailed comparisons of measured data with data calculated using the optical constants of silicon and silicon dioxide, which are well known [60]. Also, this sample exhibits interference fringes near Brewster's angle ($\sim$45°), which allows us to see significant differences in reflection at s- and p-polarizations. This makes the effect of polarization on reflectance more apparent. Silicon dioxide on silicon is also a good reference sample because it is stable in air for long periods of time, and the two surfaces of the oxide can be exceptionally smooth and uniform.

4.2 Reflectance Measurements and Repeatability

High harmonics for these measurements were produced in 12 torr of argon gas, 57 torr of neon gas, or 80 torr of helium gas. An aperture was placed immediately before the focusing lens at an optimal diameter of 1.1 cm. The exit foil of the gas cell was positioned 100 cm from the focusing lens. Reflectance measurements were taken at multiple wavelengths simultaneously. All measurements were averaged over 100 shots where the laser power was within $\pm$10%. Reflected signal was determined by making a lineout of the harmonics at each angle by averaging in the y-direction over the area shown in Figure 4.1. Harmonic orders were then determined using the method discussed in section 3.1. The maximum value of each harmonic was used for the reflected signal for that wavelength at each specific sample angle. Background noise (or 'dark current') was determined by averaging over an area on the MCP away from the harmonics (also shown in Figure 4.1). The advantage of measuring dark current in this way is that it is taken simultaneously with reflected signal. It thus takes into account angular dependence and any other unknown that may affect the dark current at different points in the run. The incident harmonic signal (before the sample) was

measured three different times during the run, at the beginning, middle, and end, to guard against possible drift in harmonic flux during the experiment. The variations between these measurements were on the order of the uncertainty in a given measurement. S- and p-polarizations were found to reflect from the EUV grating somewhat differently (see Figure 4.2), so each reflectance measurement was normalized using the incident measurement of the same polarization. The normalization algorithm followed the following format:

$$R = \frac{R_s - D_s}{I_s - D_s} \tag{4.1}$$

where R is the reflectance, R_s is the reflected signal, D_s is the dark signal, and I_s is the incident signal.

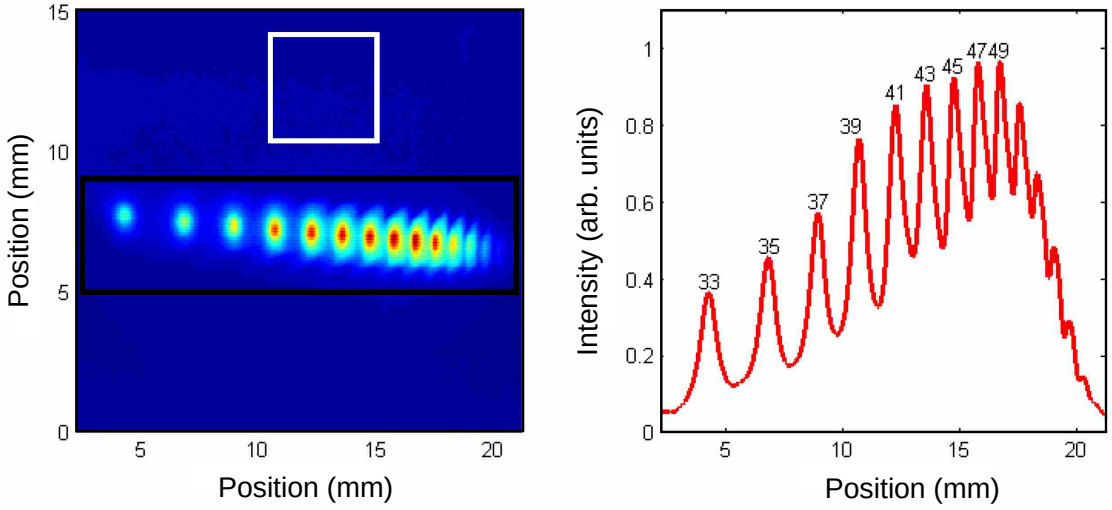

Figure 4.1 Harmonics (left) and lineout (right) at a sample angle of 10°. The black box in the left figure shows where harmonics are averaged in the y-direction to make the lineout. The white box in the left figure above the harmonics shows the area that is averaged to determine dark current.

Reflectance measurements were taken on three separate days in order to show repeatability. Figure 4.3 shows these three measurements of s-polarized reflectance at for four representative wavelengths, 15.7 nm, 15.1 nm, 14.5 nm and 14.0 nm, with

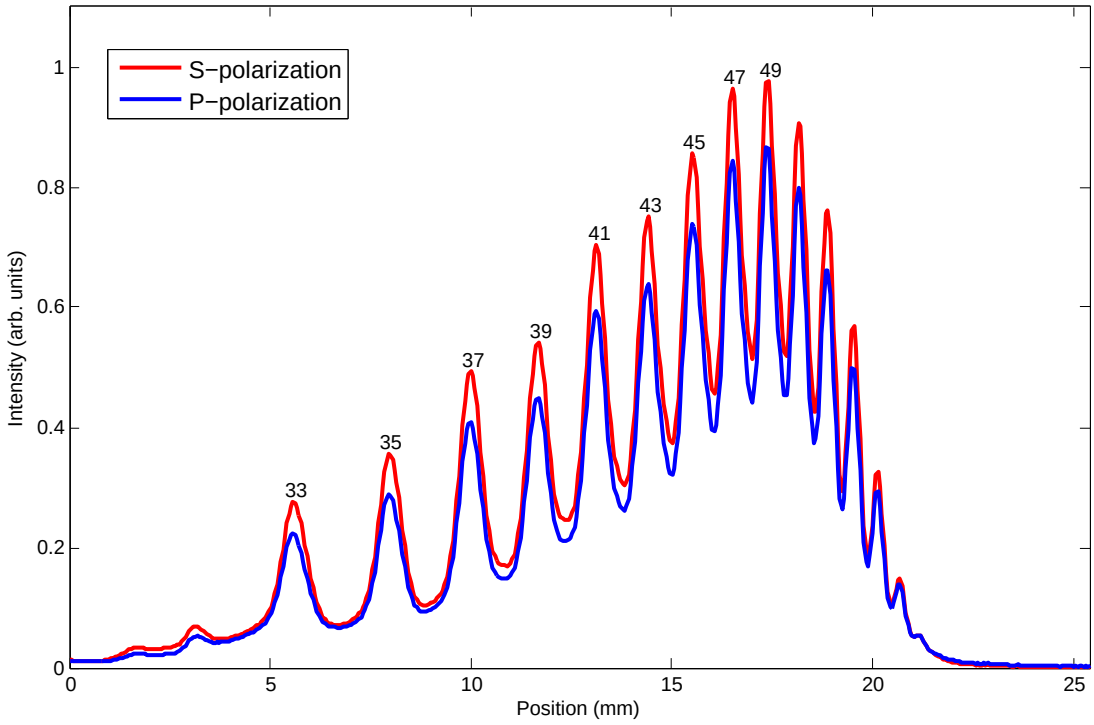

Figure 4.2 S- and p-polarized harmonics reflected slightly differently from the EUV grating. Accordingly, each reflectance measurement was normalized using the incident measurement of the same polarization.

fair repeatability.

4.3 Theoretical Model

To show the effectiveness of EUV polarimetry with high harmonics, we compare measured reflectance curves with calculated curves. In this section we describe the theoretical model used to calculate curves to compare with measured curves.

In many circumstances, it is necessary to consider more than one layer (see section 5.4), so we use a multilayer matrix theory. The layers consist of vacuum (region 0), multiple thin films (regions 1 through m), and a substrate (region $m+1$). The thickness of the jth layer is specified by d_j, and the complex index of refraction in each region is $N_j = n_j + i\kappa_j$. Light with wavelength λ is incident from region 0 onto region 1 with incidence angle θ_0, measured from grazing, and propagates in region 1 with angle θ_1 and in region j with angle θ_j, measured from grazing. The complex angles are determined in each region from Snells law: $N_0 \cos\theta_0 = N_j \cos\theta_j$. The reflectance from the multilayer stack is calculated using a standard matrix approach [13,14], which will be reviewed here.

At each interface, there is an incident wave, a reflected wave, and a transmitted wave. At the next interface, the transmitted wave from the previous layer becomes the new incident wave. The subscript r indicates waves traveling to the right (towards the substrate). These include incident and transmitted waves at each interface. The subscript l indicates waves traveling to the left (away from the substrate), i.e. reflected waves.

We review here the standard treatment for light reflected from a multilayer. At the first interface, the boundary conditions for the parallel components of the **E** and **B** fields for p-polarized light are

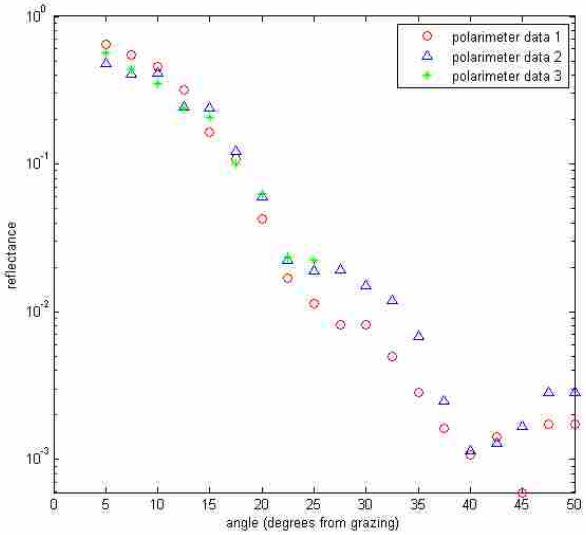

(a) q=51, λ=15.7 nm

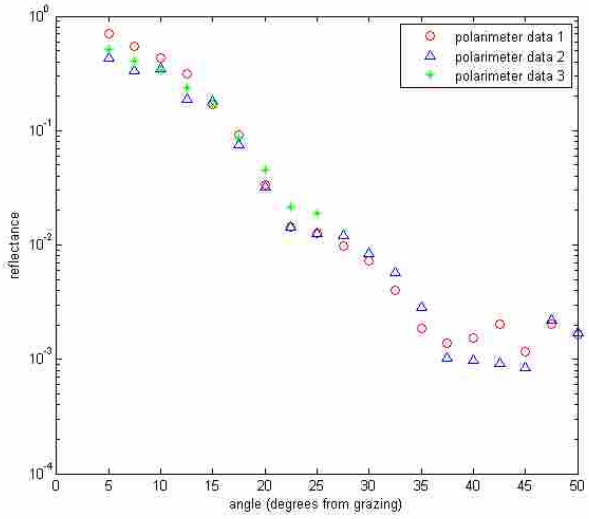

(b) q=53, λ=15.1 nm

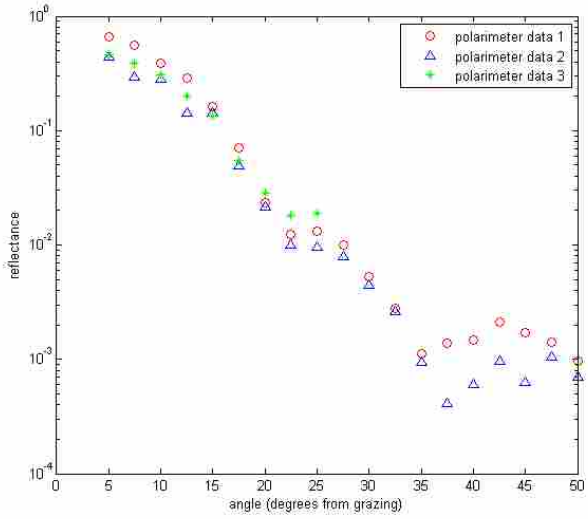

(c) q=55, λ=14.5 nm

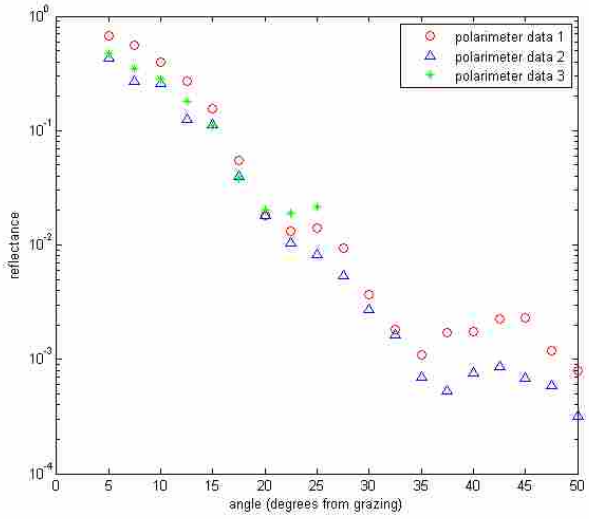

(d) q=57, λ=14.0 nm

Figure 4.3 Reflectance measurements made on three different days to show repeatability.

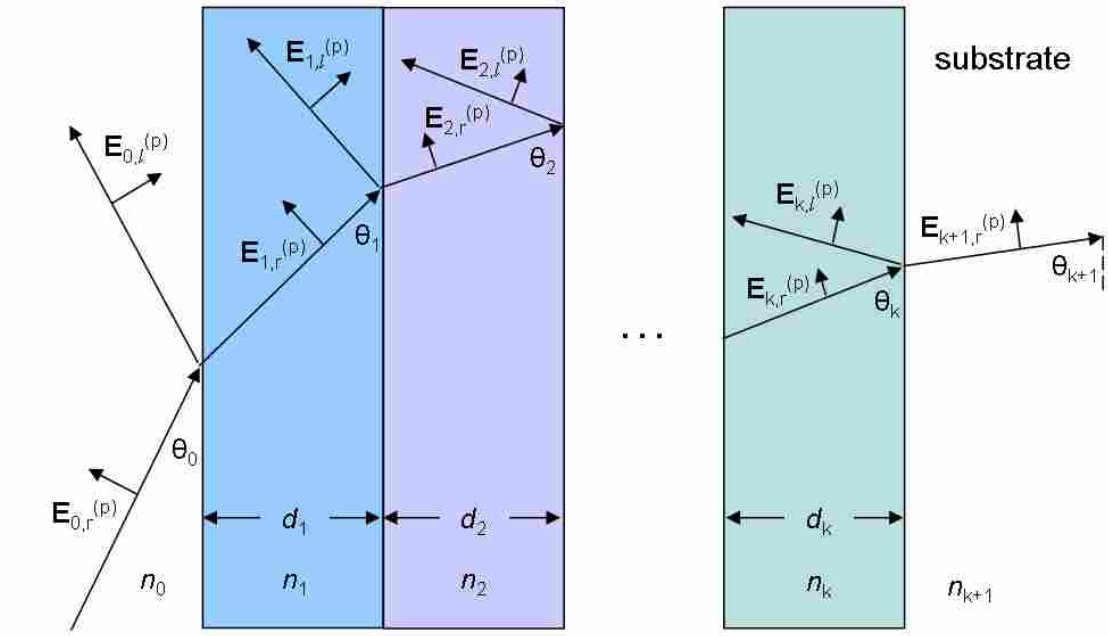

Figure 4.4 Schematic showing light propagation through multiple layers.

$$\sin\theta_0(E_{0,r}^{(p)} + E_{0,l}^{(p)}) = \sin\theta_1(E_{1,r}^{(p)} + E_{1,l}^{(p)}) \tag{4.2}$$

and

$$N_0(E_{0,r}^{(p)} - E_{0,l}^{(p)}) = N_1(E_{1,r}^{(p)} - E_{1,l}^{(p)}) \tag{4.3}$$

Similarly, at an arbitrary interface $j+1$ the boundary conditions for the parallel components of the **E** and **B** fields for p-polarized light are

$$\sin\theta_j(E_{j,r}^{(p)}e^{2\pi i N_j d_j \sin\theta_j/\lambda} + E_{j,l}^{(p)}e^{-2\pi i N_j d_j \sin\theta_j/\lambda}) = \sin\theta_{j+1}(E_{j+1,r}^{(p)} + E_{j+1,l}^{(p)}) \tag{4.4}$$

and

$$N_j(E_{j,r}^{(p)}e^{2\pi i N_j d_j \sin\theta_j/\lambda} - E_{j,l}^{(p)}e^{-2\pi i N_j d_j \sin\theta_j/\lambda}) = N_{j+1}(E_{j+1,r}^{(p)} - E_{j+1,l}^{(p)}) \tag{4.5}$$

Here we set the origin within each layer at the left surface. When making the connection with the subsequent layer at the right surface, we must explicitly take

into account the phase acquired by the field in propagating through the thickness d_j, as reflected in equations 4.4 and 4.5.

At the final interface, the boundary conditions can be written as

$$\sin\theta_m(E^{(p)}_{m,r}e^{2\pi i N_m d_m \sin\theta_m/\lambda} + E^{(p)}_{m,l}e^{-2\pi i N_m d_m \sin\theta_m/\lambda}) = \sin\theta_{m+1}E^{(p)}_{m+1,r} \tag{4.6}$$

and

$$N_m(E^{(p)}_{m,r}e^{2\pi i N_m d,\sin\theta_m/\lambda} - E^{(p)}_{m,l}e^{-2\pi i N_m d_m \sin\theta_m/\lambda}) = N_{m+1}E^{(p)}_{m+1,r} \tag{4.7}$$

The right side of the equation shows explicitly that there is no left-traveling wave in the substrate.

We can write Eqs. 4.4 and 4.5 as a single matrix equation, as follows.

$$\begin{bmatrix} \sin\theta_j e^{i\beta_j} & \sin\theta_j e^{-i\beta_j} \\ N_j e^{i\beta_j} & -N_j e^{-i\beta_j} \end{bmatrix} \begin{bmatrix} E^{(p)}_{j,r} \\ E^{(p)}_{j,l} \end{bmatrix} = \begin{bmatrix} \sin\theta_{j+1} & \sin\theta_{j+1} \\ N_{j+1} & -N_{j+1} \end{bmatrix} \begin{bmatrix} E^{(p)}_{j+1,r} \\ E^{(p)}_{j+1,l} \end{bmatrix} \tag{4.8}$$

where $\beta_j = 2\pi N_j d_j \sin\theta_j/\lambda$. Solving Eq. 4.8, we find

$$\begin{bmatrix} E^{(p)}_{j,r} \\ E^{(p)}_{j,l} \end{bmatrix} = \begin{bmatrix} \sin\theta_j e^{i\beta_j} & \sin\theta_j e^{-i\beta_j} \\ N_j e^{i\beta_j} & -N_j e^{-i\beta_j} \end{bmatrix}^{-1} \begin{bmatrix} \sin\theta_{j+1} & \sin\theta_{j+1} \\ N_{j+1} & -N_{j+1} \end{bmatrix} \begin{bmatrix} E^{(p)}_{j+1,r} \\ E^{(p)}_{j+1,l} \end{bmatrix} \tag{4.9}$$

We can now use Eq. 4.9 to connect the incident, reflected, and transmitted waves from the entire stack, as follows. If we write Eq. 4.9 for the $j = 0$ case, we find

$$\begin{bmatrix} E^{(p)}_{0,r} \\ E^{(p)}_{0,l} \end{bmatrix} = \begin{bmatrix} \sin\theta_0 & \sin\theta_0 \\ N_0 & -N_0 \end{bmatrix}^{-1} \begin{bmatrix} \sin\theta_1 & \sin\theta_1 \\ N_1 & -N_1 \end{bmatrix} \begin{bmatrix} E^{(p)}_{1,r} \\ E^{(p)}_{1,l} \end{bmatrix} \tag{4.10}$$

Substituting in for $\begin{bmatrix} E^{(p)}_{1,r} \\ E^{(p)}_{1,l} \end{bmatrix}$ by using Eq. 4.9 now for the $j = 1$ case, we find

$$\begin{bmatrix} E_{0,r}^{(p)} \\ E_{0,l}^{(p)} \end{bmatrix} = \begin{bmatrix} \sin\theta_0 & \sin\theta_0 \\ N_0 & -N_0 \end{bmatrix}^{-1} \begin{bmatrix} \sin\theta_1 & \sin\theta_1 \\ N_1 & -N_1 \end{bmatrix} \begin{bmatrix} \sin\theta_1 e^{i\beta_1} & \sin\theta_1 e^{-i\beta_1} \\ N_1 e^{i\beta_1} & -N_1 e^{-i\beta_1} \end{bmatrix}^{-1} \begin{bmatrix} E_{2,r}^{(p)} \\ E_{2,l}^{(p)} \end{bmatrix} \tag{4.11}$$

If we define a matrix $M_j^{(p)}$ to be

$$M_j^{(p)} = \begin{bmatrix} \sin\theta_j & \sin\theta_j \\ N_j & -N_j \end{bmatrix} \begin{bmatrix} \sin\theta_j e^{i\beta_j} & \sin\theta_j e^{-i\beta_j} \\ N_j e^{i\beta_j} & -N_j e^{-i\beta_j} \end{bmatrix}^{-1} \tag{4.12}$$

we can connect the fields in the initial and final layers, as follows

$$\begin{bmatrix} E_{0,r}^{(p)} \\ E_{0,l}^{(p)} \end{bmatrix} = \begin{bmatrix} \sin\theta_0 & \sin\theta_0 \\ N_0 & -N_0 \end{bmatrix}^{-1} \left(\prod_{j=1}^{m} M_j^p \right) \begin{bmatrix} \sin\theta_{m+1} & \sin\theta_{m+1} \\ N_{m+1} & -N_{m+1} \end{bmatrix} \begin{bmatrix} E_{m+1,r}^{(p)} \\ 0 \end{bmatrix} \tag{4.13}$$

Once these matrices are computed, we can find the reflectance and transmission of the multilayer stack using the following equations

$$T^{(p)} = \left| \frac{E_{m+1,r}^{(p)}}{E_{0,r}^{(p)}} \right|^2 \tag{4.14}$$

$$R^{(p)} = \left| \frac{E_{0,l}^{(p)}}{E_{0,r}^{(p)}} \right|^2 \tag{4.15}$$

Similarly, for s-polarized light we have the equations

$$T^{(s)} = \left| \frac{E_{m+1,r}^{(s)}}{E_{0,r}^{(s)}} \right|^2 \tag{4.16}$$

$$R^{(s)} = \left| \frac{E_{0,l}^{(s)}}{E_{0,r}^{(s)}} \right|^2 \tag{4.17}$$

where

$$\begin{bmatrix} E_{0,r}^{(s)} \\ E_{0,l}^{(s)} \end{bmatrix} = \begin{bmatrix} 1 & 1 \\ N_0\sin\theta_0 & -N_0\sin\theta_0 \end{bmatrix}^{-1} \left(\prod_{j=1}^{m} M_j^s \right) \begin{bmatrix} 1 & 1 \\ N_{m+1}\sin\theta_{m+1} & -N_{m+1}\sin\theta_{m+1} \end{bmatrix} \begin{bmatrix} E_{m+1,r}^{(p)} \\ 0 \end{bmatrix} \tag{4.18}$$

and

$$M_j^{(s)} = \begin{bmatrix} 1 & 1 \\ N_j\sin\theta_j & -N_j\sin\theta_j \end{bmatrix} \begin{bmatrix} e^{i\beta_j} & e^{-i\beta_j} \\ N_j\sin\theta_j e^{i\beta_j} & -N_j\sin\theta_j e^{-i\beta_j} \end{bmatrix}^{-1} \tag{4.19}$$

4.4 Comparison with Calculated Reflectance Curves

Figure 4.5 shows reflectance measurements for s- and p-polarizations for four representative wavelengths: 29.6 nm, 20.5 nm, 15.7 nm, 14.0 nm compared with reflectance curves calculated using the optical constants of silicon and silicon dioxide [60], which are well known. Also plotted are reflectance measurements from the same sample taken at the Advanced Light Source synchrotron (Beamline 6.3.2).

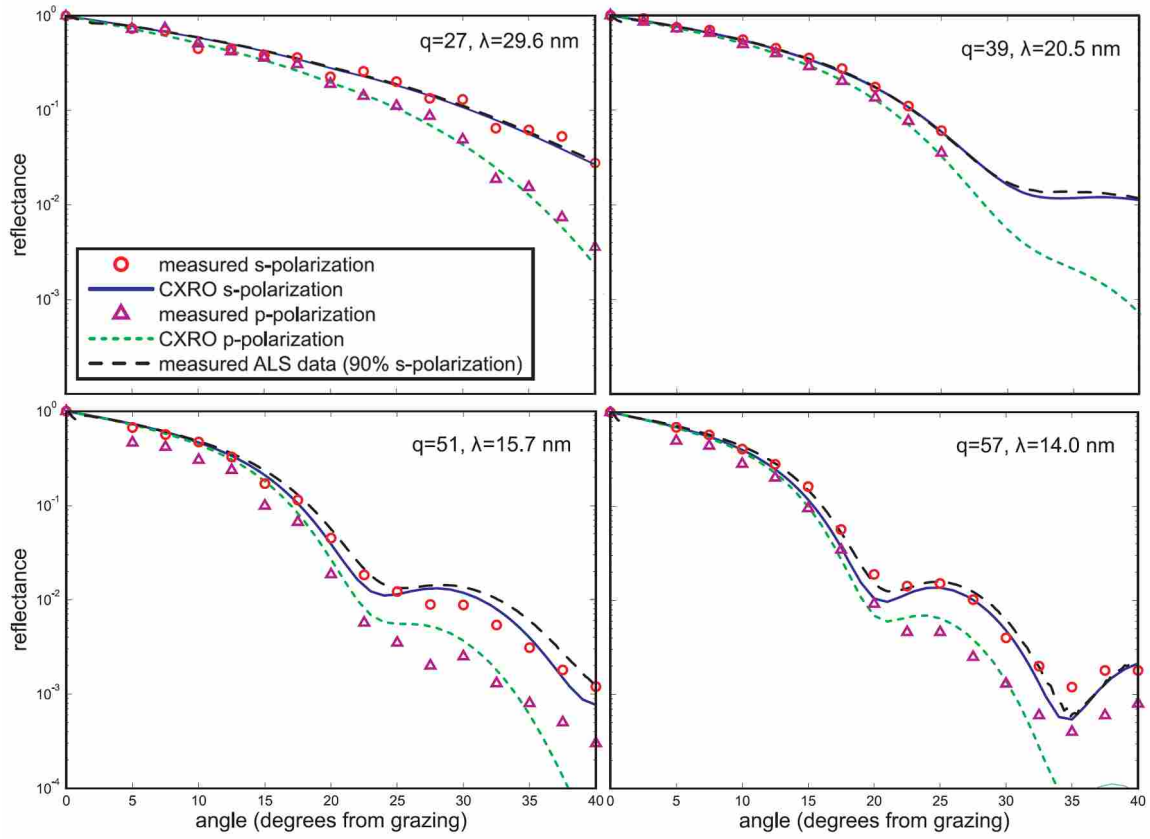

Figure 4.5 Comparison of reflectance measurements made with BYU polarimeter and those calculated using the optical constants of silicon and silicon dioxide. Also plotted are reflectance measurements from the same sample taken at the Advanced Light Source synchrotron (Beamline 6.3.2).

The measured data agrees reasonably well with calculated values. Also, interference fringes in both data sets match well. Figure 4.6 shows the measured and

computed reflectance as a function of wavelength at a sample angle of 17.5° from grazing. The results show reasonably good agreement, although the data points show noticeable fluctuation.

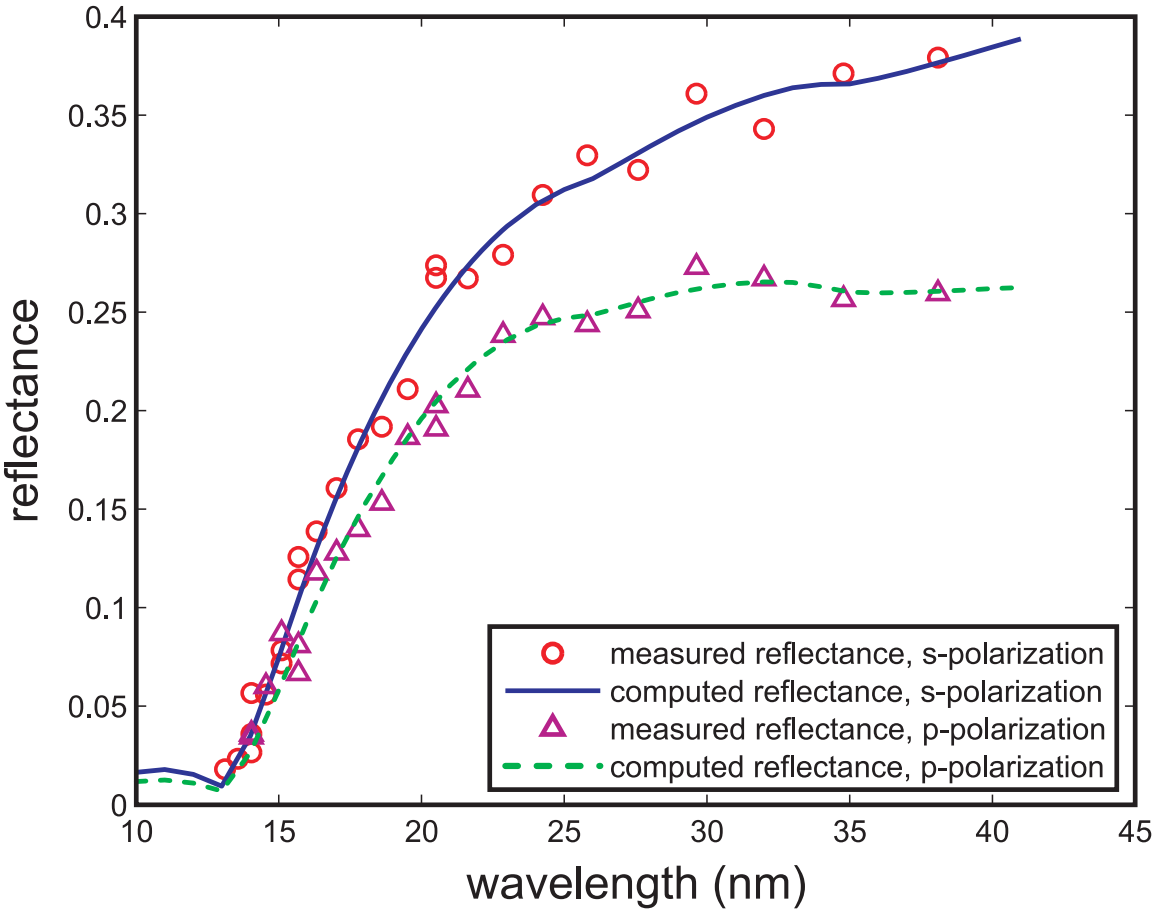

Figure 4.6 Measured s- and p-polarized reflectances (circles and triangles) from a silica sample as a function of wavelength at an incident angle of 17.5° from grazing. Also plotted are s- and p-polarized reflectances computed using the optical constants of SiO_2 (solid and dashed lines) [60].

4.5 Recovery of the Optical Constants of Silicon Dioxide

We used s-polarized reflectance measurements at four representative wavelengths to determine how well the optical constants of silicon dioxide could be recovered. The recovered optical constants along with their known values are shown in Table 4.1. The experimentally determined constants and the published constants vary somewhat, even though the error in these constants is relatively small compared to the scatter seen in the data (see Figure 4.5). This suggests that there are systematic errors in our measurements that are not negligible. These errors could include small misalignments, laser energy drift, or gas pressure variations. In Figure 4.5 you can see that frequently the s- and p-polarized data points are simultaneously higher or lower than the calculated curves. These errors could be caused by slight misalignments if different physical locations on the MCP detector have slightly different sensitivities. It is also evident in repeatability measurements (see Figure 4.3) that our measurement errors are not completely statistical. These difficulties are overcome using a technique described in chapter 5. We also show in the next chapter that the optical constants, especially κ, can be extracted with more accuracy from absolute reflectance measurements using samples that are thinner than the 27 nm sample used here. In that sense, these recovered constants are not the best that can be extracted from absolute reflectance measurements. We show in table 5.1 examples of constants extracted using absolute reflectance measurements from a 1 nm SiO_2 sample. These constants still vary somewhat from known values, but are closer than those obtained here.

wavelength	n **recovered**	n **from literature [60]**	κ **recovered**	κ **from literature [60]**
29.6 nm (q=27)	0.952±0.01	0.911	0.058±0.06	0.085
20.5 nm (q=39)	0.935±0.008	0.946	0.024±0.009	0.033
15.7 nm (q=51)	0.956±0.005	0.968	0.014±0.008	0.016
14.0 nm (q=57)	0.984±0.002	0.975	0.014±0.003	0.012

Table 4.1 Optical constants for SiO_2 recovered by fitting to absolute reflectance measurements along with their known values.

Chapter 5

Ratio Reflectance Technique for Measuring Optical Constants

As shown in the previous chapter, our absolute reflectance measurements agree reasonably well with expected reflectance curves. However, these reflectance measurements are susceptible to a number of systematic errors, such as drift in the generating laser intensity over the course of a run, alignment errors, dynamic range limitations, and possible changes in harmonic generation parameters such as gas pressure. As shown in section 4.5, the optical constants of silicon dioxide derived using absolute reflectance measurements vary somewhat from the known values (see table 4.1). However, our instrument has the capability of easily and quickly rotating linear polarization between s- and p-polarization, and we can take advantage of this to improve the accuracy of derived optical constants.

In this chapter we demonstrate the technique of determining optical constants from the ratio of p-polarized to s-polarized reflectance measurements (rather than from the absolute reflectance measurement for a given polarization). This technique was first suggested for visible and infrared wavelengths by Avery [83] (for bulk sam-

ples) and Miller and Taylor [84] (for thin films) and has been used to determine material optical constants at these longer wavelengths [85,86]. The technique has not previously been used in the EUV region, because of the lack of a source with easily rotatable polarization. Typical values for optical constants in the EUV (n near 1 and κ in the range 0.01-0.5) are quite different from visible and IR values. The efficacy of the ratio technique in the EUV wavelength range has not previously been explored.

We show in this chapter that the ratio technique greatly improves the performance of our instrument. We find that the ratio curve is as sensitive to the material optical constants as the absolute reflectance curves in the range from close to grazing (where reflection is best) to near Brewster's angle. Thus, there is no disadvantage in extracting optical constants from ratio measurements, but there is a significant advantage to this technique when using an EUV source prone to fluctuations or if the detector is prone to misalignments (assuming that the EUV polarization can be easily controlled).

In our technique, the signal ratio is measured for multiple incidence angles, then fit to a theoretical model to obtain optical constants. The essential requirement for implementing this technique is to have a linearly polarized EUV source that can be conveniently rotated (in our case, in about 5 seconds). Plasma sources are unpolarized, and while synchrotron light is naturally polarized, the polarization is not easily rotated. In the case of laser high harmonics, however, the polarization can be rotated with a half-wave plate in the generating laser beam. The harmonics preserve the same linear polarization as the laser [14], so the EUV polarization state can be changed by merely rotating a waveplate in the laser beam before the harmonics are generated. The measurement can be repeated many times for increased statistical accuracy against laser fluctuation. Since the ratio measurement does not rely on the value for the incident intensity, and given that systematic noise tends to contaminate

both s and p measurements in the same way, this technique removes errors owing to long-term laser drifts and alignment variation.

Another advantage of the ratio reflectance technique is that p- and s-polarized reflectances typically vary from each other by less than one order of magnitude over incident angles from 0° to 45° from grazing. This requires the detection system to have a linear response over only a modest range of intensities for an accurate measurement of the reflectance ratio. In contrast, the reflected EUV signal for typical materials is often 2-4 orders of magnitude smaller than the incident signal in this angle range, requiring wide dynamic range for absolute reflectance measurements (see section 3.3).

In our ratio technique, a single layer of the material to be characterized is deposited onto well characterized substrate. To demonstrate the effectiveness of this method, we first characterized a naturally occurring thin film of SiO_2 on a Si substrate, which is described in this chapter. Chapter 6 describes characterization of evaporated copper and uranium films. We determine the thickness of the layer using spectroscopic ellipsometry with near-visible wavelengths. Then a series of reflectance ratio measurements is obtained at a range of angles. Finally, the measured ratios are fit (using a least-squares fit) to the theoretical curve to find the optical constants of the layer.

5.1 Ratio Measurements

The ratio measurement technique was implemented using our high-harmonics-based polarimeter without need of hardware modification. We used two silicon dioxide thin films with different thicknesses: a naturally oxidized silicon sample with a SiO_2 layer of 1.0 nm$\pm$0.2 nm and a thermally oxidized silicon sample with a SiO_2 layer of 27.4 nm$\pm$0.2 nm (thicknesses were determined by spectroscopic ellipsometry). The

optical constants of SiO_2 and Si are well known [60], giving a standard by which to judge measurement errors. Figure 5.1 plots the measured ratio reflectance for the 27.4 nm thick sample at a wavelength of 29.6 nm taken on three different days to show repeatability. Also plotted for comparison is the measured s-polarized absolute reflectance for the same sample taken on three different days. This figure shows that ratio reflectance measurements are much more repeatable than absolute reflectance measurements (see section 4.2). This confirms our supposition that the ratio method would divide away many systematic errors to which absolute reflectance measurements are susceptible.

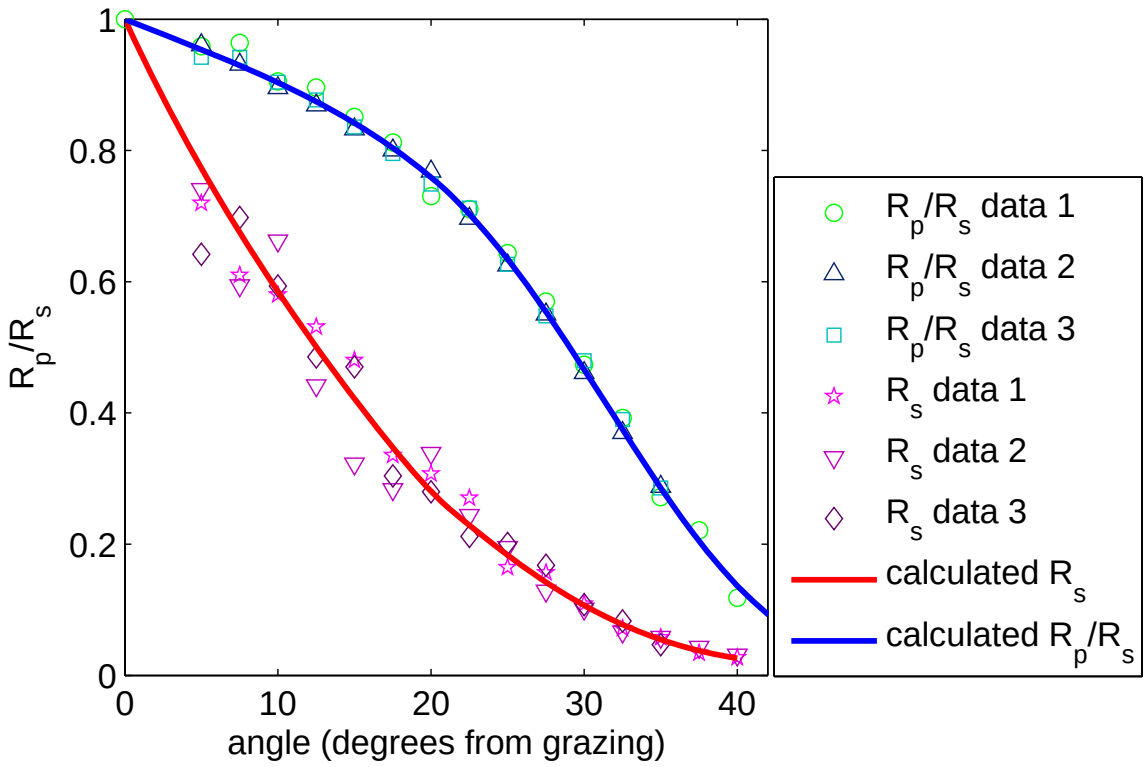

Figure 5.1 Measured ratio reflectance and absolute s-polarized reflectance of a 27.4 nm thick SiO_2 sample at a wavelength of 29.6 nm taken on three different days to show repeatability. Ratio data is much more repeatable than absolute reflectance measurements.

Figure 5.2 plots the measured absolute reflectance for s-polarized and p-polarized

light as well as the measured ratio reflectance at a wavelength of 29.6 nm for both the 27.4 nm and the 1.0 nm sample. Each point represents an average of 400 shots at an effective frequency of about 3 Hz (because of laser energy discrimination described in section 3.5). The lines show best-fit curves calculated from the model described in section 4.3 with n and κ for the SiO_2 layer taken as free parameters in a least-squares fitting algorithm. Note that the scatter in measured values for the ratio reflectance is much lower than that of the two absolute reflectances. As discussed above, this is owing to the fact that the ratio measurement is insensitive to possible long-term systematic errors. In principle, the remaining error can be reduced by averaging more measurements to the extent that the error is statistical in nature.

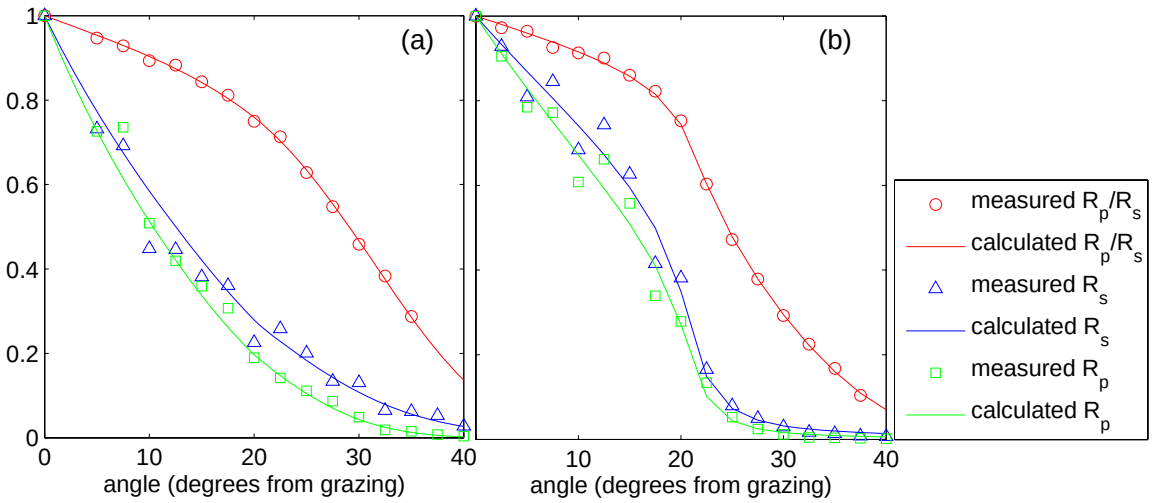

Figure 5.2 Measured and fit s- and p-polarized absolute reflectances and the ratio of p-polarized to s-polarized reflectance from a silica sample at λ=29.6 nm with a thickness of (a) 27 nm and (b) 1 nm.

Figure 5.3 shows the measured and fit ratio reflectance from the 1 nm thick sample for five wavelengths. The fits model well features seen in measured data, such as the shoulder seen in these plots.

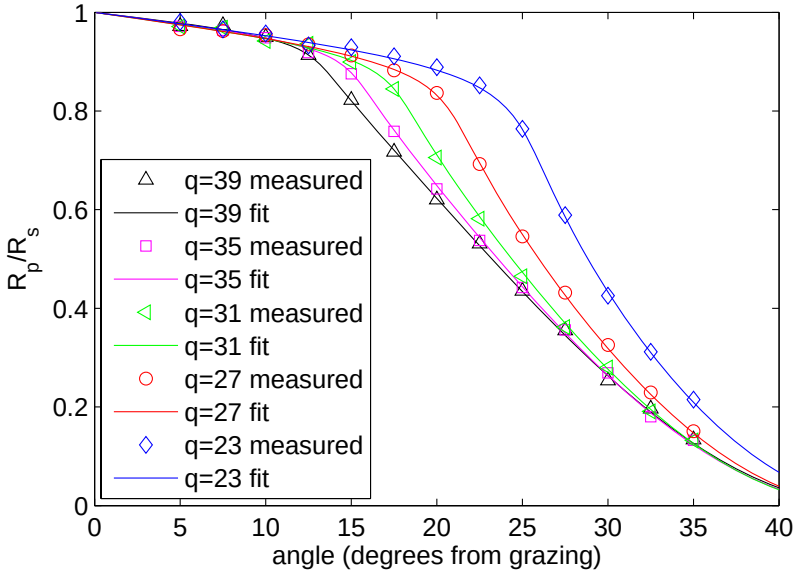

Figure 5.3 Measured and fit ratio of p-polarized to s-polarized reflectance from a 1 nm thick silica sample at five wavelengths: q=39 (λ=20.5 nm), q=35 (λ=22.9 nm), q=31 (λ=25.8 nm), q=27 (λ=29.6 nm), and q=23 (λ=34.8 nm).

5.2 Ratio Calculations

Given that we can make a measurement of R_p/R_s with more accuracy than we can measure absolute reflectance of either polarization, an important question is whether we can derive optical constants from reflectance ratio measurements with the same efficiency as can be derived from ideal absolute reflectance measurements. To extract optical constants accurately, the theoretical curve for R_p/R_s must be sensitive to variations in the constants. Figure 5.4 shows calculated plots of s-polarized absolute reflectance and the ratio of p-polarized to s-polarized reflectance at a wavelength of 29.6 nm as n and κ are varied. The heavier lines in Figure 5.4 show the reflectance and reflectance ratio for a film with n and κ chosen to be the constants of silicon dioxide at a wavelength of 29.6 nm (n=0.911, κ=0.085) and the film thickness chosen to be 1 nm. The dashed curves show the variation in the curves as n and κ are each changed by $\pm$0.05 from their actual values. We can see from these plots that variation in the

constants results in similar changes in the ratio reflectance and s-polarized absolute reflectance curves. (The R_p curve shows somewhat less variation than either of the ones plotted.)

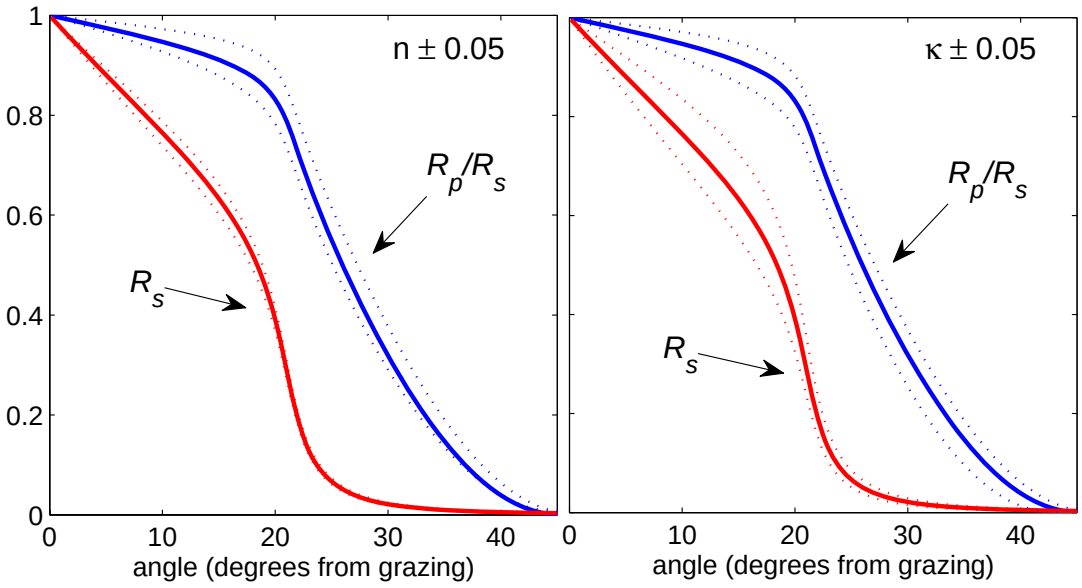

Figure 5.4 Calculated plots of s-polarized absolute reflectance and the ratio of p-polarized to s-polarized reflectance from a single layer of SiO_2 on Si at a wavelength of 29.6 nm. Solid curves show the accepted values of n=0.911 and κ=0.085 and a thickness of 1 nm. Dashed curves show the extent of the change when (left) n is varied by ±0.05 with κ held fixed, and (right) κ is varied by ±0.05 with n held fixed. These curves show that the ratio reflectance curves show as much variation as absolute reflectance curves as optical constants are changed.

To effectively extract κ from either a ratio reflectance measurement or an absolute reflectance measurement, film thicknesses need to be relatively thin. κ primarily influences absorption. Accordingly, to see the effects of absorption in a reflectance measurement, an appreciable fraction of light entering the film needs to travel through the film, reflect from the substrate, and return and join the reflected signal. Once a film is thicker than a few absorption depths (considered from the perspective of the incident angle), essentially all of the light that enters the material gets absorbed.

Figure 5.5 shows calculated plots of s-polarized absolute reflectance and the ratio reflectance as κ is varied by ± 0.05 (n is held fixed at 0.911). The left plot shows the curve variation with a film thickness of 1 nm with, and the right plot shows the curve variation with a film thickness of 27 nm. These plots show that absolute reflectance and ratio reflectance measurements are only sensitive to changes in κ if the film thickness is relatively small. Recall that in chapter 4 we recovered the constants for silicon dioxide using the absolute reflectance of a 27.4 nm thick sample. The disagreement of these recovered constants with known values, shown in Table 4.1, is partly due to the use of this thick sample. Using absolute reflectance from a thin sample leads to somewhat better recovery of optical constants, as shown in Table 5.1.

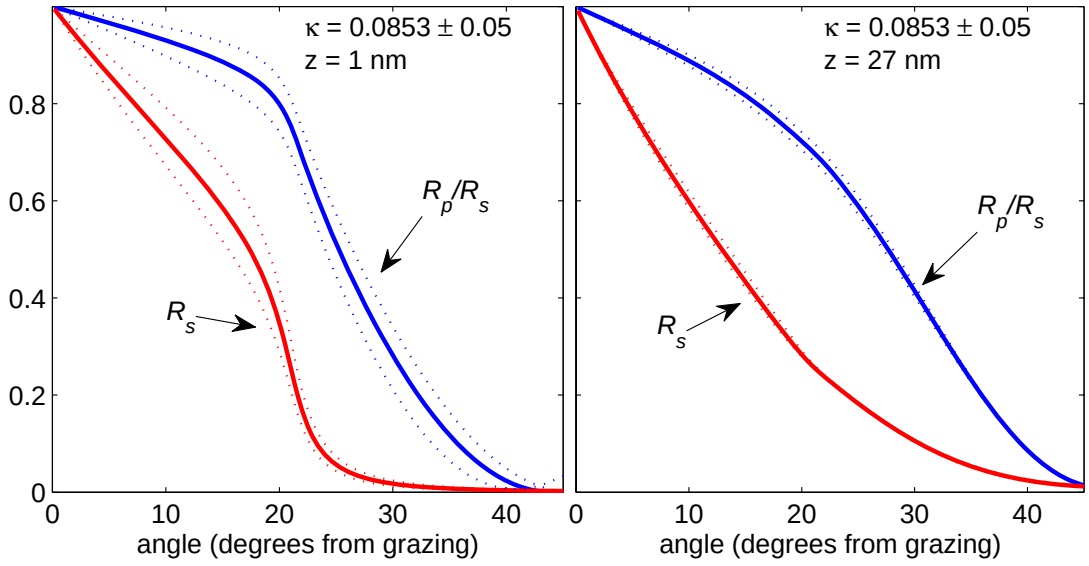

Figure 5.5 Calculated plots of s-polarized absolute reflectance and the ratio of p-polarized to s-polarized reflectance from a single layer of SiO_2 on Si at a wavelength of 29.6 nm. Solid curves show the accepted values of n=0.911 and κ=0.085 with a thickness of 1 nm (left) and a thickness of 27 nm (right). Dashed curves show the extent of the change when κ is varied by ± 0.05. These curves show that κ can only be extracted efficiently from absolute or ratio reflectance curves if the film thickness is relatively thin.

We have also found in this analysis that changes in κ and changes in film thickness

unfortunately result in similar changes to both the absolute reflectance and the ratio reflectance curves. Figure 5.6 shows calculated plots of s-polarized absolute reflectance and the ratio reflectance as (left) κ is varied by ± 0.05 and (right) thickness is varied by ± 0.5 nm. The changes in the curves looks similar for variations in κ and variations in thickness. Thus, it is difficult for the fitting algorithm to accurately determine both κ and film thickness independently. Because of this, it is useful to determine film thicknesses using spectroscopic ellipsometry and fix that value in a fit to measured data. As a side note, there is a known effect where the index of refraction of a material depends on the thickness of the film, called the anomalous skin effect. When making multilayer mirrors, researchers typically use very thin films, with thicknesses similar to those used here. Thus, we presume to be measuring the optical constants of materials as they will be used in multilayer coatings.

This computational analysis indicates that we can deduce accurate values for optical constants by fitting to ratio reflectance curves as well or better than to (low-noise) absolute reflectance data. In addition, we find that it is advantageous in fitting using either ratio reflectance measurements or absolute reflectance measurements to (1) keep film thicknesses relatively thin and (2) determine film thicknesses using spectroscopic ellipsometry or some other means and keep that value fixed during a fit.

As a side note, through this section we have plotted curves with incident angles from 0 to 45 degrees from grazing, which is the angle range where materials have sizable reflectances in the EUV. However, this also happens to be the angle range where ratio reflectance curves show the most sensitivity to optical constant values. Figure 5.7 plots the ratio reflectance for a 1 nm SiO_2 sample as n is varied by ± 0.05. This plot shows that between Brewster's angle ($\sim 45°$) and near-normal incidence there is very little curve variation as n is changed. It is fortuitous in that the angle

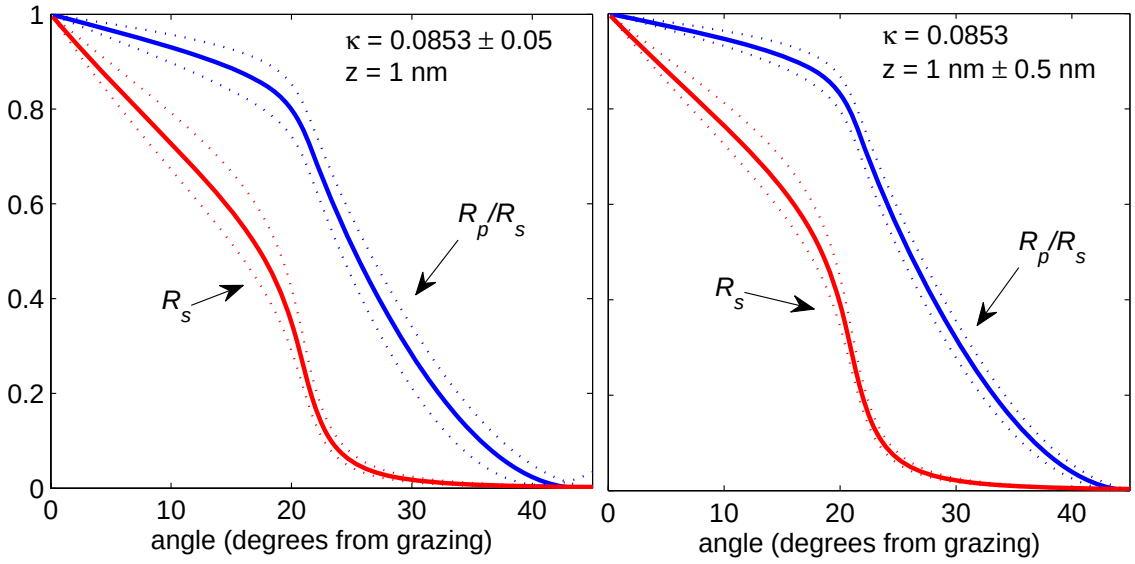

Figure 5.6 Calculated plots of s-polarized absolute reflectance and the ratio of p-polarized to s-polarized reflectance from a single layer of SiO_2 on Si at a wavelength of 29.6 nm. Solid curves show the accepted values of n=0.911 and κ=0.085 and a thickness of 1 nm. Dashed curves show the extent of the change when (left) κ is varied by $\pm$0.05 and (right) thickness is varied by $\pm$0.5 nm. These curves show that changes in κ and changes in film thickness result in similar curve variation for both absolute and ratio reflectance.

range where ratio curves are most sensitive to optical constants is also the range where reflectance is highest.

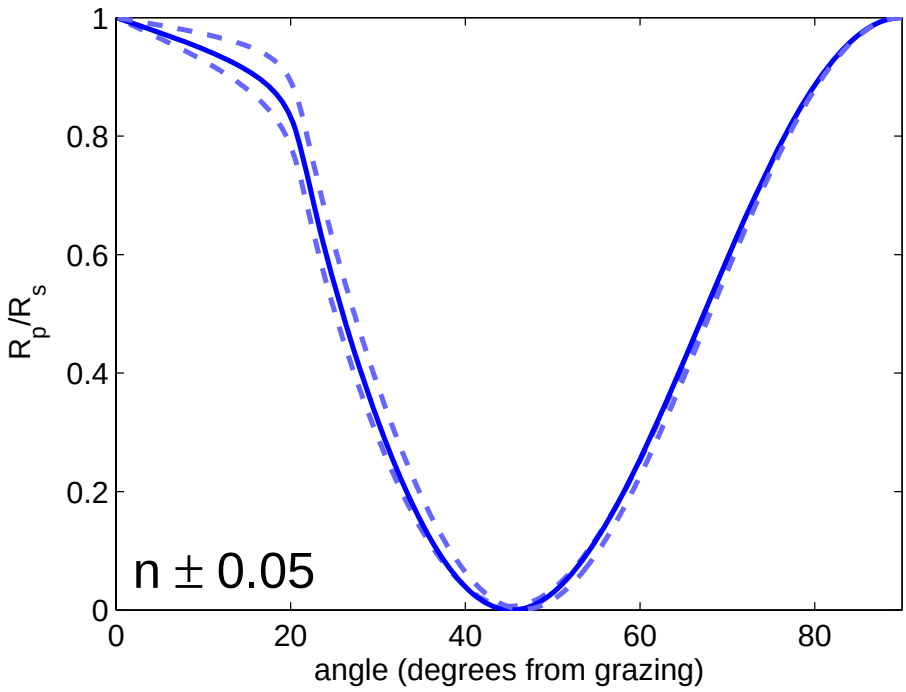

Figure 5.7 Calculated plot the ratio reflectance from a single layer of SiO_2 on Si at a wavelength of 29.6 nm from 0 to 90 degrees from grazing as n is varied. The solid curve shows the accepted values of n=0.911 and κ=0.085 and a thickness of 1 nm. Dashed curves show the extent of the change when n is varied by $\pm$0.05. These curves show that the ratio reflectance is most sensitive to optical constant values in the angle range between 0° and Brewster's angle.

5.3 Validation

We used our measured data (shown in Figure 5.2) to evaluate how well the optical constants for the 1 nm thick SiO_2 film could be recovered from ratio reflectance data. We used a least-squares fitting algorithm to find the complex index of the SiO_2 film with the thickness fixed at 1 nm (as measured with spectroscopic ellipsometry) and the optical constants of the Si substrate fixed at their accepted values. We also included

wavelength	n **recovered with ratio reflectance**	n **recovered with absolute reflectance**	n **from literature [60]**
29.6 nm (q=27)	0.911±0.006	0.941±0.01	0.911
34.8 nm (q=23)	0.898±0.002	0.926±0.009	0.900
wavelength	κ **recovered with ratio reflectance**	κ **recovered with absolute reflectance**	κ **from literature [60]**
29.6 nm (q=27)	0.086±0.003	0.043±0.04	0.085
34.8 nm (q=23)	0.120±0.003	0.148±0.008	0.122

Table 5.1 Optical constants for SiO_2 recovered by fitting to ratio reflectance measurements, recovered by fitting to absolute reflectance measurements, and their known values.

the effect of a thin contamination layer that formed on the sample (see section 5.4). The recovered optical constants along with their known values are shown in Table 5.1. The ratio technique gave excellent agreement. For comparison, we also show the optical constants recovered using absolute reflectance data, described in section 4.5. As discussed above, the absolute measurements were subject to systematic errors owing to possible detector alignment errors and long-term drifts in the high-harmonic EUV source. When these data points are used to determine the optical constants, they give less accurate results, which vary somewhat from the known values for SiO_2. We conclude that utilizing the ratio of p-polarized to s-polarized reflectance is a much more robust approach for extracting optical constants. This technique can significantly reduce the systematic errors to which our absolute measurements are sensitive.

5.4 Hydrocarbon Contamination

In this measurement, we found that our samples typically became contaminated with a thin layer of hydrocarbons over time. We found that cleaning with a xenon excimer

lamp (Resonance LTD) for five minutes would effectively remove the contaminant. However, even during transfer from the cleaning area to the measurement chamber, our samples would often accumulate a layer of hydrocarbons (less than 1 nm). Our algorithm also had to determine the constants for the contaminant layer (the thickness of the contaminant having been characterized by a separate ellipsometry measurement) in order to extract the constants for the SiO_2 layer. We used the optical constants of carbon for this first layer when determining the constants for SiO_2. Conversely, we obtained the optical constants of carbon when the constants for SiO_2 were used for the layer beneath the contaminant. In subsequent experiments, we alleviated this problem by doing *in-situ* deposition and measurement (an advantage for our instrument) for which sample contamination became less of an issue.

Chapter 6

Optical Constants for Thin Films of Copper and Uranium

In this chapter we present measured optical constants of copper, uranium, and their natural oxides in the range from 10 nm to 47 nm determined using the ratio-reflectance technique described in Chapter 5. This is one of the first times that high harmonics have been used in a work-horse setting to make measurements important to another field, rather than just demonstrating proof of principle. We have attached an evaporator to our polarimeter so that we are able to evaporate copper and uranium and then make reflectance measurements without breaking vacuum (*in-situ* measurements). We selected copper for this study for the sake of its evaporation characteristics (similar to uranium) even though it is not a strategic EUV material. We expected to verify previously accepted values for copper in this range, but we determined that they were actually the constants of oxidized copper. On the other hand, uranium was suggested as a high-reflectance material in the EUV several years ago [61] and has even been used in a multilayer mirror on the IMAGE satellite [52]. However, difficulties with oxidation have prevented the careful measurement of uranium's optical

constants. EUV polarimetry with high harmonics has afforded an opportunity for *in-situ* measurements of uranium at a broad range of EUV wavelengths for the first time.

6.1 Interest in Copper

The optical properties of copper in the ultraviolet and extreme ultraviolet have been studied previous to this work [87–90]. We initially undertook a study of copper as a known sample by which we could validate our deposition and *in-situ* measurement techniques. However, we concluded that our measured optical constants for copper metal did not agree with values cited by the Center for X-ray Optics (CXRO) website [91]. After investigating other references, we found that discrepancies were most likely due to previous researcher's failure to keep samples from partially oxidizing before measurement. Copper is now being used an interconnect material in microelectronics, having replaced aluminum for many applications because of its higher conductivity. With the advent of EUV lithography it was important to resolve these differences in the reported optical properties of copper.

The index of refraction for copper cited by CXRO is determined using photoabsorption measurements made by Hagemann et al. in reference [87]. In this publication, measurements were not made *in-situ*. However, they deposited a 5 nm capping layer of carbon onto the copper samples before exposure to air to prevent oxidation. We suspect that something went wrong in this attempt to prevent oxidation. Optical properties of naturally oxidized copper films (not *in-situ*) have been made from 5-34 nm by Haensel [88] and from 8-30 nm by Tomboulian [89]. *In-situ* measurements have been made from 35-70 nm by Beaglehole [90]. Our optical constants for copper metal agree with these *in-situ* measurements by Beaglehole and with the

measurements made by Tomboulian. Measurements made by Haensel and Hagemann agree with our measurements of oxidized copper. This suggests that constants determined by Hagemann, which are commonly used as the constants of copper metal, are actually the constants of oxidized copper.

6.2 Interest in Uranium

As discussed throughout this work, the optical constants of many materials have not yet been measured in the extreme ultraviolet (10-100 nm). This is true for most materials of the actinide group because the reactivity, toxicity, and (sometimes) radioactivity of these materials adds challenges to performing optical measurements in the EUV range. The literature contains little information on the optical properties of uranium in the EUV. Faldt and Nisson [92] evaporated uranium and measured optical constants *in-situ* using ellipsometry and normal-incidence reflectometry in the range from 50 to 2000 nm. Cukier and co-workers [93] measured the photoabsorption of uranium films from 2.7 nm to 9.5 nm, where oxidation was prevented with aluminum capping layers. S. Lunt [53], a master's student at BYU, studied the optical properties of oxidized uranium films in the range of 5-17 nm, and at 30.4 nm, 53.7 nm, and 58.4 nm. However, for a wide wavelength range in the EUV, no data are available, especially for unoxidized uranium.

The interest in characterizing pure uranium films arises from a theoretical as well as an experimental point of view. Calculations based on atomic scattering factors predict that uranium may have high reflectance properties in the EUV. These calculations indicate that uranium might be an excellent material for single-surface (broadband), low-angle mirrors for x-ray astronomy, with perhaps much more reflectance than nickel, gold, or iridium films commonly used [61]. Multilayer uranium/silicon

mirrors were produced by the BYU group of Allred and Turley for use on the IMAGE satellite launched in 2000 [52], which required high reflectance at 30.4 nm but low reflectance at 58.4 nm. While making these multilayer mirrors, the BYU group concluded that the optical constants cited by Henke did not describe the reflectance well. In fact, these mirrors reflected better than expected, and better than many other commonly-used materials in this region [94]. This experience calls for a careful characterization of the optical constants of uranium.

6.3 Deposition Experimental Setup

We fitted the polarimeter instrument described in Chapter 3 with evaporation equipment for *in-situ* deposition of thin films. The deposition system consists of two connected vacuum chambers, one for thin-film deposition and the other for reflectance measurements, as shown in Figure 6.1. The reflectance chamber and deposition chamber are initially open to each other while the system is pumped with a roughing pump (Varian 600DS) and a turbo pump (Varian TV 551 Navigator) to a pressure of 1×10^{-4} torr. The sample is then moved out of the beam path and rotated so that it presses up against an o-ring attached to a bellows, creating a seal that isolates the deposition chamber from the reflectance chamber. The deposition chamber is evacuated further with a sorption pump (Varian 941-6501) cooled with liquid nitrogen to a pressure of 10^{-5} torr. After deposition, the deposition chamber and reflectance chamber are again open to each other, and reflectance measurements are made at a pressure of 1×10^{-4} torr. A photograph and schematic of the deposition chamber are shown in Figure 6.2.

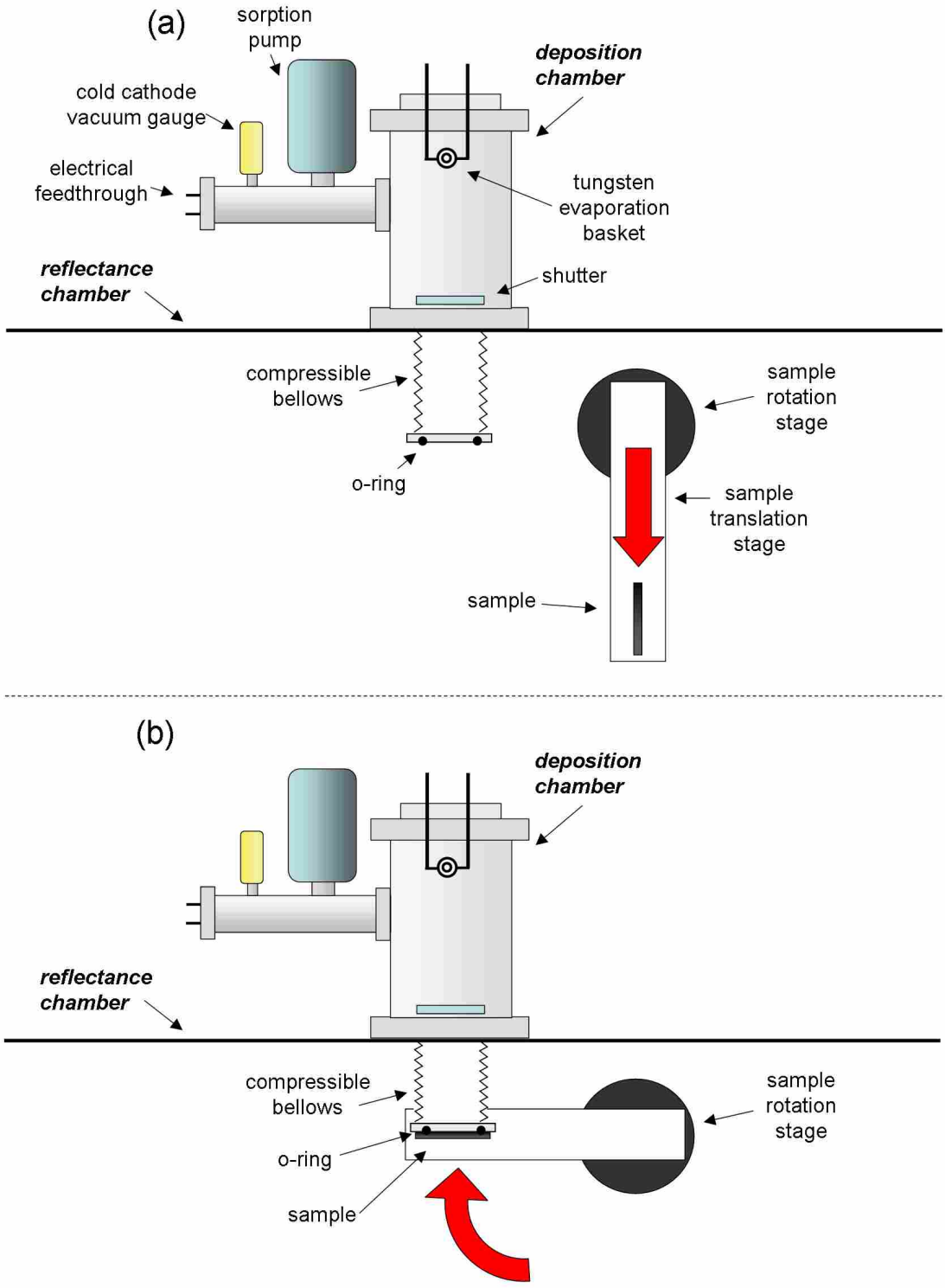

Figure 6.1 Schematic of deposition apparatus (top view). (a) The sample is moved out of the beam path using a linear translation stage. (b) The sample is rotated until it presses against an o-ring on a compressible bellows, forming a seal.

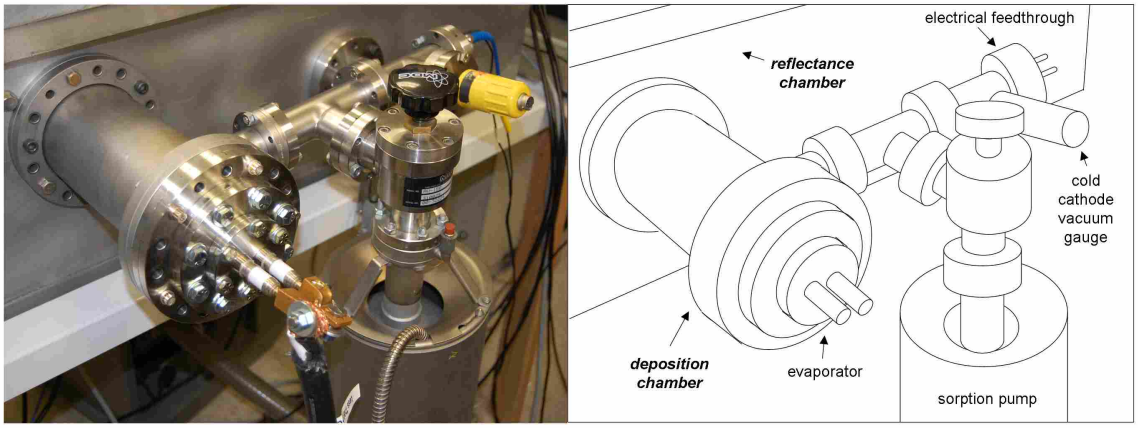

Figure 6.2 Photograph and schematic of deposition chamber.

6.4 Deposition of Copper and Measurements

Copper of 99.99% purity was evaporated horizontally using a tungsten basket (R.D. Mathis, B12B-3X.025W16) onto polished silicon 100 substrates (with a natural SiO_2 layer) at a distance of 35 cm. The silicon substrates were cleaned with a xenon excimer lamp (Resonance LTD) for five minutes immediately before pumping down the system to avoid hydrocarbon contamination. The copper deposition was designed to achieve a film thickness between 7 and 12 nm by evaporating completely everything in the basket.

Ratio reflectance measurements were performed *in-situ* on samples at room temperature using the technique described in Chapter 5. After reflectance measurements were made, the copper samples were exposed to atmosphere and immediately ($\sim$5 minutes) measured with spectroscopic ellipsometry to determine the thickness of the metal and the oxide that had formed since air exposure. This oxide layer was found to be about 0.7 nm of CuO after five minutes of air exposure and grew initially at a rate of about 0.1 nm/minute. Oxidation later slowed to about 0.02 nm/minute.

For measurements of the optical properties of CuO_x, copper samples were heated to about 300°F for 5 minutes, after which they were found to be fully oxidized using the spectroscopic ellipsometer. We are unsure of the exact state of oxidized copper that formed naturally after this process, and so we will refer to the naturally oxidized copper as CuO_x. Here, x denotes the ratio of oxygen to copper in the sample, which is unknown. Copper and CuO_x films thicker than 5 nm were measured with atomic force microscopy to have a roughness less than 1 nm (rms) on a 1 μm×1 μm scale. With thinner films, we found that the copper would agglomerate on the surface, forming islands and not providing full coverage. This is presumably a surface effect, which we were careful to avoid.

6.5 Ratio Reflectance Data and Optical Constants for Copper

Figures 6.3 and 6.4 show the ratio reflectance and fit of Cu and CuO_x respectively at representative wavelengths of 10.1 nm, 18.6 nm, 25.8 nm, and 34.8 nm. Each point represents an average of 400 shots at an effective frequency of about 3 Hz (because of laser energy discrimination of ±10% described in section 3.5). The lines show best-fit curves calculated from the model described in section 4.3 with n and κ for the test layer taken as free parameters in a least-squares fitting algorithm. The thickness of the SiO_2 layer was measured using spectroscopic ellipsometry and held fixed during the fit. The optical constants for the silicon dioxide layer and silicon substrate were also held fixed. For CuO_x, the thickness of the layer was measured using spectroscopic ellipsometry and held fixed during the fit. The variation of the thickness across 2 cm of the sample (measured with ellipsometry) was about 0.2 nm, and the uncertainty in the ellipsometry fit was about 0.2 nm. Combining these uncertainties in quadrature gives

an uncertainty in this thickness of about ±0.3 nm. For copper, the thickness of the layer was determined from the ellipsometric measurement of the oxide layer thickness using the ratio of the densities of the metal and the oxide (densities for copper and CuO were used, 8.96 g/cm^3 and 6.31 g/cm^3 respectively). This thickness was accurate to approximately ±0.7 nm, due to uncertainties in the density and/or composition of the oxide, variation across the sample, and uncertainties in the ellipsometry fit. The data show features such as in the $\lambda = 34.8$ nm fit of copper that the model reproduces well. These features have to do with the thickness of the layer, as well as n and κ.

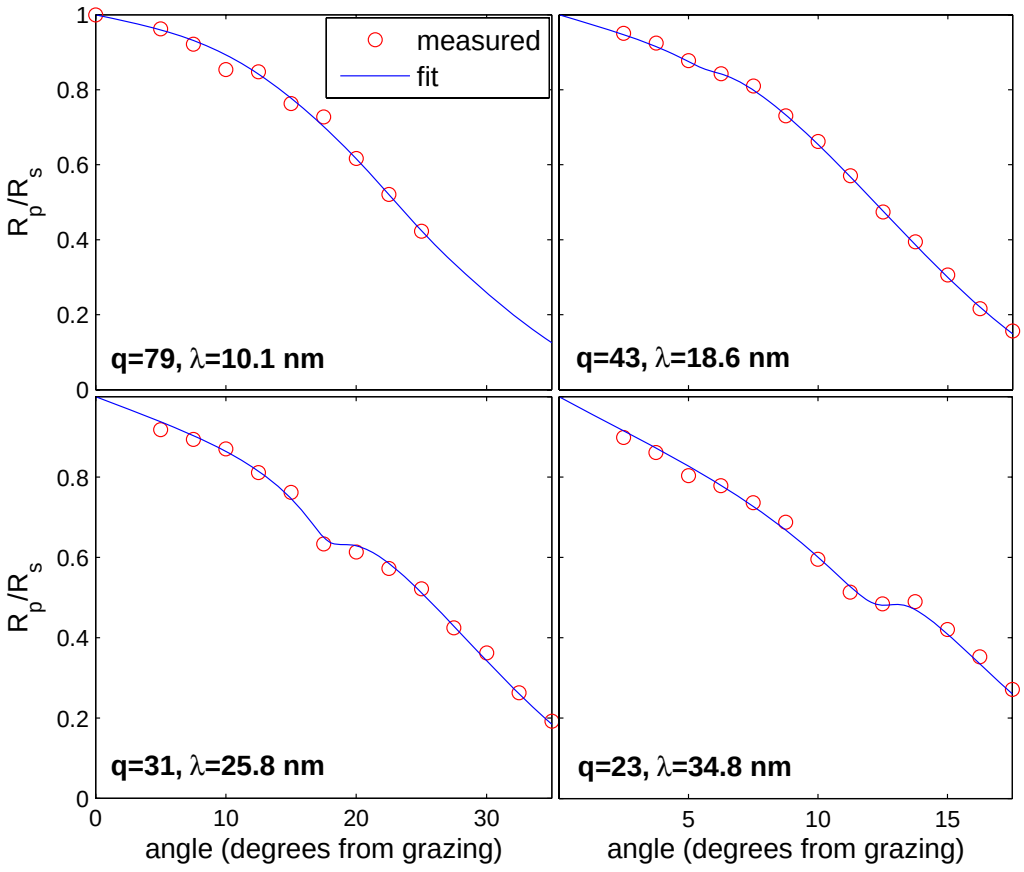

Figure 6.3 The measured ratio reflectance and fit of copper at four representative wavelengths: 10.1 nm, 18.6 nm, 25.8 nm, and 34.8 nm.

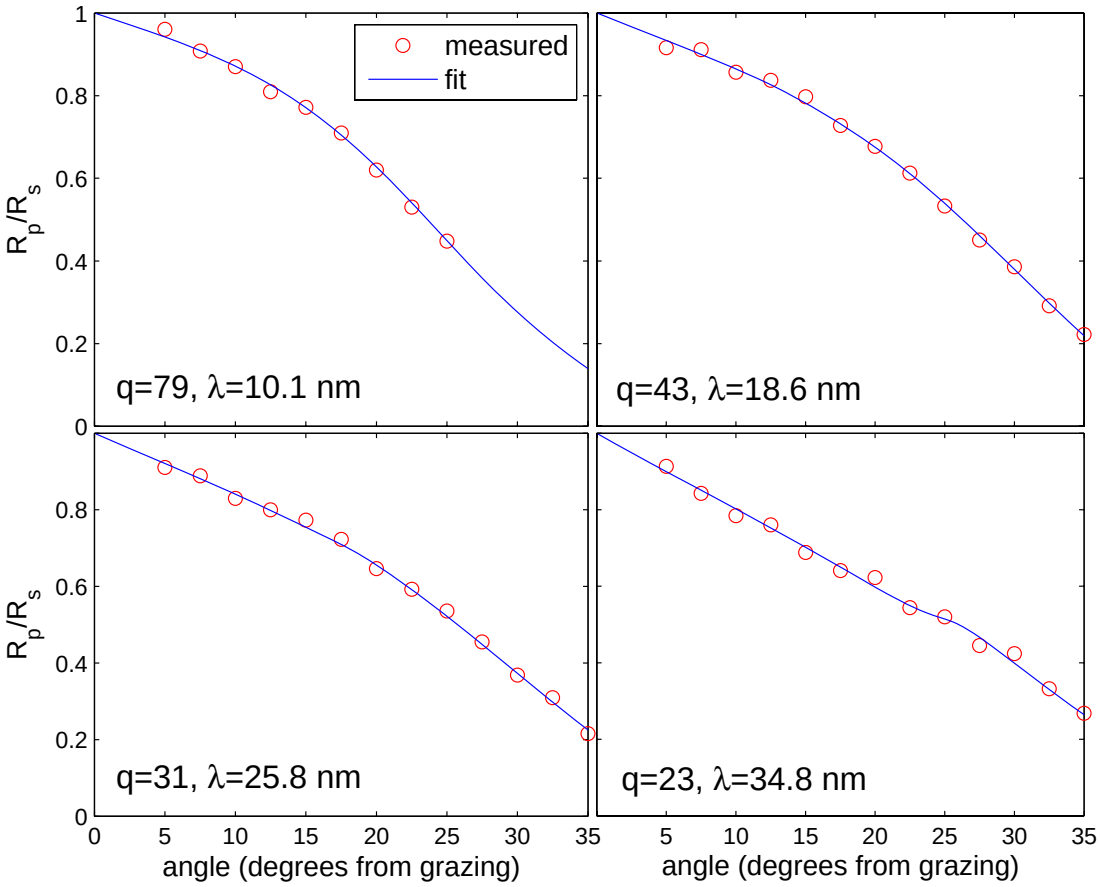

Figure 6.4 The measured ratio reflectance and fit of CuO_x at four representative wavelengths: 10.1 nm, 18.6 nm, 25.8 nm, and 34.8 nm.

The optical constants for Cu and CuO_x are shown in Figure 6.5. Error bars shown in this plot are those produced by the fitting algorithm and are associated with the fit error and also the uniqueness of the ratio curve (see section 5.2). Optical constants are also listed in numeric form in Table 6.1.

An important question is how much the uncertainties in film thickness will affect values for optical constants. We re-fit each data set for the maximum and minimum thicknesses set by our uncertainties (with the thickness fixed) to see how much our fit values for optical constants changed. At an example wavelength, $\lambda = 15.1$ nm, q=53, changing the thickness from 7.4 nm to 8.1 nm (for our uncertainty of 0.7 nm) changes n by 0.0026 and κ by 0.0052. Similarly, changing the thickness from 7.4 nm to 6.7 nm (for our uncertainty of 0.7 nm) changes n by -0.0026 and κ by -0.0045. At each wavelength we added in quadrature the statistical error due to the fit and this error due to uncertainty in the film thickness. Figure 6.6 shows a plot of measured optical constants for copper and the extent of the curve change due to these errors. Figure 6.7 shows a similar plot for CuO_x. Our total error for values of n is about 0.009, and our total error for values of κ is about 0.01.

Figure 6.8 shows a plot of measured κ for copper and CuO_x along with those measured by Hagemann [87], Haensel [88], Tomboulian [89], and Beaglehole [90]. The measurements by Hagemann are those cited on the CXRO website [91]. Because Hagemann, Haensel, and Tomboulian measured photoabsorption only, we only plot κ here. Our measured κ for copper matches data measured *in-situ* by Beaglehole. Values for n measured by Beaglehole match our measured n for copper as well (not shown). This agreement demonstrates that Beaglehole's and our measurements were taken on copper metal, rather than oxidized copper. *In-situ* measurements are very reliable at preventing oxidation because there is virtually no chance for oxygen to be in contact with the sample when the sample remains under vacuum through the

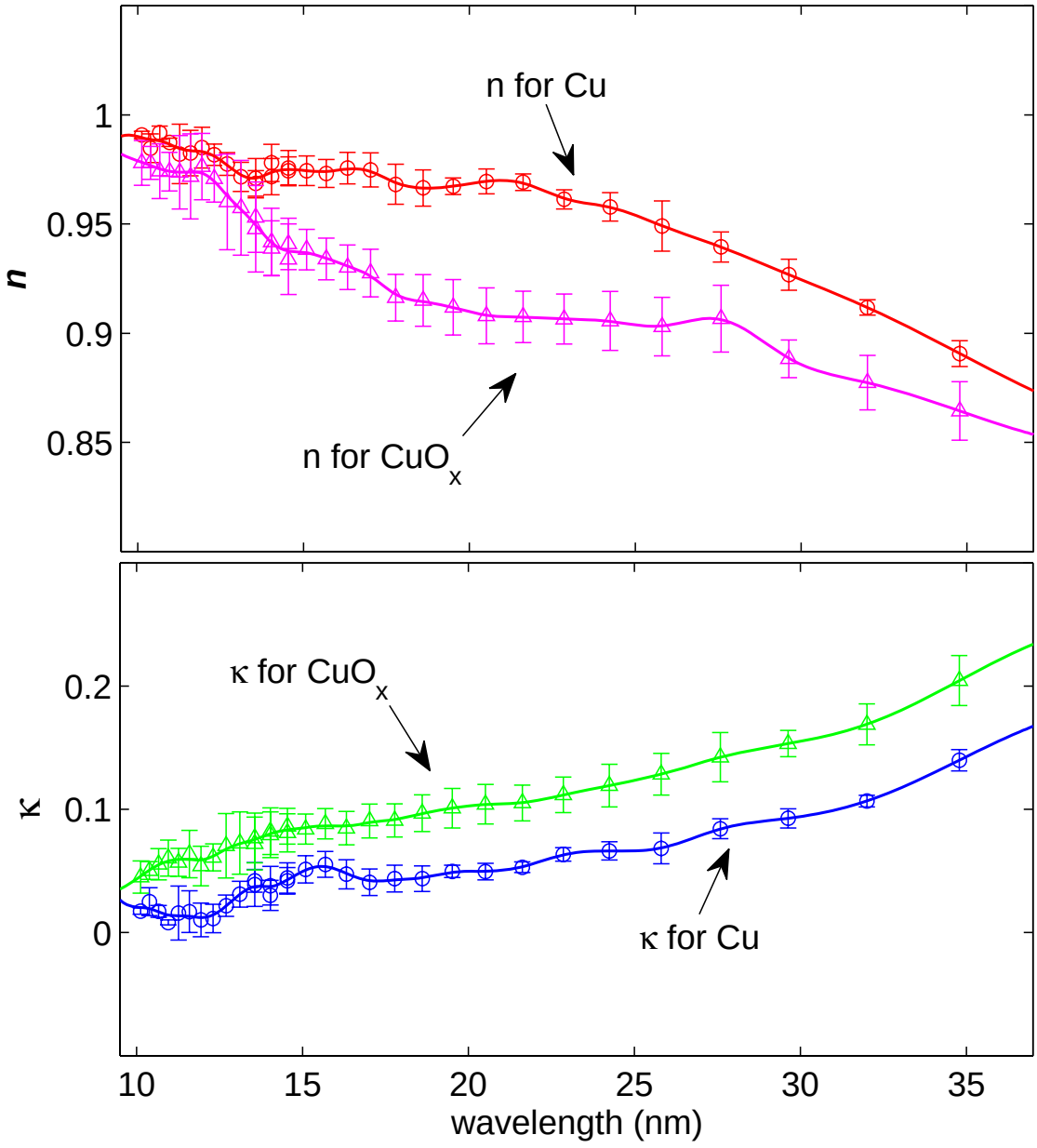

Figure 6.5 The optical constants of Cu and CuO_x determined using the ratio reflectance technique. Statistical error bars are also shown.

wavelength (nm)	n **for Cu**	κ **for Cu**	n **for** $\mathbf{CuO_x}$	κ **for** $\mathbf{CuO_x}$
10.1	0.991	0.017	0.978	0.045
10.4	0.985	0.025	0.978	0.050
10.7	0.992	0.017	0.974	0.055
11.0	0.987	0.008	0.974	0.060
11.3	0.982	0.016	0.974	0.057
11.6	0.983	0.017	0.972	0.064
11.9	0.985	0.010	0.976	0.054
12.3	0.982	0.011	0.971	0.061
12.7	0.978	0.022	0.960	0.070
13.1	0.972	0.031	0.957	0.073
13.6	0.971	0.039	0.948	0.072
14.0	0.978	0.038	0.939	0.082
14.6	0.976	0.044	0.934	0.086
15.0	0.974	0.051	0.938	0.084
15.7	0.973	0.055	0.934	0.088
16.3	0.976	0.047	0.930	0.085
17.0	0.975	0.041	0.928	0.091
17.8	0.968	0.044	0.916	0.091
18.6	0.967	0.044	0.915	0.097
19.5	0.967	0.050	0.912	0.101
20.5	0.970	0.050	0.908	0.104
21.6	0.969	0.053	0.908	0.105
22.9	0.961	0.063	0.907	0.112
24.2	0.958	0.066	0.906	0.119
25.8	0.949	0.068	0.903	0.128
27.6	0.940	0.084	0.907	0.142
29.6	0.927	0.093	0.888	0.153
32.0	0.912	0.107	0.877	0.169
34.8	0.891	0.140	0.864	0.204

Table 6.1 Optical constants of Cu and CuO_x.

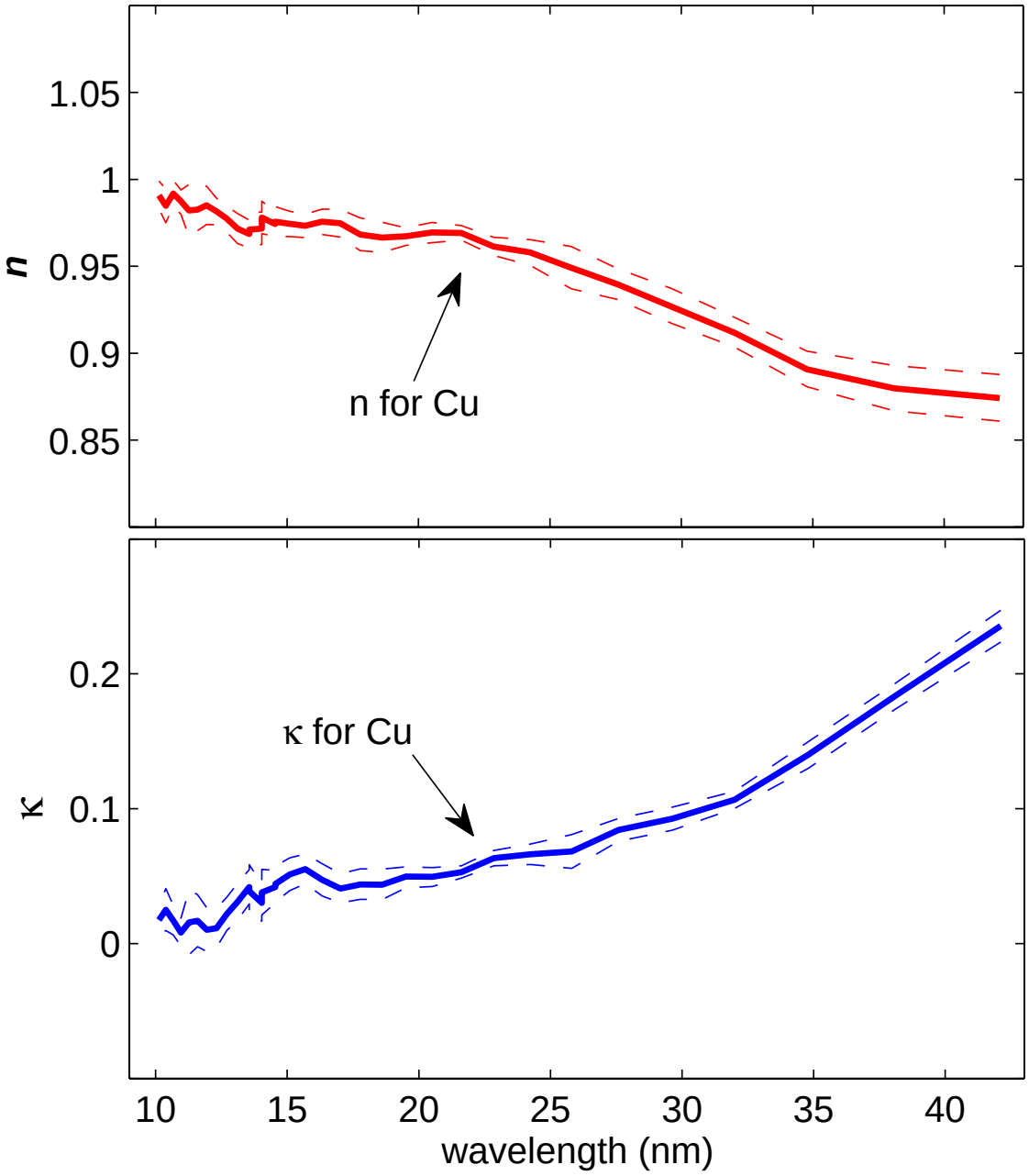

Figure 6.6 Solid curves show the optical constants of copper. Dashed curves show the extent of the change when statistical errors and errors due to uncertainty in thickness are included.

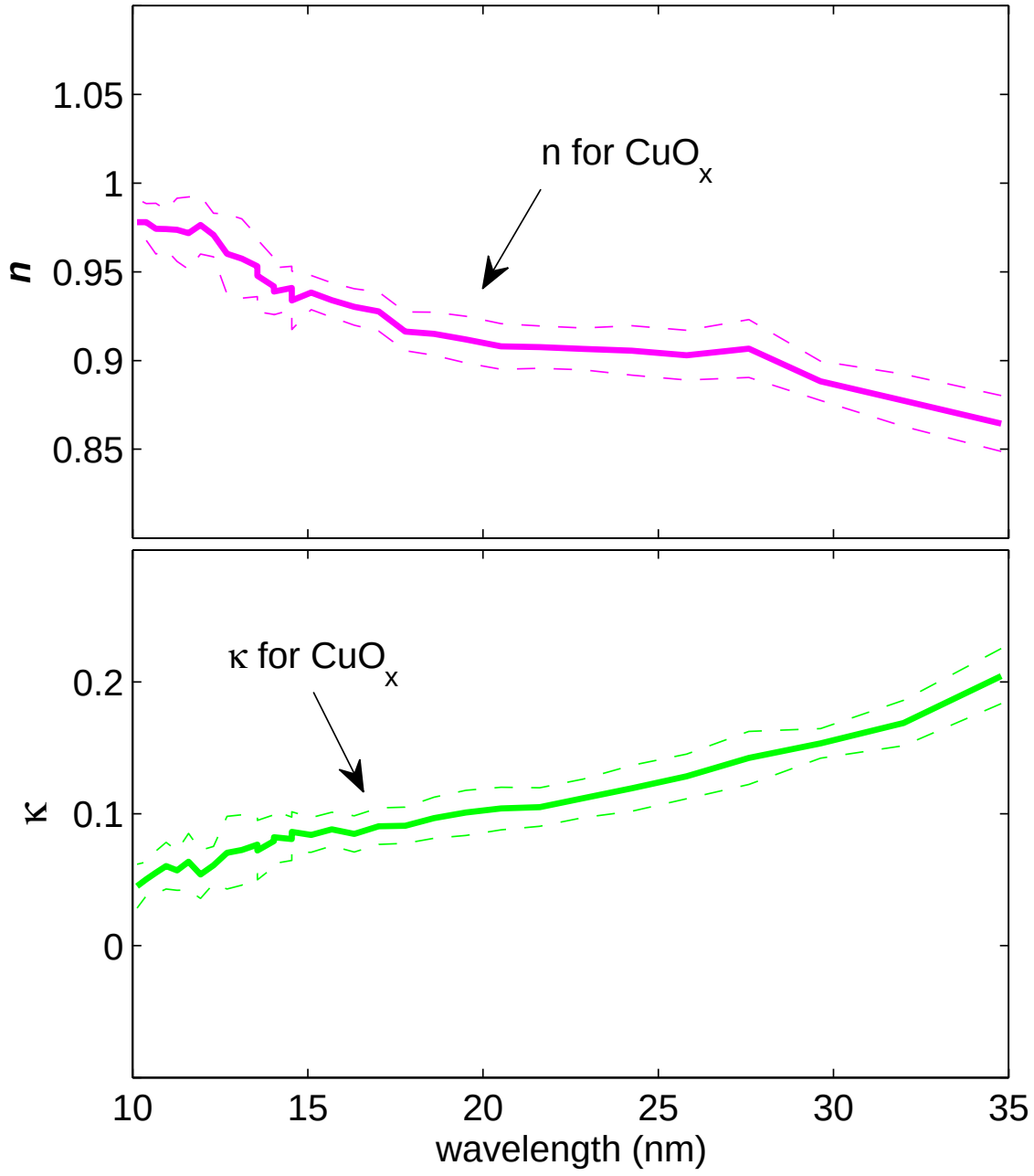

Figure 6.7 Solid curves show the optical constants of oxidized copper. Dashed curves show the extent of the change when statistical errors and errors due to uncertainty in thickness are included.

entire deposition and measurement process.

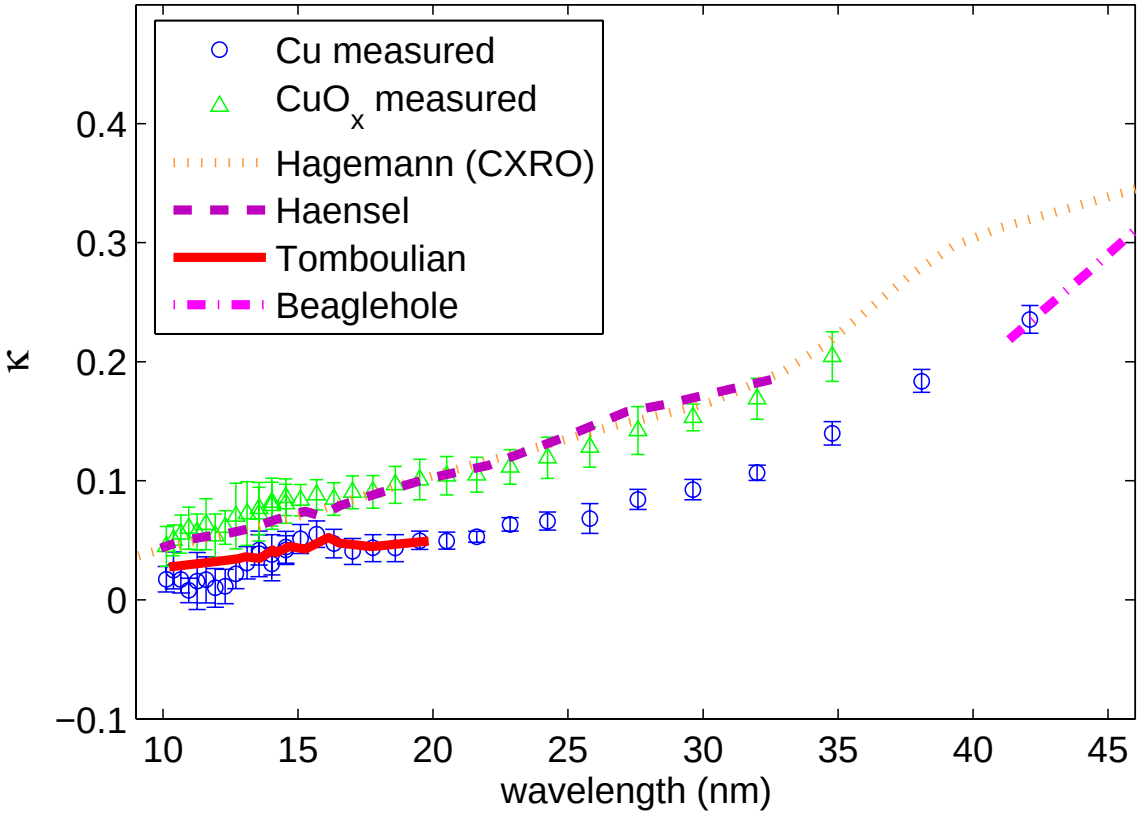

Figure 6.8 Measured κ of copper and oxidized copper compared with κ measured by Hagemann [87], Haensel [88], Tomboulian [89], and Beaglehole [90]. Our κ for copper matches that of Beaglehole (measured *in-situ*) and Tomboulian (not measured *in-situ*). Our κ for oxidized copper matches that of Haensel (not measured *in-situ*) and Hagemann (measured with a carbon capping layer).

Unexpectedly, our data for copper metal also matches values measured by Tomboulian, although these measurements were not made *in-situ*. However, Tomboulian stated that they minimized as much as possible the time that their samples were exposed to air (only a minute or two). In our experience, we found that copper samples oxidized less than 1 nm in 5 minutes of air exposure. This suggests that Tomboulian's samples may have sustained minimal oxidation (less than 0.5 nm) in transfer to the measurement chamber. This small amount of oxidation may not have

affected measured optical constants very much, especially because Tomboulian measured absorption of samples thicker than 50 nm. This suggests less than 1% error in transmission measurements.

Our values of κ for naturally oxidized copper agree with values measured by Haensel (not *in-situ*), as expected. Haensel did not report taking any measures to prevent or minimize sample oxidation, and samples he used were as thin as 5 nm. We thus presume that his samples were fully oxidized at the time of measurement.

Our measured values for CuO_x also match values measured by Hagemann. Hagemann's samples were also relatively thin; some thicknesses were less than 10 nm. As mentioned previously, Hagemann and coworkers aimed to prevent sample oxidation by coating their copper samples with 5 nm carbon capping layers on both sides of the film. However, by comparing with our measured data it seems that their samples were oxidized nonetheless. We do not have enough information about Hagemann's sample preparation and measurement techniques to postulate how this could have occurred.

Although the comparisons to many of the previous data sets show disagreement, we still have confidence that our data is correct. Firstly, the other data sets do not all agree with each other. Second, we are the only investigators to report the optical constants of both copper metal and oxidized copper and show that those measurements are different. Third, our data for copper agree with the only other data set also measured *in-situ*. Capping layers can be effective, but the easiest way to be certain that no oxidation has occurred is to measure samples *in-situ*. Discrepancies between ours and other works are most likely due to previous researchers failure to keep samples from partially oxidizing before measurement.

6.6 Deposition of Uranium and Measurements

Depleted uranium of purity >99.7% was evaporated using the same equipment and baskets as used for copper onto polished silicon 100 substrates (with a natural SiO_2 layer) at a distance of 35 cm. A shutter was closed initially during the evaporation. After about 30 s of evaporation, pressure in the deposition area began to drop rapidly because the uranium began to bind to molecules in the deposition area, effectively becoming a pump. After the pressure dropped below 1×10^{-6} the shutter was opened for 10 seconds. This time frame allowed a deposition of about 2 nm of uranium metal (approximately 0.2 nm/s).

Ratio reflectance measurements were performed on uranium films *in-situ* at room temperature using the same technique as used for copper (described in Chapter 5). After exposure to atmosphere, we found that thin films oxidized completely in less than the time required to vent the chamber and make an ellipsometry measurement (∼5 minutes). This result was unexpected because oxidation rates previously reported suggested the rate should be slower. For bulk samples, rates have been measured between 0.035 nm/hour [95] and 4.6 nm/hour [96]. In either of these scenarios, though they vary greatly, we should have been able to measure the oxide growing. Atomic force microscope measurements showed uranium films to have less than 1 nm rms roughness on a 1 μm×1 μm scale. We thus hypothesize that (1) very thin films of uranium may oxidize initially more quickly than bulk or thicker films, or (2) our samples may have microchasms or voids not visible with the AFM that allow it to oxidize more quickly than a solid film. Although further investigation is beyond the scope of this work, we find that the optical constants of uranium measured *in-situ* differ significantly from the constants of oxidized uranium. This gives us confidence that we did measure the constants of uranium metal.

6.7 Ratio Reflectance Data and Optical Constants for Uranium

Figures 6.9 and 6.10 show the ratio reflectance and fit of U and UO_x, respectively, at representative wavelengths of 10.1 nm, 18.6 nm, 25.8 nm, and 34.8 nm. Each point represents an average of 400 shots at an effective repetition rate of about 3 Hz (because of laser energy discrimination of ±10% described in section 3.5). The lines show best-fit curves calculated from the model described in section 4.3 with n and κ for the test layer taken as free parameters in a least-squares fitting algorithm. The thickness of the SiO_2 layer was measured using spectroscopic ellipsometry and set to that value in the fitting algorithms. The optical constants for the silicon dioxide layer and silicon substrate were also held fixed. For UO_x, the thickness of the layer was measured using spectroscopic ellipsometry and also held fixed in the fitting algorithm. This thickness was estimated to be accurate to within about ±0.3 nm, which was the variation of the thickness across about a 2 cm-wide patch of the sample. For uranium, the thickness of the layer was determined from the ellipsometric measurement of the oxide layer thickness using the ratio of the densities of the metal and the oxide (densities for uranium and UO_2 were used, 19.1 g/cm^3 and 10.96 g/cm^3 respectively). This thickness was estimated to be accurate to approximately ±0.7 nm, due to uncertainty in the density and/or composition of the oxide along with variation across the sample. These data also show features that are reproduced well by the fit, such as the fringe in the fit of UO_x at 34.8 nm.

The optical constants for U and UO_x are shown in Figure 6.11. Error bars shown in this plot are those produced by the fitting algorithm associated with fit error and also the uniqueness of the ratio curve (see section 5.2). Optical constants are also listed in numeric form in Table 6.2.

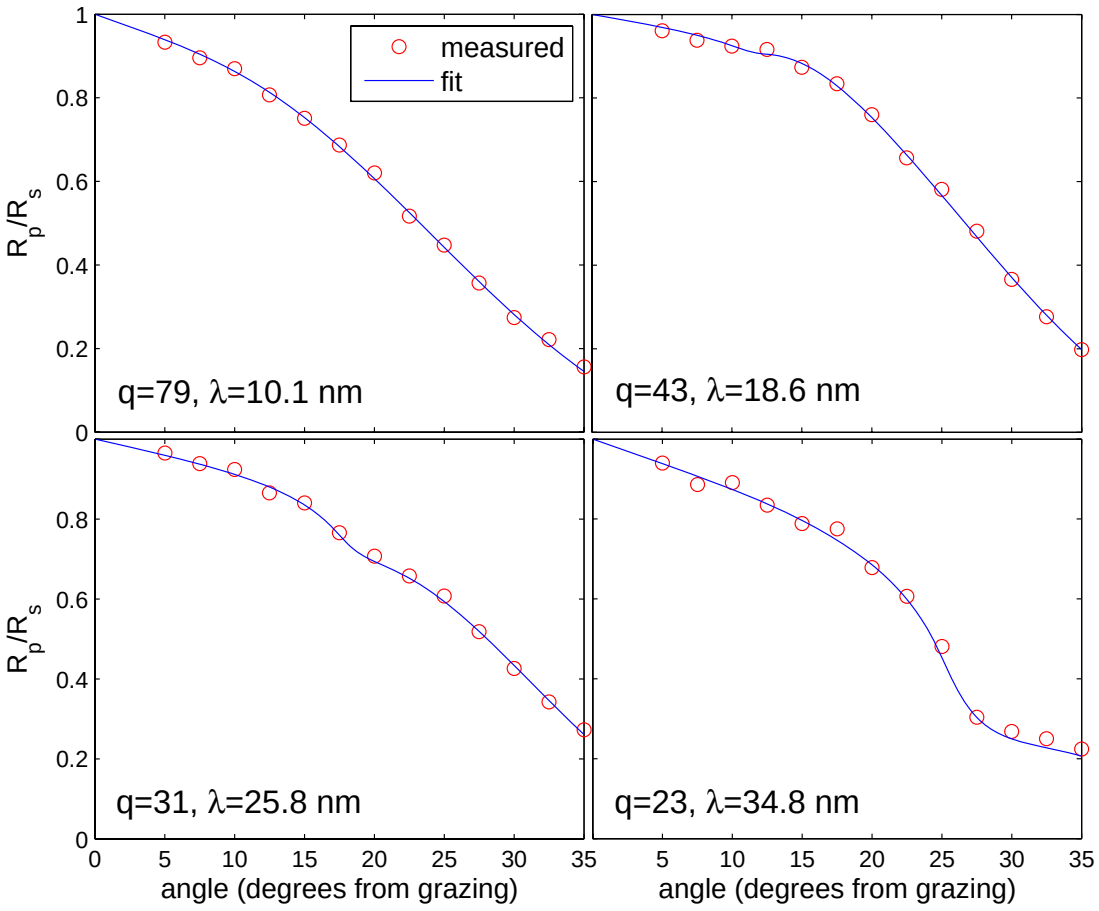

Figure 6.9 The measured ratio reflectance and fit of uranium at four representative wavelengths: 10.1 nm, 18.6 nm, 25.8 nm, and 34.8 nm.

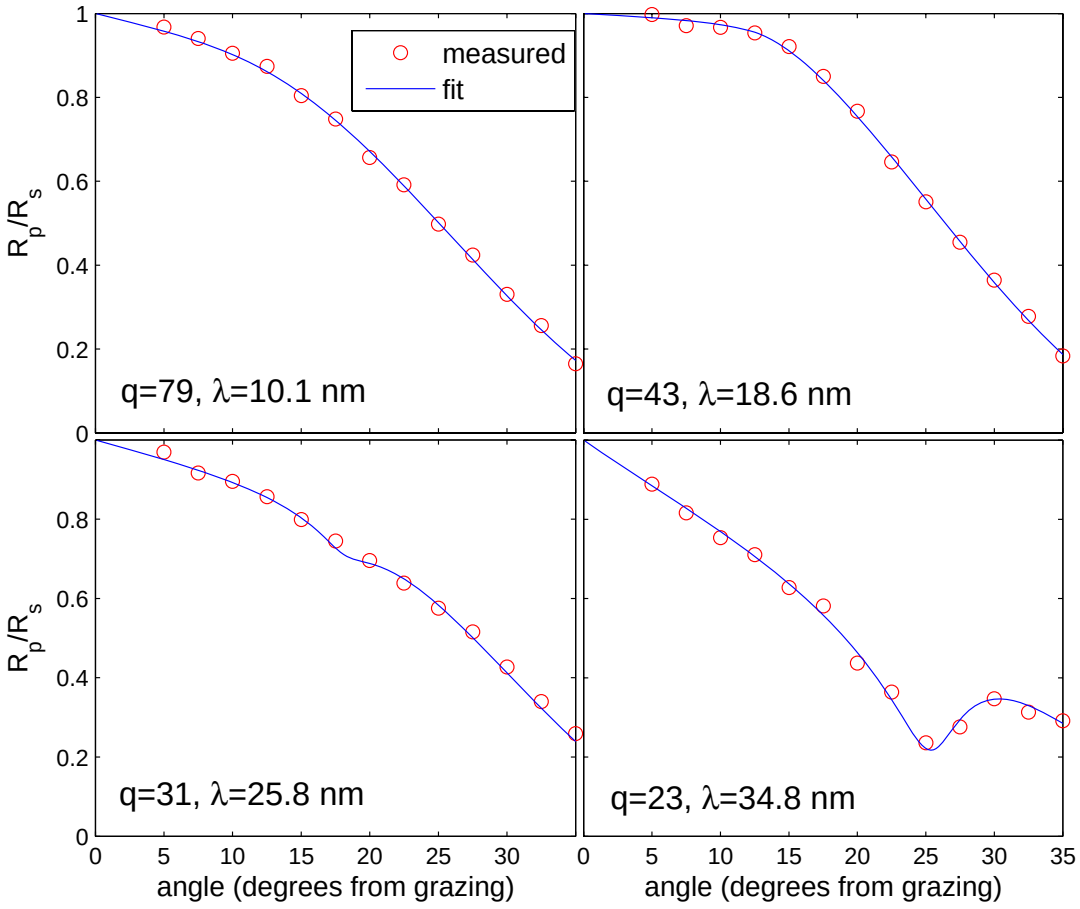

Figure 6.10 The measured ratio reflectance and fit of UO_x at four representative wavelengths: 10.1 nm, 18.6 nm, 25.8 nm, and 34.8 nm.

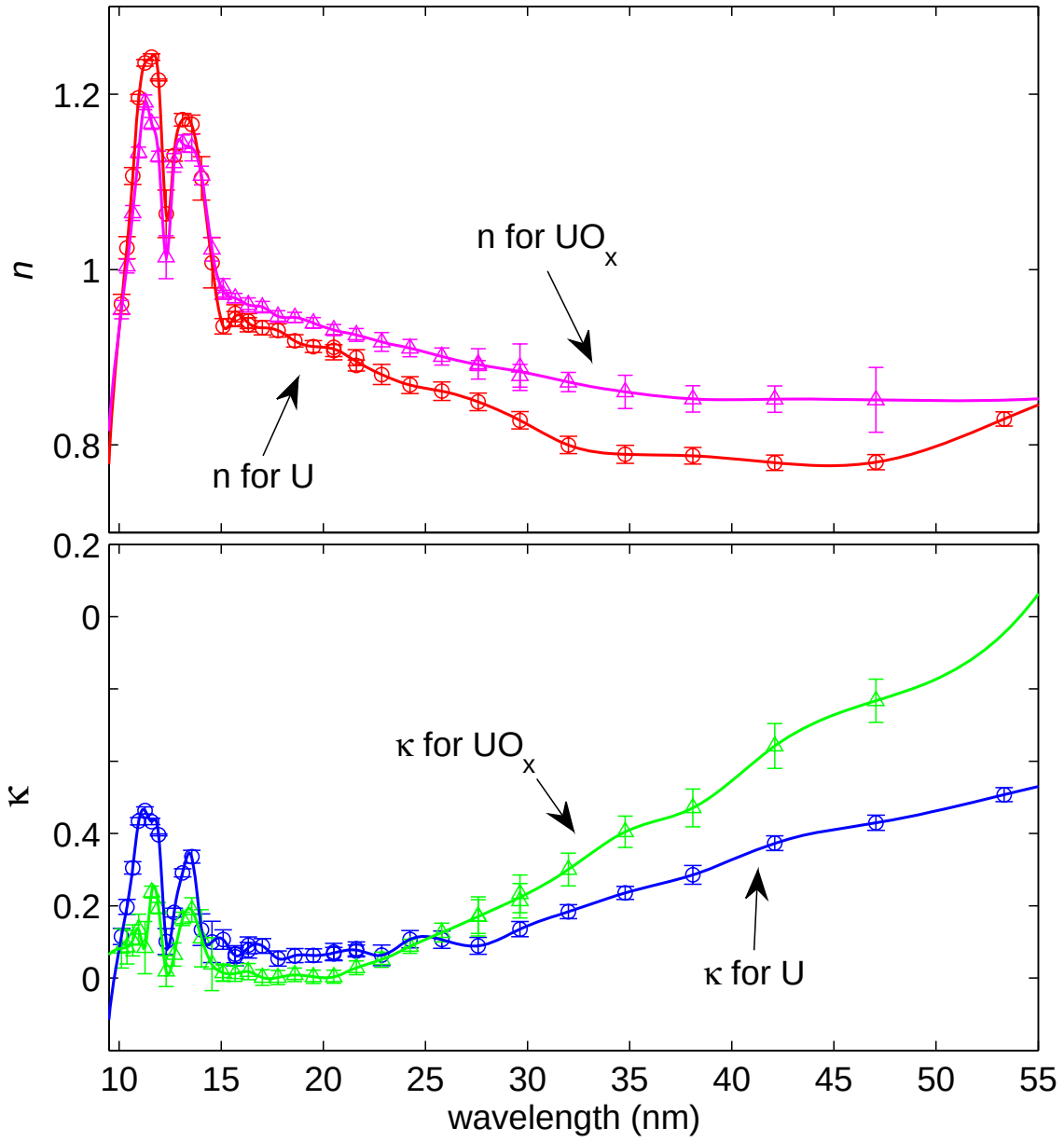

Figure 6.11 The optical constants of U and UO_x determined using the ratio reflectance technique. Statistical error bars are also shown.

wavelength (nm)	n **for U**	κ **for U**	n **for UO$_x$**	κ **for UO$_x$**
10.1	0.961	0.058	0.954	0.041
10.4	1.025	0.098	1.004	0.043
10.7	1.107	0.152	1.065	0.052
11.0	1.196	0.217	1.134	0.068
11.3	1.236	0.232	1.191	0.042
11.6	1.242	0.217	1.167	0.119
11.9	1.216	0.198	1.129	0.097
12.3	1.064	0.051	1.014	0.010
12.7	1.130	0.091	1.122	0.033
13.1	1.171	0.146	1.144	0.082
13.6	1.166	0.168	1.139	0.094
14.0	1.104	0.067	1.107	0.055
14.5	1.008	0.050	1.023	0.019
15.1	0.935	0.053	0.972	0.007
15.7	0.950	0.029	0.968	0.006
16.3	0.941	0.045	0.960	0.009
17.0	0.934	0.045	0.957	0.001
17.8	0.931	0.027	0.947	0.001
18.6	0.919	0.031	0.945	0.005
19.5	0.912	0.031	0.939	0.002
20.5	0.911	0.036	0.931	0.002
21.6	0.900	0.040	0.925	0.014
22.9	0.880	0.032	0.917	0.025
24.2	0.868	0.054	0.910	0.044
25.8	0.861	0.053	0.901	0.063
27.6	0.849	0.045	0.891	0.085
29.6	0.828	0.068	0.879	0.107
32.0	0.800	0.092	0.872	0.150
34.8	0.789	0.118	0.861	0.202
38.1	0.788	0.143	0.852	0.235
42.1	0.780	0.187	0.852	0.321
47.1	0.780	0.215	0.851	0.384

Table 6.2 Optical constants of U and UO$_x$.

Fig 6.12 shows measured optical constants for uranium and the extent of the curve change when statistical errors and errors due to uncertainty in film thickness are considered. Fig 6.13 shows a similar curve for naturally oxidized uranium. The overall error for values of both n and κ was about 0.02.

The optical constants of uranium were re-measured completely on a second day to show repeatability. The samples on the two days were different depositions and had different thicknesses. These two sets of data are shown in Figure 6.14. The data sets agree within our error bars.

To our knowledge, the optical constants of uranium (as opposed to uranium oxide) have never been measured in this wavelength range. As mentioned earlier in this chapter, Faldt and Nisson [92] measured the optical constants of evaporated uranium *in-situ* from 50 to 2000 nm. At shorter wavelengths, Cukier et al. [93] measured the photoabsorption cross section of uranium from 2.7-9.5 nm, preventing absorption using an aluminum capping layer. Lunt [53] studied the optical properties of UO_2 in the range 5-17 nm, and at 30.4 nm, 53.7 nm, and 58.4 nm. Figure 6.15 plots κ for uranium and UO_x along with κ for U measured by Faldt and Cukier and κ for UO_2 measured by Lunt. Error bars on our data include statistical errors as well as errors due to uncertainty in film thickness. This plot shows that our data for uranium matches data taken *in-situ* by Faldt and data using a capping layer taken by Cukier. Also, our data for UO_x matches data taken by Lunt of UO_2.

6.8 Comparison with Atomic Scattering Factor Calculations

The Center for X-ray Optics (CXRO) has a website [91] where optical constants can be looked up for many materials in the wavelength range from 0.01 nm to 40 nm.

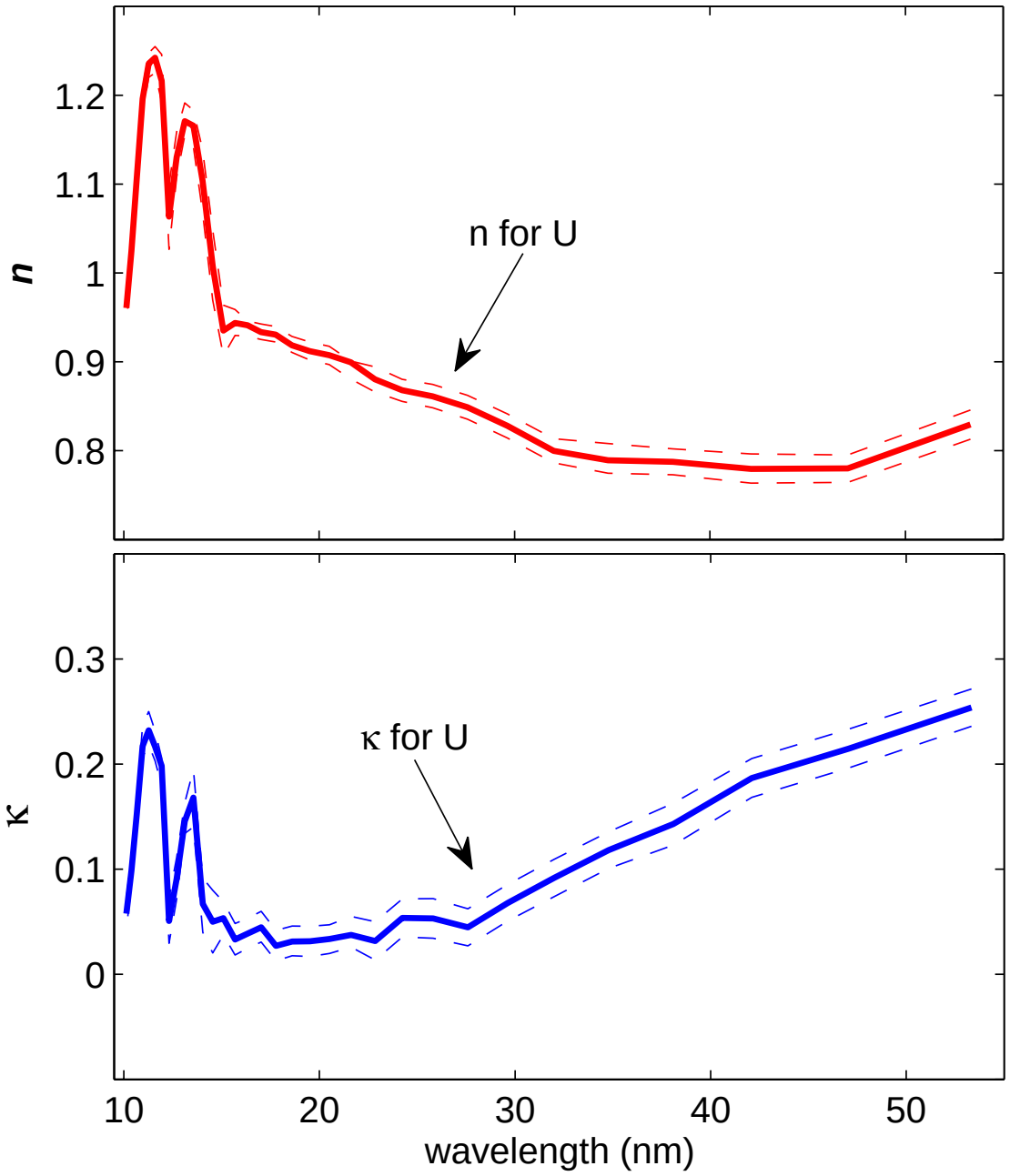

Figure 6.12 Solid curves show the optical constants of uranium. Dashed curves show the extent of the change when statistical errors and errors due to uncertainty in thickness are included.

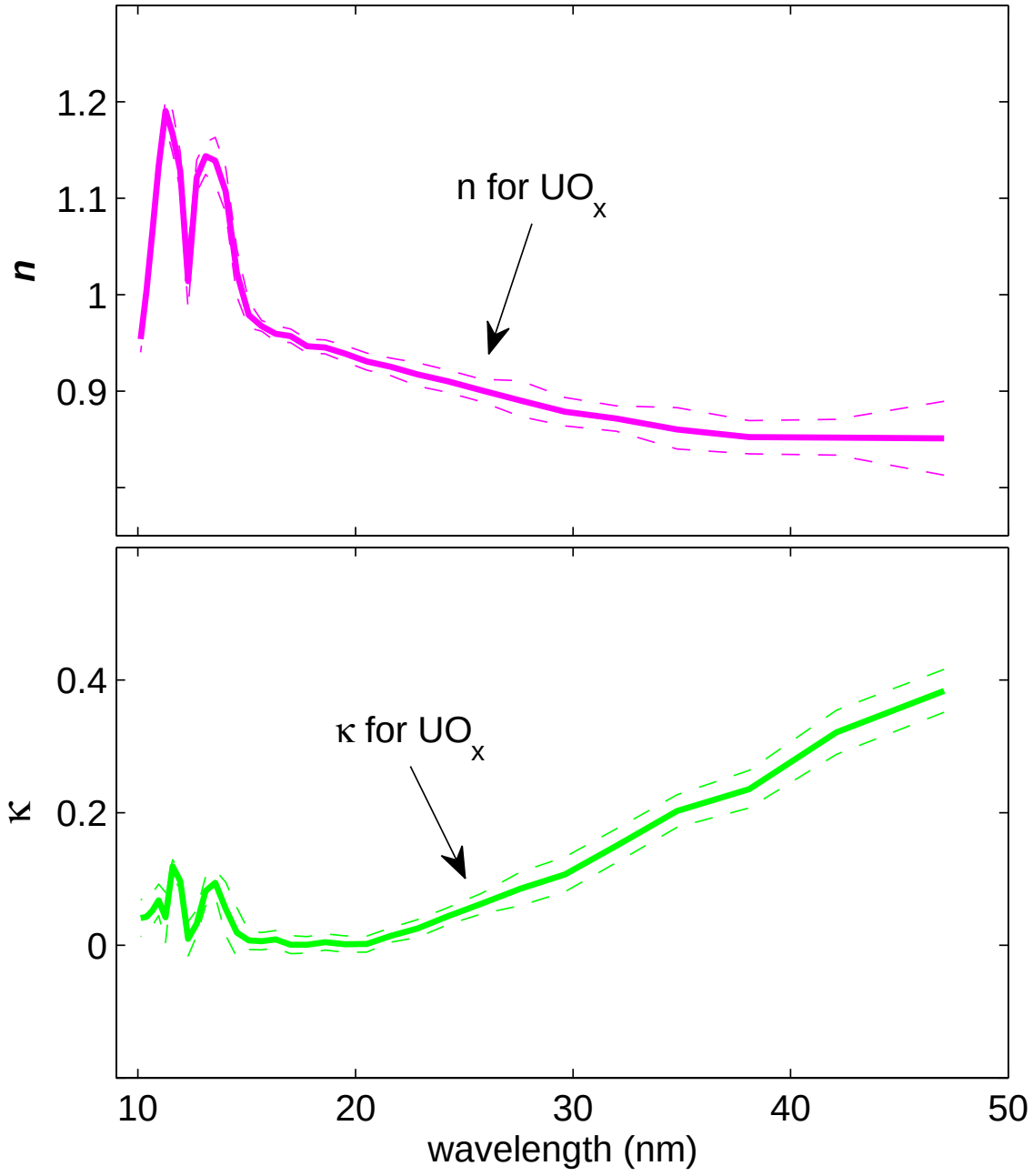

Figure 6.13 Solid curves show the optical constants of UO_x. Dashed curves show the extent of the change when statistical errors and errors due to uncertainty in thickness are included.

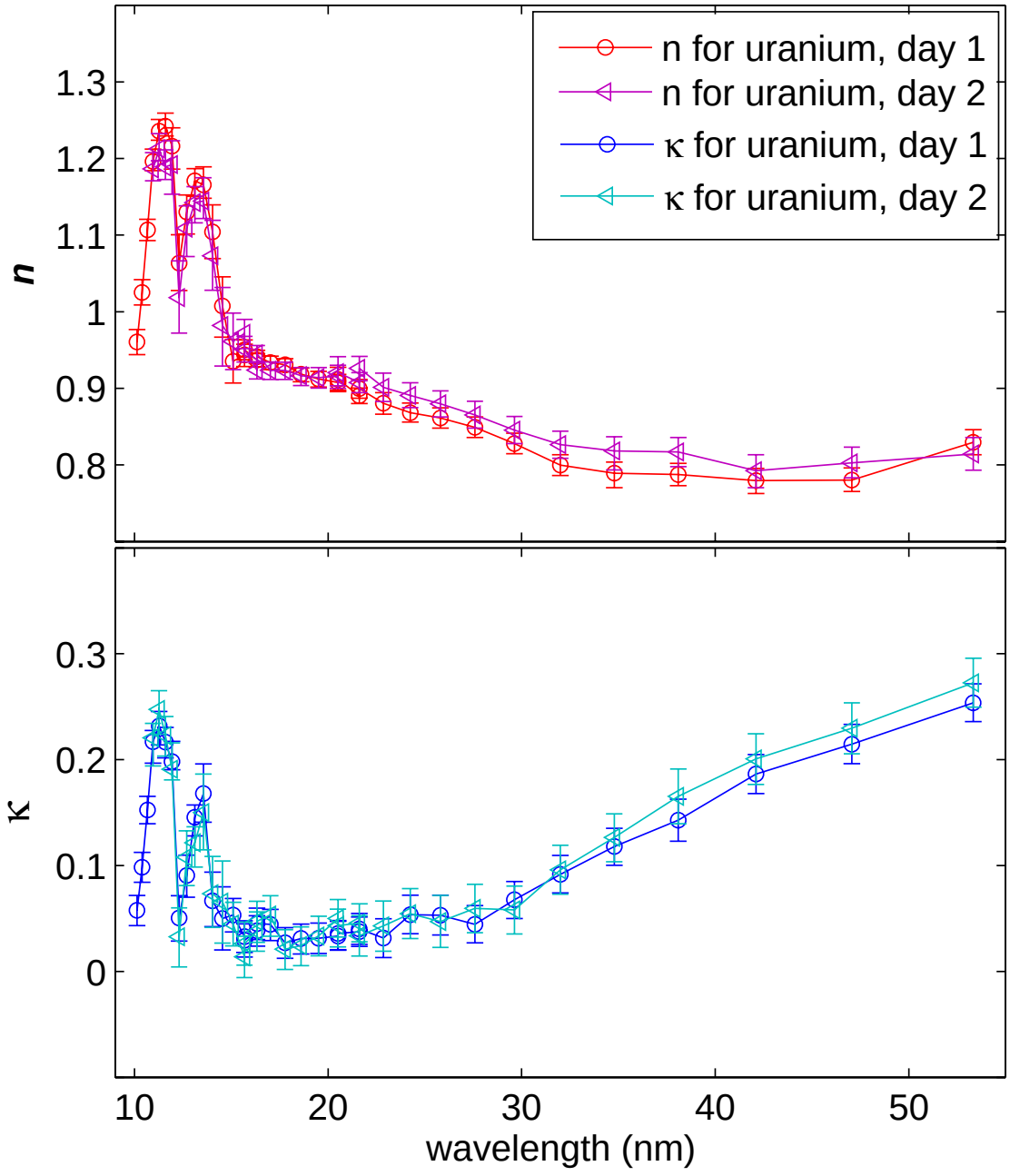

Figure 6.14 The optical constants of uranium measured on two separate days to show repeatability. The data sets agree within error bars.

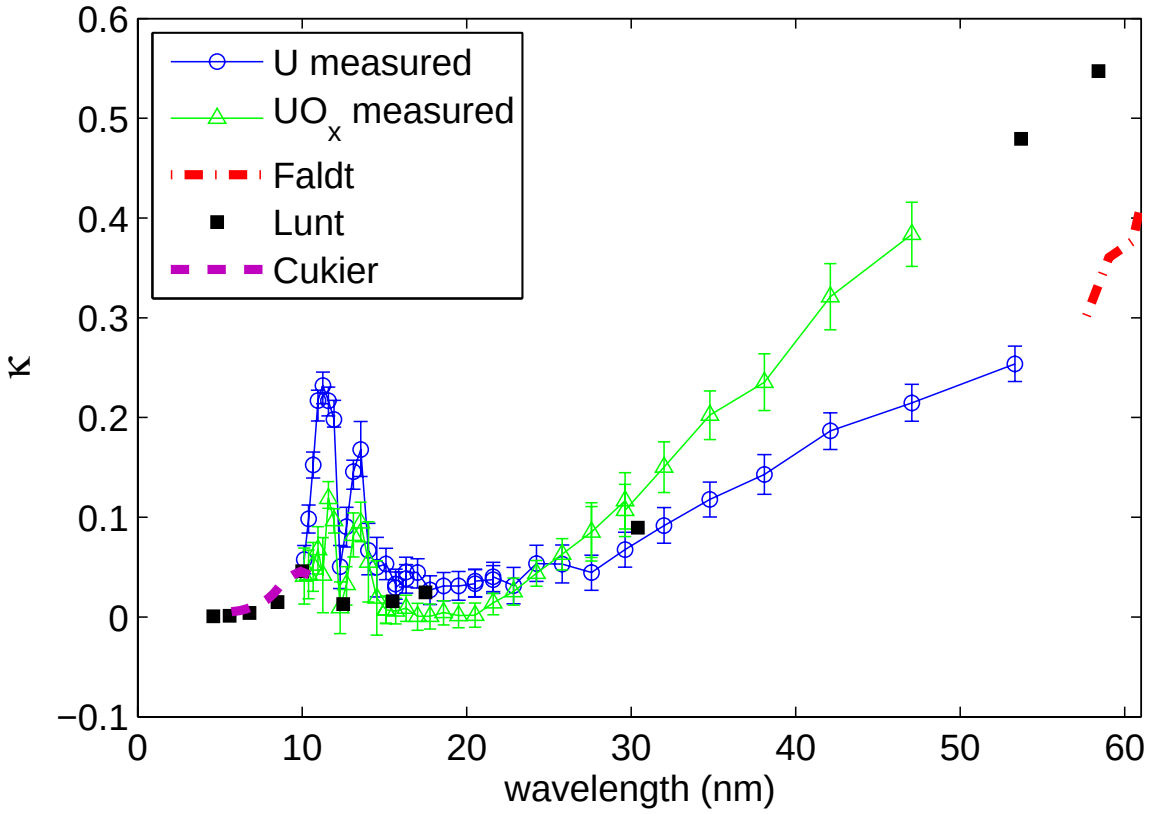

Figure 6.15 Measured κ of uranium and oxidized uranium compared with κ for uranium measured by Faldt [92] and Cukier [93] and κ for UO_2 measured by Lunt [53]. Our κ for uranium matches that of Faldt (measured *in-situ*) and Cukier (measured with an aluminum capping layer). Our κ for oxidized uranium matches κ for UO_2 measured by Lunt.

These optical constants are calculated using atomic scattering factors from the tables compiled in 1993 by Henke et al. in reference [60]. In the extreme ultraviolet wavelength range, the primary interactions of light with matter are photoabsorption and coherent scattering. At the atomic level, atomic scattering factors describe these processes. The atomic scattering factor, $f = f_1 + if_2$, is defined as the ratio of the amplitudes of electromagnetic radiation scattered by a particular atom to that of a single free electron. Henke and coworkers compiled photoabsorption cross sections for 92 elements from available experimental data and theoretical calculations. These data were used along with modified Kramers-Kronig dispersion relations to calculate the atomic scattering factors for the elements.

For condensed matter, atomic scattering factors may be used to describe interaction with EUV photons if we assume that the individual atoms scatter independently, that is, unaffected by the chemical state of the system. It is shown in reference [60] that this is a good assumption for wavelengths shorter than about 24 nm and sufficiently far from absorption edges. At longer wavelengths, however, the specific chemical state is important, and experimental measurements must be made. In the atomic description, the total coherently scattered amplitude is simply the vector sum of the amplitudes scattered by the individual atoms.

The index of refraction, $N = n + i\kappa$, of a material can be determined from the atomic scattering factors by assuming that individual atoms scatter as dipoles. This assumption is good when the wavelength of light is long compared with atomic dimensions. The index of refraction can be written as

$$N = n + i\kappa = 1 - \frac{r_0}{2\pi}\lambda^2 N_v(f_1 + if_2) \tag{6.1}$$

where r_0 is the classical electron radius, λ is the wavelength, and N_v is the number of atoms per unit volume.

Previous to this work, these calculations based on atomic scattering factors were the only optical constants for uranium available in this region. Figure 6.16 plots our measured n and κ for uranium along with n and κ for uranium tabulated on the CXRO website. As mentioned previously, atomic scattering factors are only applicable far from absorption thresholds and at wavelengths shorter than 24 nm. Much of our data is taken at wavelengths longer than 24 nm, and wavelengths shorter than 24 nm are near an absorption edge ($\sim$11 nm). Therefore, we do not expect these calculations to match our data very well, which they do not. However, they do confirm the general trend of our data. Something interesting to note is that the absorption peaks in our measured data are shifted about 0.5 nm to longer wavelengths (lower energy) compared to those based on atomic scattering factor calculations. Professor Allred and Turley's group previously observed this same trend in the measured constants of thorium and thorium dioxide [55, 97]. These shifts may be due to chemical bonding effects disregarded by atomic scattering factor calculations.

6.9 Conclusions

We have shown that high harmonics provide a good source of extreme ultraviolet radiation sufficient to do polarimetry measurements and extract material optical constants in the wavelength range from 10 nm to 42 nm. We have used laser-generated high harmonics here for the first time in a workhorse setting to make measurements valuable to the field of EUV optics. We have found that the relative noisiness of our harmonic source can be checked by using the unique polarization properties of the harmonics to reduce systematic errors significantly. We have found that optical constants can be extracted from these polarization ratio reflectance measurements, and we have done so to find the optical constants of copper, uranium, and their natural

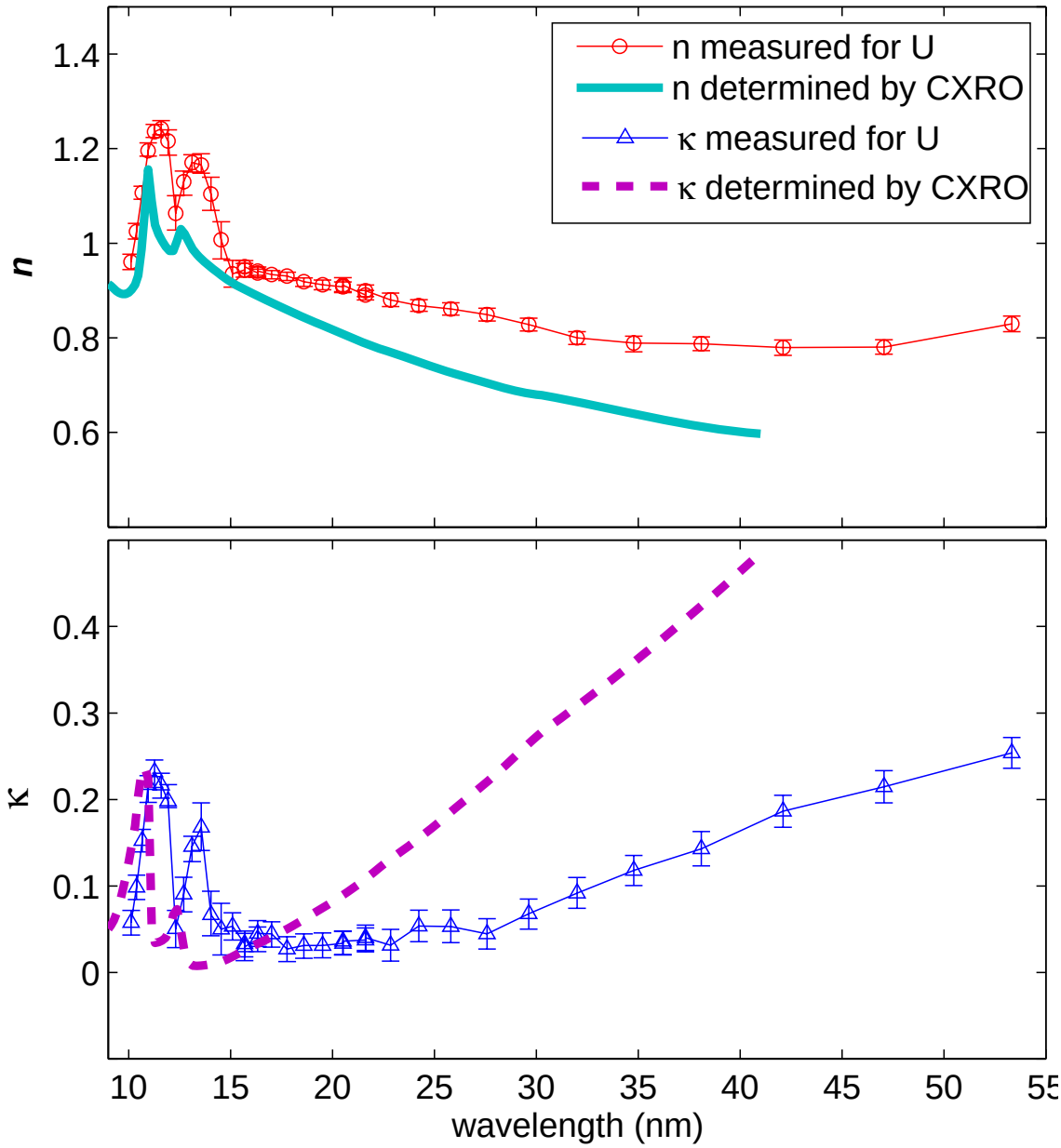

Figure 6.16 Measured optical constants of uranium compared with constants calculated using the atomic scattering factors [60]. Calculated data does not match our data very well, most likely because calculated data is not accurate near absorption edges (here ∼11 nm) or at wavelengths longer than 24 nm. Interestingly, measured absorption peaks are shifted about 0.5 nm to longer wavelengths compared to calculated data.

oxides through this wavelength range.

Appendix A

Standard Operating Procedures

A.1 Aligning the Polarimeter Positioning System

1. Align the infrared laser through the polarimeter using the apertures.
2. Block the infrared laser, and align the HeNe laser through the harmonic-generation chamber and into the polarimeter with the same apertures used to align the infrared laser.
3. Open the program on the computer called 'APT User.' It can be found on the desktop. Load the correct settings by going to File, then Load, then clicking on 'standard'.
4. Move the sample into the beam, and move the sample angle to 90°.
5. Adjust the sample rotation stage until the HeNe beam is retro-reflecting onto the aperture inside the polarimeter chamber. Use the knobs on the back of the sample holder to make fine adjustments.
6. Block the HeNe beam going into the polarimeter through the harmonic-generation chamber.

7. Align the HeNe beam going into the polarimeter through the window in the side port by flipping the switch labeled 'HeNe mirror' to insert the removable mirror into the beam path. Adjust an upstream mirror until the beam is aligned to the aperture inside the polarimeter, then adjust the removable mirror until the beam is retro-reflecting from the sample onto the same mirror.

8. Using the sample translation stage, move the sample out of the beam.

9. Use the detector rotation stage to center the HeNe spot on the grating. Adjust the CCD camera looking at the grating surface until the HeNe spot is clearly visible on the TV screen. Mark the location of the HeNe spot on the TV screen with a marker.

10. Move the grating rotation until the HeNe spot is visible on the TV screen for the camera looking at the microchannel plate. Mark the location of the HeNe spot on the TV screen with a marker.

11. Move the sample into the beam and adjust the sample rotation until the HeNe is again retro-reflecting onto the aperture inside the polarimeter.

12. Move the sample angle to 0° and adjust the micrometer on the sample holder until the sample is cutting off half of the HeNe beam.

13. Move the sample angle to 90° and move the sample out of the beam.

A.2 Making a Reflectance Measurement

1. After aligning the positioning system, place a gas cell in the harmonic-generation chamber and pump the system down. The secondary vacuum chamber needs to be at pressures below 10^{-6}.

2. Close the knob pumping out the semi-infinite gas cell region, and fill the region with the desired amount of gas. Typical pressures are 80 torr of helium, 55 torr of neon, and 12 torr of argon.

3. Close the gate valve, and unblock the infrared laser to allow it to drill the foil.

4. When the foil has been drilled, open the gate valve and check to make sure the pressure in the secondary vacuum chamber is still low.

5. Turn on the microchannel plate detector by flipping two switches marked '1/2A-SB,' waiting 30 seconds, then flipping two switches marked '3/4A-SB.'

6. Open the program on the computer 'ImageCaptureBrimhall.vi.' A shortcut can be found on the desktop.

7. Click the LabView 'run' button on the top left corner of the screen.

8. Block the beam and click the black 'Ultracal' button to do a background subtraction.

9. Click the green 'Run' button to start running the camera.

10. Move the grating rotation and adjust the gas pressure, aperture, and MCP plate voltage until you see harmonics on the screen. Optimize the harmonics with these same parameters.

11. Make sure that the waveplate is in the beam.

12. Set the acceptable laser-energy range with the controls called 'Laser Min' and 'Laser Max.' The readouts of 'Actual Max,' 'Avg Max,' and 'Standard Deviation' are there to help you set a good range. The green light entitled 'Laser

Energy in Range?' will give you a visible estimate of how many shots are making it in the range.

13. When you are satisfied with your laser-energy range, take a measurement of harmonics by setting the number in the control entitled '# of shots to average' and clicking the blue button called 'Average.' When the number in the box 'Repetitions' equals the number of shots to average, your harmonic image will appear on the screen. Click the green 'Run' button to stop the camera, then click 'Save' to save your data.

14. Move your sample, detector, polarization, and other motors around and collect your desired data.

A.3 Computer Programs

Two computer programs run the necessary equipment to operate the polarimeter. The first is called 'APTUser' and can be found on the desktop of the polarimeter computer. This program operates the seven motors used in the polarimeter positioning system. The second is called 'ImageCaptureBrimhall.vi' and a shortcut can also be found on the desktop of the polarimeter computer. This program operates the image capture system used to record harmonic data. These programs, which run the polarimeter, are described in the following two sections.

A.3.1 APTUser

When opening APTUser, four sub-screens should appear. These four screens are connected to the four drivers used to operate the seven motors of the polarimeter positioning system. If the four screens do not come up, the drivers are probably not

on or not connected to the computer. On each of the four screens you will see a serial number that corresponds to the serial number of the motor drivers. This tells you which screen operates which driver. Each driver operates two motors. Thus each of the four screens operates two motors. The top left screen operates the waveplate rotation and the second port is blank. The top right screen operates the linear focusing of the MCP (left) and the linear translation of the sample (right). The bottom left screen operates the detector rotation (left) and the sample rotation (right). The bottom right screen operates the MCP rotation (left) and the grating rotation. You can move a motor by clicking on the red numbers and typing in the place you want it to go.

You can adjust the settings for a particular motor by flipping the 'Channel' toggle switch to the motor you want to adjust, then clicking the 'Settings' button on the bottom right of the screen. You can also save your settings under a profile name. A profile that works for polarimetry measurements (set up by me) is called 'standard.' This profile should come up automatically when opening the program, but if it doesn't, you can load it by going to File, then Load, and clicking on the profile called 'standard.'

A.3.2 ImageCaptureBrimhall.vi

ImageCaptureBrimhall.vi is a program I wrote in LabView that allows you to save images harmonic images. The image capture is triggered by the avalanche photodiode in the oscillator, so if the oscillator isn't modelocked or the trigger isn't connected, the program will not run.

The front panel can be seen in Figure A.1. The screen titled 'Intensity Graph' is the main screen that images the microchannel plate. The two graphs immediately below and to the left of this screen show lineouts of the screen at the locations

specified by the yellow crosshairs. The indicators immediately below this screen give information about the image on the screen, such as the maximum and minimum intensity values.

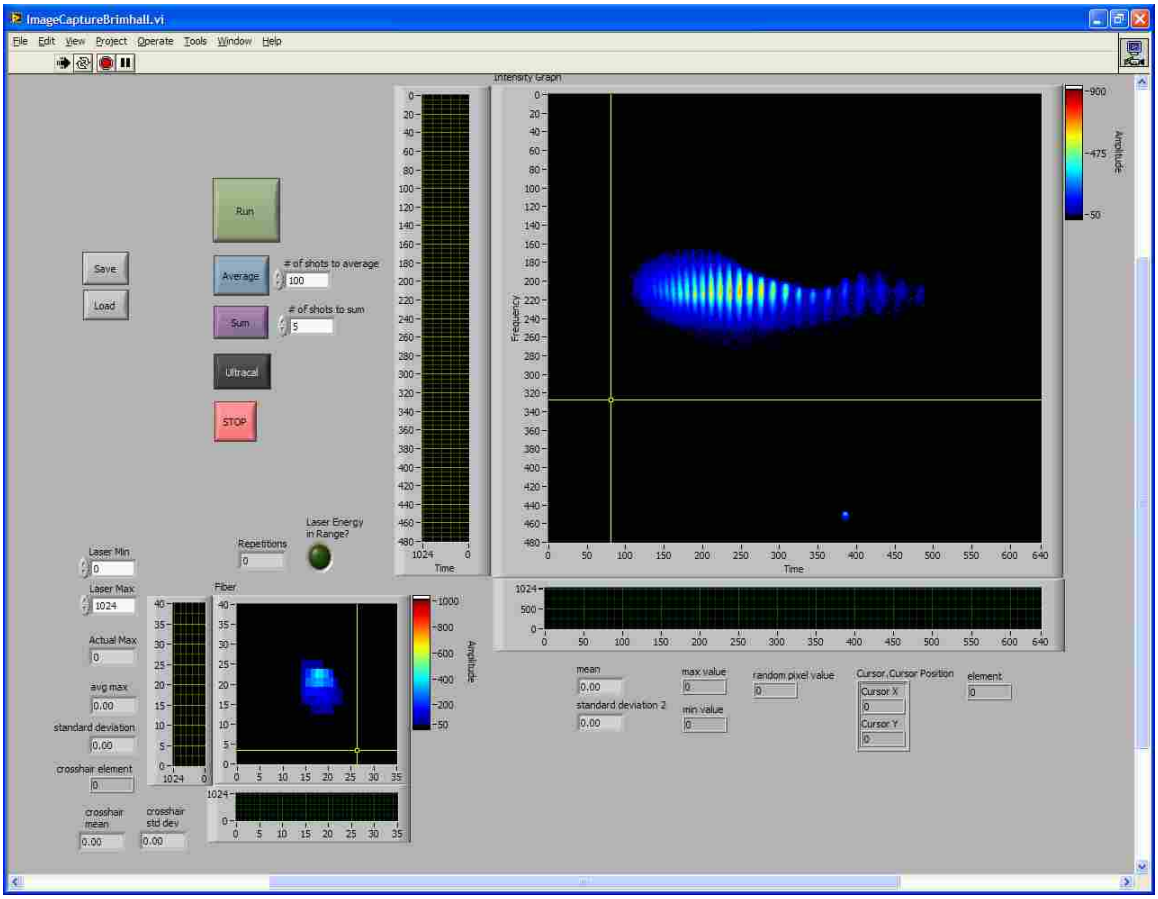

Figure A.1 ImageCaptureBrimhall.vi front panel

The smaller screen to the left of the main screen, entitled 'Fiber' is a subset of the main screen that shows only the fiber location. The program uses the pixels within this screen to determine whether the laser is within the range specified by the controls 'Laser Min' and 'Laser Max.' The indicators below these two controls are meant to help the user specify this laser energy range. The 'avg max' indicator resets every time the run button is pressed. Thus, letting the program run for a minute or so gives a more accurate average than letting it run for only a few seconds. The 'standard

deviation' indicator tells you how jumpy the laser is. If this is very large, it might be wise to make some adjustments to the laser to make it more stable. The green light called 'Laser Energy in Range?' gives a visual estimate of how good your specified range is. Typically you want to capture at least one out of every three or four shots, so you aren't waiting a long time to complete a measurement. On a good laser run, you might capture almost every shot.

The buttons to the left of the main screen control the image capture. The black 'Ultracal' button does a background subtraction, and the 'Run' button is ineffective until this button is pressed. The 'Run' button starts the camera, which continues running until the 'Run' button is pressed again. The average button averages together the number of shots specified by the control called '# of shots to average' where the laser energy is within the range specified by the controls called 'Laser Min' and 'Laser Max.' The indicator titled 'Repetitions' tells you how many shots the computer has captured where the laser energy is within the specified range. When the number indicated in 'Repetitions' matches the number of shots to average, the main screen shows the averaged image.

The 'Sum' button does not work, and I haven't wanted to use it enough to fix it. In principle, the sum button just needs the same programming as the average button (which works), without dividing by the number of frames at the end.

The 'Save' button is only effective when the 'Run' button is not pressed. The save command saves the image on the main screen in matrix form. This makes it easy to read into MatLab for later analysis. Please note: the image on the main screen is the only thing that will be saved. Individual shots that comprise the averaged image, the number of shots averaged, and the user-specified laser energy range are examples of data that are not saved. The 'Load' button will plot on the main screen an image that was previously saved with this same program. Again, the load button cannot recover

data that is not previously saved, such as the user-specified laser energy range.

The block diagram is shown in Figure A.2. Most of the programming tells the card when to capture images. All of the IMAQ sub-VIs are sub-VIs that came with the capture card, and most of the programming came from their examples. For example, 'IMAQ Init.vi' loads a configuration file and configures the camera. The actual image comes from 'IMAQ Extract Buffer.vi.' I convert the image into an array using 'IMAQImageToArray.' I then plot this array in the main screen (after subtracting the ultracal image).

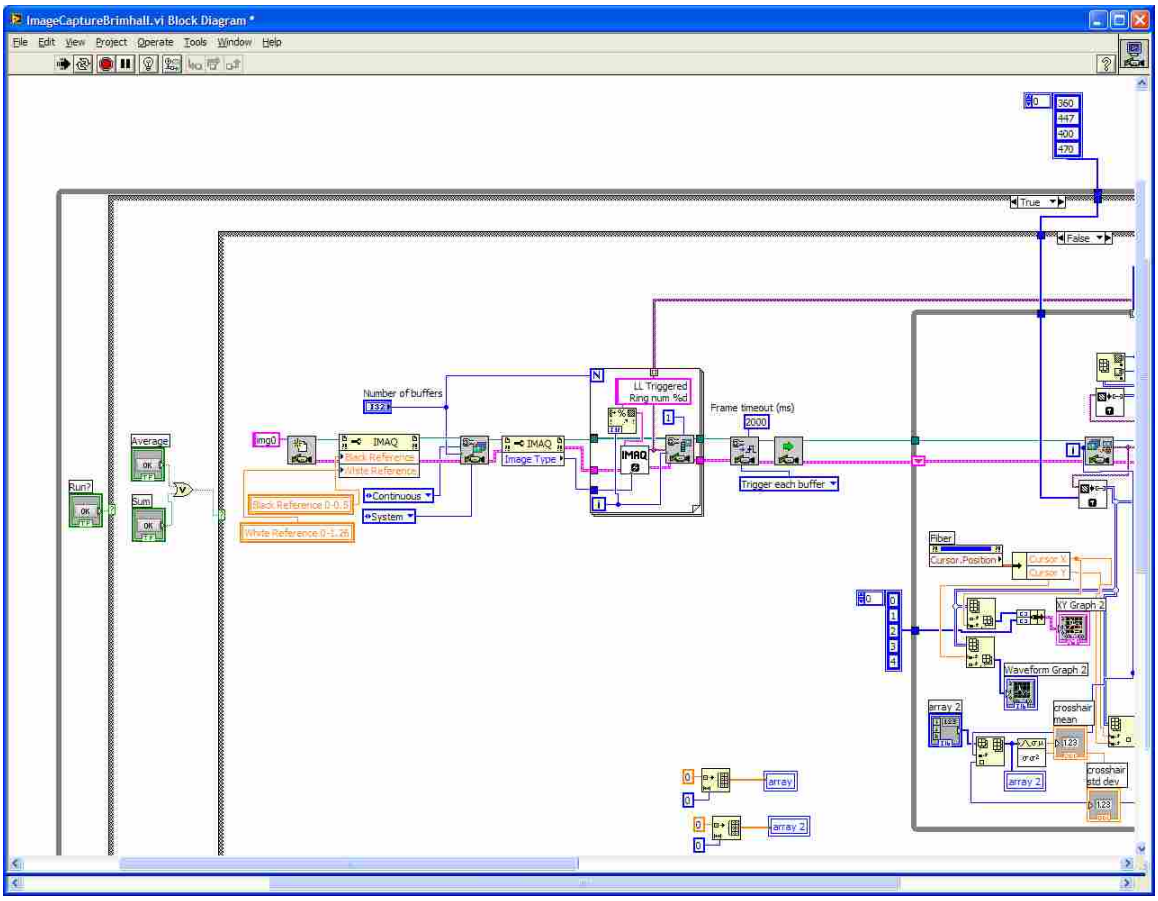

Figure A.2 ImageCaptureBrimhall.vi block diagram

I also cut a piece of this array out to plot in the 'Fiber' screen. The control to specify this piece is on the very top of the block diagram, outside of all of the loops.

This control is made up of four pixel numbers: left, top, right, and bottom. If one can see the fiber spot on the main screen, but not on the fiber screen, one needs to change these numbers until you can see it again.

Bibliography

[1] P. Franken, P. Hill, C. Peters, and G. Weinreich, "Generation of optical harmonics," Phys. Rev. Lett. **7,** 118 (1961).

[2] A. McPherson, G. Gibson, H. Jara, U. Johann, T. S. Luk, I. A. McIntyre, K. Boyer, and C. K. Rhodes, "Studies of multiphoton production of vacuum ultraviolet radiation in the rare gases," J. Opt. Soc. Am B **4,** 595–601 (1987).

[3] M. Ferray, A. L'Huillier, X. F. Li, L. A. Lomprk, G. Mainfray, and C. Manus, "Multiple-harmonic conversion of 1064 nm radiation in rare gases," J. Phys. B **21,** L31–L35 (1988).

[4] A. L'Huillier and P. Balcou, "High-order harmonic generation in rare gases with a 1-ps 1053-nm laser," Phys. Rev. Lett. **70,** 774–777 (1993).

[5] A. Rundquist, C. Durfee, Z. Chang, C. Herne, S. Backus, M. M., and H. Kapteyn, "Phase-matched generation of coherent soft x-rays," Science **280,** 1412–1415 (1998).

[6] E. Takahashi, Y. Nabekawa, T. Otsuka, M. Obara, and K. Midorikawa, "Generation of highly coherent submicrojoule soft x-rays by high-order harmonics," Phys. Rev. A **66,** 1–4 (2002).

[7] J. Zhou, J. Peatross, M. M. Murnane, H. C. Kapteyn, and I. P. Christov, "Enhanced High-Harmonic Generation Using 25 fs Laser Pulses," Phys. Rev. Lett. **76,** 752–755 (1996).

[8] C. Spielmann, N. H. Burnett, S. Sartania, R. Koppitsch, M. Schnrer, C. Kan, M. Lenzner, P. Wobrauschek, and F. Krausz, "Generation of Coherent X-rays in the Water Window Using 5-Femtosecond Laser Pulses," Science **278,** 661–664 (1997).

[9] P. Milonni and J. Eberly, *Lasers* (Wiley, New York, 1988).

[10] T. Ditmire, E. T. Gumbrell, R. A. Smith, J. W. G. Tisch, D. D. Meyerhofer, and M. H. R. Hutchinson, "Spatial Coherence Measurement of Soft X-Ray Radiation Produced by High Order Harmonic Generation," Phys. Rev. Lett. **77,** 4756 – 4759 (1996).

[11] R. A. Bartels, A. Paul, H. Green, H. C. Kapteyn, M. M. Murnane, S. Backus, I. P. Christov, Y. Liu, D. Attwood, and C. Jacobsen, "Generation of Spatially Coherent Light at Extreme Ultraviolet Wavelengths," Science **297,** 376–378 (2002).

[12] G. Farkas and C. Toth, "Proposal for attosecond light pulse generation using laser induced multiple-harmonic conversion processes in rare gases," Physics Letters A **168,** 447–450 (1992).

[13] T. Brabec and F. Krausz, "Intense few cycle light pulses: frontiers of nonlinear optics," Rev. Mod. Phys. **72,** 545591 (2000).

[14] D. Schulze, M. Dorr, G. Sommerer, J. Ludwig, P. Nickles, T. Schlegel, W. Sandner, M. Drescher, U. Kleineberg, and U. Heinzmann, "Polarization of the 61st Harmonic from 1053-nm Laser Irradiation in Neon," Phys. Rev. A **57,** 3003 (1998).

[15] P. Dietrich, N. H. Burnett, M. Ivanov, and P. B. Corkum, "High-harmonic generation and correlated two-electron multiphoton ionization with elliptically polarized light," Phys. Rev. A **50,** R3585 – R3588 (1994).

[16] J. Krause, K. Schafer, and K. Kulander, "High-order harmonic generation from atoms and ions in the high intensity regime," Phys. Rev. Lett. **68,** 3535 (1992).

[17] P. Corkum, "Plasma perspective on strong-field multiphoton ionization," Phys. Rev. Lett. **71,** 1994 (1993).

[18] E. Constant, D. Garzella, P. Breger, E. Mevel, C. Dorrer, C. L. Blanc, F. Salin, and P. Agostini, "Optimizing High Harmonic Generation in Absorbing Gases: Model and Experiment," Phys. Rev. Lett. **82,** 1668 – 1671 (1999).

[19] Y. Tamaki, J. Itatani, Y. Nagata, M. Obara, and K. Midorikawa, "Highly efficient phase-matched high-order harmonic generation in self guided laser beam," Phys. Rev. Lett. **82,** 1422–1425 (1999).

[20] C. Durfee, A. Rundquist, S. Backus, C. Herne, M. Murnane, and H. Kapteyn, "Phase matching of high-order harmonics in hollow waveguides," Phys. Rev. Lett. **83,** 2187–2190 (1999).

[21] A. Rundquist, C. G. Durfee, Z. Chang, C. Herne, S. Backus, M. M. Murnane, and H. C. Kapteyn, "Phase-matched generation of coherent soft x-rays," Science 280 (1998).

[22] L. G. Gouy, "Sur une propriete nouvelle des ondes lumineuses," Compt. Rendue Acad. Sci. Paris **110,** 1251 (1890).

[23] J. Peatross and D. Meyerhofer, "Intensity-dependent phase effects in high order harmonic generation," Phys. Rev. A **52,** 3976 (1995).

[24] P. Salieres, A. L'Huillier, and M. Lewenstein, "Coherence control of high-order harmonics," Phys. Rev. Lett. **74,** 3776 (1995).

[25] C. Altucci, T. Starczewski, E. Mevel, C. G. Wahlstrom, B. Carre, and A. L'Huillier, "Influence of atomic density in high-order harmonic generation," J. Opt. Soc. Am. B **13,** 148 (1996).

[26] A. Braun, G. Korn, X. Liu, D. Du, J. Squier, and G. Mourou, "Self-channeling of high-peak-power femtosecond laser pulses in air," Opt. Lett. **20,** 73 (1995).

[27] A. L'Huillier, P. Balcou, S. Candel, K. J. Schafer, and K. C. Kulander, "Calculations of High-Order Harmonic-Generation Processes in Xenon at 1064nm," Phys. Rev. A **46,** 2778 (1992).

[28] J.F.Hergott, M. Kovacev, H. Merdji, C. Hubert, Y. Mairesse, E. Jean, and P. Breger, "Extreme ultraviolet high-order harmonic pulses in the microjoule range," Phys. Rev. A **66,** 021801(R) (2002).

[29] H. Milchberg, C. Durfee, and T. McIlrath, "High-order frequency conversion in the plasma waveguide," Phys. Rev. Lett. **75,** 2494–2497 (1995).

[30] Y. Tamaki, Y. Nagata, M. Obara, and K. Midorikawa, "Phase-matched high order harmonic generation in a gas-filled hollow fiber," Phys. Rev. A **59,** 4041–4044 (1999).

[31] S. Voronov, I. Kohl, J. Madsen, N. Terry, J. Titensor, Q. Wang, and J. Peatross, "Control of Laser High Harmonic Generation with Counter-Propagating Light," Phys. Rev. Lett. **87,** 133902 (2001).

[32] J. Sutherland, "Phase-matching optimization of laser high-order harmonics generated in a gas cell," Master's Thesis (Brigham Young University, Provo, UT, 2005).

[33] V. Tosa, E. Takahashi, Y. Nabekawa, and K. Midorikawa, "Generation of high-order harmonics in a self-guided beam," Phys. Rev. A **67,** 1–4 (2003).

[34] M. Ivanov and P. B. Corkum, "Routes to Control of Intense-Field Atomic Polarizability," Phys. Rev. Lett. **74,** 2933–2936 (1995).

[35] M. Nisoli and G. Sansone, "New frontiers in attosecond science," Progress in Quantum Electronics **33,** 1759 (2009).

[36] E. Goulielmakis *et al.*, "Direct Measurement of Light Waves," Science **305,** 1267–1269 (2004).

[37] A. C. Kak and M. Slaney, *Principles of Computerized Tomographic Imaging* (Society for Industrial and Applied Mathematics, New York, 2001).

[38] J. Itatani, J. Levesque, D. Zeidler, H. Niikura, H. Pepin, J. C. Kieffer, P. B. Corkum, and D. M. Villeneuve, "Tomographic imaging of molecular orbitals," Nature **432,** 867 (2004).

[39] W. Chao, B. D. Harteneck, J. A. Liddle, E. H. Anderson, and D. T. Attwood, "Soft X-ray microscopy at a spatial resolution better than 15 nm," Nature **435,** 1210–1213 (2005).

[40] W. Meyer-Ilse, D. Hamamoto, A. Nair, S. Lelievre, G. Denbeaux, L. J. A. L. Pearson, D. Yager, M. A. Legros, and C. A. Larabell, "High resolution protein localization using soft x-ray microscopy," J. Microsc. **201,** 395403 (2001).

[41] C. A. Larabell and M. A. L. Gros, "X-ray tomography generates 3-D reconstructions of the yeast, Saccharomyces cerevisiae, at 60-nm resolution," Mol. Biol. Cell **15,** 957962 (2003).

[42] P. Fischer, G. Schutz, G. Schmahl, P. Guttmann, and D. Raasch, "Imaging of magnetic domains with the X-ray microscope at BESSY using X-ray magnetic circular dichroism," Z. Phys. B **101,** 313316 (1996).

[43] G. Schneider, M. A. Meyer, G. Denbeaux, E. Anderson, B. Bates, A. Pearson, C. Knochel, D. Hambach, E. A. Stach, and E. Zschech, "Electromigration in passivated Cu interconnects studied by transmission x-ray microscopy," J. Vac. Sci. Technol. B **20,** 30893094 (2002).

[44] R. L. Sandberg, A. Paul, D. A. Raymondson, S. Hadrich, D. M. Gaudiosi, J. Holtsnider, R. I. Tobey, O. Cohen, M. M. Murnane, and H. C. Kapteyn, "Lensless Diffractive Imaging Using Tabletop Coherent High-Harmonic Soft-X-Ray Beams," Phys. Rev. Lett. **99,** 098103 (2007).

[45] J. J. Park, D. S. Kim, S. C. Jeon, J. Park, K. H. Lee, J.-H. Lee, K. N. Kim, J. J. Yoo, and C. H. Nam, "Soft x-ray microscope constructed with a PMMA phase-reversal zone plate," Optics Letters **34,** 235–237 (2009).

[46] B. R. Sandel *et al.*, "The Extreme Ultraviolet Imager Investigation for the IMAGE Mission," Space Sci. Rev. **91,** 197 (2000).

[47] G. L. T. Chiu and J. M. Shaw, http://www.research.ibm.com/journal/rd/411/chiu.html (accessed 21 January 2008).

[48] A. Hirai *et al.*, "Transmission X-Ray Microscopy with 50 nm Resolution Installed at Ritsumeikan Synchrotron Radiation Center," J. Appl. Phys. **38,** 274 (1999).

[49] B. Sae-Lao and R. Soufli, "Measurements of the refractive index of yttrium in the 50-1300-eV energy region," Appl. Opt. **41,** 7309 (2002).

[50] R. Soufli and E. Gullikson, "Absolute Photoabsorption Measurements of Molybdenum in the Range 60 to 930 eV for Optical Constant Determination," Appl. Opt. **37,** 1713 (1998).

[51] M. Fernandez-Perea, J. I. Larruquert, J. Aznarez, J. Mendez, M. Vidal-Dasilva, E. Gullikson, A. Aquila, R. Soufli, and J. L. G. Fierro, "Optical constants of electron-beam evaporated boron films in the 6.8-900 eV photon energy range," J. Opt. Soc. Am. **24,** 3800 (2007).

[52] B. Sandel, "IMAGE extreme ultraviolet imaged," http://euv.lpl.arizona.edu/euv/ (Accessed May 21, 2007).

[53] S. Lunt, "Determining the indices of refraction of reactively sputtered uranium dioxide thin films from 46 to 584 angstroms," Master's Thesis (Brigham Young University, Provo, UT, 2002).

[54] M. Urry, "Determining optical constants of uranium nitride thin films in the extreme ultraviolet (1.6-35 nm)," Senior Thesis (Brigham Young University, Provo, UT, 2003).

[55] N. Brimhall, A. Grigg, R. S. Turley, and D. Allred, "Thorium-based thin films in the extreme ultraviolet," Proc. of SPIE **6317,** 1–8 (2006).

[56] G. Acosta, "Scandium oxide thin films and their optical properties in the extreme ultraviolet," Ph.D. dissertation (Brigham Young University, Provo, UT, 2007).

[57] D. Allred, G. Acosta, N. Farnsworth-Brimhall, and R. S. Turley, "Simultaneous Reflection and Transmission Measurements from Coated Diodes to Determine

the Optical Constants of Thin Films in the Extreme Ultraviolet," 49th Annual Technical Conference Proceedings, Society of Vacuum Coaters **49,** 314–318 (2006).

[58] J. Johnson, "Computationally modeling the effects of surface roughness on soft x-ray multilayer reflectors," Master's Thesis (Brigham Young University, Provo, UT, 2006).

[59] J. Jackson, Senior Thesis (Brigham Young University, Provo, UT, 2007).

[60] B. L. Henke, E. M. Gullikson, and J. C. Davis, "X-ray interactions: photoabsorption, scattering, transmission, and reflection at E=50-30000 eV, Z=1-92," Atomic Data and Nuclear Data Tables **54,** 181–342 (1993).

[61] D. D. Allred, M. B. Squires, R. S. Turley, W. Cash, and A. Shipley, "Highly Reflective Uranium Mirrors for Astrophysics Applications," Proc. of SPIE 4782-29 (2002).

[62] N. Brimhall, J. Painter, N. Powers, G. Giraud, M. Turner, M. Ware, and J. Peatross, "Measured laser beam evolution during high-order harmonic generation in a semi-infinite gas cell," Optics Express **15,** 1684–1689 (2007).

[63] J. Painter, M. Adams, N. Brimhall, E. Christiansen, G. Giraud, N. Powers, M. Turner, M. Ware, and J. Peatross, "Direct observation of laser filamentation in high-order harmonic generation," Optics Letters **31,** 3471–3473 (2006).

[64] H. T. Kim, I. J. Kim, V. Tosa, Y. S. Lee, and C. H. Nam, "High brightness harmonic generation at 13 nm using self-guided and chirped femtosecond laser pulses," Appl. Phys. B **78,** 863–867 (2004).

[65] J. Sutherland, E. Christensen, N. Powers, S. Rhynard, J. Painter, and J. Peatross, "High harmonic generation in a semi-infinite gas cell," Optics Express **12,** 4430–4436 (2004).

[66] D. Strickland and G. Mourou, "Compression of amplified optical pulses," Opt. Comm. **56,** 219 (1985).

[67] P. Maine, D. Strickland, P. Bado, M. Pessot, and G. Mourou, "Generation of Ultrahigh Peak Power Pulses by Chirped Pulse Amplification," IEEEE Journal of Quantum Electronics **24,** 398–403 (1988).

[68] S. L. Voronov, "Controlling laser high-order harmonic generation using weak counter-propagating light," Ph.D. dissertation (Brigham Young University, Provo, UT, 2003).

[69] S. Kazamias, F. Weihe, D. Douillet, C. Valentin, T. Planchon, S. Sebban, G. Grillon, F. Auge, D. Huilin, and P. Balcou, "High order harmonic generation optimization with an apertured laser beam," Eur. Phys. J. D **21,** 353–359 (2002).

[70] E. T. J. Nibbering, G. Grillon, M. A. Franco, B. S. Prade, and A. Mysyrowicz, "Determination of the inertial contribution to the nonlinear refractive index of air, N2, and O2 by use of unfocused high-intensity femtosecond laser pulses," J. Opt. Soc. Am. B **14,** 650–660 (1997).

[71] S. Carusotto, E. Iacopini, E. Polacco, F. Scuri, G. Stefanini, and E. Zavattini, "Measurement of the Kerr constant of He, A, O2, N2, H2, and D2," Nuovo Cimento **5D,** 328–338 (1985).

[72] S. Champeaux and L. Berge, "Femtosecond pulse compression in pressure-gas cells filled with argon," Phys. Rev. E **68,** 066603 (2003).

[73] A. Chiron, B. Lamouroux, R. Lange, J. F. Ripoche, M. Franco, B. Prade, G. Bonnaud, G. Riazuelo, and A. Mysyrowicz, "Numerical simulations of the nonlinear propagation of femtosecond optical pulses in gases," Eur. Phys. J. D **6,** 383396 (1999).

[74] S. Carusotto, E. Iacopini, E. Polacco, F. Scuri, G. Stefanini, and E. Zavattini, "Measurement of the Kerr constant of He, A, O2, H2, and D2," Nuovo Cimento **5D,** 328338 (1985).

[75] M. Ammosov, N. Delone, and V. Krainov, "Tunnel ionization of complex atoms and of atomic ions in an alternating electromagnetic field," Sov. Phys. JETP **64,** 11911194 (1986).

[76] M. Lewenstein, P. Salieres, and A. L'Huillier, "Phase of the atomic polarization in high-order harmonic generation," Phys. Rev. A **52,** 4747–4754 (1995).

[77] K. Kulander and B. Shore, "Calculations of multi-harmonic conversion of 1064-nm radiation in Xe," Phys. Rev. Lett. **62,** 524 (1989).

[78] N. Brimhall, "Extreme ultraviolet polarimetry with laser-generated high-order harmonics," Master's Thesis (Brigham Young University, Provo, UT, 2007).

[79] A. Thompson *et al.*, *X-Ray Data Booklet* (Lawrence Berkeley National Laboratory, University of California, Berkeley, CA, 2001).

[80] H. Noda, T. Namioka, and M. Seya, "Geometric theory of holographic gratings," J. Opt. Soc. Am. **64,** 1031 (1974).

[81] T. Sekikawa, T. Kumazaki, Y. Kobayashi, Y. Nabekawa, and S. Watanabe, "Femtosecond extreme-ultraviolet quasi-continuum generation by an intense femtosecond Ti:sapphire laser," J. Opt. Soc. Am. B **15,** 1406 (1998).

[82] M. Turner, N. Brimhall, M. Ware, and J. Peatross, "Simulated laser-pulse evolution for high-order harmonic generation in a semi-infinite gas cell," Opt. Express **16,** 1571 (2008).

[83] D. G. Avery, "An improved method for measurements of optical constants by reflection," Proc. Phys. Soc. London Sect. B **65,** 425 (1952).

[84] R. F. Miller and A. J. Taylor, "Optical constants of thin films by an optimized reflection ratio method," J. Phys. D **4,** 1419 (1971).

[85] R. F. Miller, L. S. Julien, and A. J. Taylor, "Optical constants of gadolinium and terbium films obtained from in situ reflection measurements m ultra high vacuum," J. Phys. F **4,** 2338 (1974).

[86] H. R. Philipp and E. A. Taft, "Optical constants of germanium in the region 1 to 10 eV," Phys. Rev. **113,** 1002 (1959).

[87] H. J. Hagemann, W. Gudat, and C. Kunz, "Optical constants from the far infrared to the x-ray region: Mg, Al, Cu, Ag, Au, Bi, C, and Al_20_3," Journal of the Optical Society of America **65,** 742–744 (1975).

[88] R. Haensel, C. Kunz, T. Sasaki, and B. Sonntag, "Absorption Measurements of Copper, Silver, Tin, Gold, and Bismuth in the Far Ultraviolet," Applied Optics **7,** 301–306 (1968).

[89] D. H. Tomboulian, D. E. Bedo, and W. M. Neupert, "$M_{2,3}$ absorption spectra of the elemental solids Cr through Ge," J. Phys. Chem. Solids **3,** 282–302 (1957).

[90] D. Beaglehole, M. D. Crescenzi, M. L. Theye, and G. Vuye, "Dielectric constant of gold, copper, and gold-copper alloys between 18 and 35 eV," Phys. Rev. B **19,** 6303–6314 (1979).

[91] "X-ray Interactions with Matter," http://henke.lbl.gov/optical_constants/ (accessed 16 June 2009).

[92] A. Faldt and P. O. Nilsson, "Optical properties of uranium in the range 0.6-25 eV," J. Phys. F: Metal Phys. **10,** 2573–2580 (1980).

[93] M. Cukier, P. Dhez, F. Wuilleumier, and P. Jaegle, "Photoionization cross section of uranium in the soft x-ray region," Phys. Lett. A **48,** 307–308 (1974).

[94] M. B. Squires, Honors Thesis (Brigham Young University, Provo, UT, 1999).

[95] G. W. McGillivray, D. A. Geeson, and R. Greenwood, "Studies of the Kinetics and Mechanism of the Oxidation of Uranium by Dry and Moist Air, A Model for Determining the Oxidation Rate Over a Wide Range of Temperatures and Water Vapor Pressures," Journal of Nuclear Materials **208,** 81–97 (1994).

[96] A. G. Ritchie, R. C. Greenwood, and S. J. Randles, "The kinetics of the uraniumoxygenwater vapour reaction between 40 and 100 C," Journal of Nuclear Materials **139,** 121 (1986).

[97] J. Johnson, D. Allred, R. S. Turley, W. Evans, and R. Sandberg, "Thorium-Based Thin Films as Highly Reflective Mirrors in the EUV," Mater. Res. Soc. Symp. Proc. **893,** 207–214 (2006).

Index